DESIGN AND THEORETICAL STUDY OF WURTZITE GAN HEMTS AND APDS VIA ELECTROTHERMAL MONTE CARLO SIMULATION

A Thesis
Presented to
The Academic Faculty

by

Sriraaman Sridharan

In Partial Fulfillment
of the Requirements for the Degree
Doctor of Philosophy in the
School of Electrical and Computer Engineering

Georgia Institute of Technology
May 2013

DESIGN AND THEORETICAL STUDY OF WURTZITE GAN HEMTS AND APDS VIA ELECTROTHERMAL MONTE CARLO SIMULATION

Approved by:

Dr. P. Douglas Yoder, Advisor
School of Electrical and Computer Engineering
Georgia Institute of Technology

Dr. Russell Dean Dupuis
School of Electrical and Computer Engineering
Georgia Institute of Technology

Dr. Shyh-Chiang Shen
School of Electrical and Computer Engineering
Georgia Institute of Technology

Dr. Samuel Graham
School of Mechanical Engineering
Georgia Institute of Technology

Dr. Michael J. Leamy
School of Mechanical Engineering
Georgia Institute of Technology

Date Approved: 6 December 2012

To my family.

ACKNOWLEDGEMENTS

The first thank you goes to my thesis advisor Dr. Douglas Yoder for giving me the opportunity to work in this exciting field. I am very grateful for his unwavering support, encouragement, guidance, wisdom, and patience to help me complete this research. His rigor and high standards have truly made me a better engineer.

I would like to thank my committee members Dr. Russell Dean Dupuis, Dr. Shyh-Chiang Shen, Dr. Samuel Graham, and Dr. Michael J. Leamy for the opportunity to collaborate and for taking the time to review my thesis and provide valuable comments and suggestions.

I am grateful to Dr. Benjamin Klein for his support and for all the technical and non-technical discussions we have had over the years. I am indebted to him and his wife, Mrs. Julie Klein for hosting a memorable baby shower for my wife and making us feel at home. A special thanks to Mrs. Patricia Potter for organizing the baby shower and for all the administrate help I needed during my study.

I would also like to thank my former manager Dr. Stephan Mueller for seeing the potential in me and introducing me to Dr. Yoder. His encouragement and support helped me transition from industry to academia.

I am fortunate to have made good friends with Vivek Krishnamurthy, Aditya Kulkarni, Fahad Mohammed, Anusha Venkatachalam, Narayanan Terizhandur, Lane Thames, among others, and thank them for all the fun we had together. A special thanks to my good friends Michael and Lisa Jordan for always being there for me and my family.

I would like to express my deep gratitude to my parents, my sister, and my late grandmother for their constant love and support. I am forever grateful to my wife, Divya, for supporting me through all these years and helping me in any way possible to complete this work. Finally, the one person who kept me motivated all the way to the end is my daughter, Medha, with whom I can spend more time now.

TABLE OF CONTENTS

LIST OF FIGURES

SUMMARY

A self-consistent, full-band, electrothermal ensemble Monte Carlo device simulation tool has been developed. It is used to study charge transport in bulk GaN, and to design, analyze, and improve the performance of AlGaN/GaN high electron mobility transistors (HEMTs) and avalanche photodiodes (APDs).

Studies of electron transport in bulk GaN show that both peak electron velocity and saturated electron velocity are higher for transport in the basal plane than along the *c*-axis. Study of the transient electron velocity also shows a clear transit-time advantage for electron devices exploiting charge transport perpendicular to the *c*-axis. The Monte Carlo simulator also enables unique studies of transport under the influence of high free carrier densities but with low doping density, which is the mode of transport in AlGaN/GaN HEMTs.

Studies of isothermal charge transport in AlGaN/GaN HEMTs operating at high gate bias show a drain current droop with increasing drain-source bias. The cause of the droop is investigated and a design utilizing source- or gate-connected field plate is demonstrated to eliminate the drain current droop. Electrothermal aspects of charge transport in AlGaN/GaN HEMTs are also investigated, and the influence of non-equilibrium acoustic and optical phonons is quantified. The calculated spatial distribution of non-equilibrium phonon population reveals a hot spot in the channel that is localized at low drain-source bias, but expands towards the drain at higher bias, significantly degrading channel mobility.

Next, Geiger mode operation of wurtzite GaN-based homojunction APDs is investigated. The influence of dopant profile, active region thickness, and optical absorption profile on single photon detection efficiency (SPDE) are quantified. Simulations of linear mode gain as a function of multiplication region thickness and doping profile reveal that weakly n-type active regions may be exploited to achieve higher avalanche gain, without

penalty to either applied bias or active region thickness. A separate absorption and multiplication APD (SAM-APD) utilizing a AlGaN/GaN heterojunction is also investigated. The presence of strong piezo-electric and spontaneous polarization charges at the heterojunction enables favorable electric field profile in the device to reduce dark current, improve excess noise factor, improve quantum efficiency, and improve breakdown probability. To maximize SPDE, a new device structure with a buried absorber is proposed and improved SPDE is demonstrated.

Lastly, a new approach for the direct generation of self-sustaining millimeter-wave oscillations is proposed. In contrast to Gunn diodes, which exploit a bulk-like active region, periodic oscillation is achieved in the proposed structures through the creation, propagation and collection of traveling dipole domains supported by fixed polarization charge and the associated two-dimensional electron gas along the plane of a polar heterojunction. Numerical simulation of induced oscillations in a simple triode structure commonly used for AlGaN/GaN HEMTs reveals two distinct modes of self-sustaining millimeter-wave oscillation.

CHAPTER I

INTRODUCTION

Gallium nitride (GaN) and related alloys are an attractive material system for a wide variety of applications due to their favorable electrical, thermal, and optical properties. Their high breakdown field strength, high saturated electron drift velocity, direct wide band gap, good thermal conductivity, and the ease of forming heterojunctions make them attractive for high-power, high-frequency electrical and optical devices. GaN high electron mobility transistors (HEMTs) have enabled significant advances in RF and micro- and millimeter-wave power amplification [1]. Solar-blind applications benefit from GaN-based unity-gain photodiodes [2], and recent improvements in both material quality and fabrication techniques have enabled high-gain ultraviolet (UV) avalanche photodiodes (APDs) [3]. UV single-photon detectors using Geiger mode GaN APDs also have been demonstrated [4, 5]. Lasers and light-emitting diodes operating between green and deep UV have already been demonstrated [6, 7]. Promising opportunities exist for further penetration into the visible spectrum using indium-rich material, as well as into the infrared by exploiting heterojunctions and inter-subband transitions [8].

In this research, charge transport in AlGaN/GaN HEMTs and APDs has been theoretically investigated by developing a comprehensive, self-consistent, full-band Monte Carlo device simulator. The simulator has been used to design, analyze, and improve the performance of AlGaN/GaN HEMTs and APDs.

1.1 Organization of the thesis

The following sections of this chapter provide a brief overview of the III-nitride material system and the motivation and objectives of this research. The next chapter introduces the Boltzmann transport equation (BTE) and describes the Monte Carlo method used to solve it. Chapter III details the simulation and calibration of charge transport in bulk GaN. The

results of isothermal and electrothermal simulation of AlGaN/GaN HEMTs are presented in chapters IV and V, respectively. Chapter VI introduces the homojunction APD followed by the details of its model, calibration, and design features. Chapter VII explores the design of heterojunction APD and presents a new design that improves the single photon detection efficiency. Chapter VIII describes the traveling dipole domains predicted by our simulations to occur in AlGaN/GaN triode structures and highlights its application to the direct generation of millimeter-wave oscillations. Finally, chapter IX concludes the thesis by presenting a summary and a discussion of the possible future directions of this work.

1.2 Overview of the III-nitride material system

Group III-nitride materials GaN, AlN, InN, and their alloys are an attractive material system for novel electronic and optoelectronic device applications. They crystallize in wurtzite, zincblende, and rocksalt crystal structures, with wurtzite being the equilibrium structure at room temperature. Due to the lack of an ideal lattice matched substrate, III-nitrides are commonly grown on sapphire, SiC, or Si substrates. The nature of these substrates and the equilibrium crystal structure of these materials favor the growth of high-quality material in the wurtzite crystal form. This research focuses on the study of devices fabricated using wurtzite GaN and its ternary alloy AlGaN.

Wurtzite is the hexagonal analog of the zincblende lattice. The crystal structure is an arrangement of interpenetrating layers of Ga and N atoms in which each atom is tetragonally connected with four atoms of the opposite species. The unit cell has a basis of four atoms with lattice constants a = 3.189 Å in the basal plane and c = 5.185 Ånormal to the basal plane [9, 10]. The bandgap energy is 3.4 eV at 300K [9, 11]. Compared to GaAs [12], GaN has a larger peak electron velocity [13], larger electron saturation velocity [14], higher breakdown field strength due the wide bandgap energy [15–17], and good thermal conductivity [18, 19] as shown in Table 1.

Electrical Property	GaAs	GaN
Bandgap (eV)	1.43	3.4
Breakdown field (MV/cm)	0.4	3
Electron mobility (cm^2/V.s)	6500	900
Saturated steady-state electron velocity (10^7 cm/s)	1.2	1.9
Peak steady-state electron velocity (10^7 cm/s)	2	3
Peak transient electron velocity (10^7 cm/s)	6	7.25
Thermal conductivity (W/K.cm)	0.5	1.7
Dielectric constant	12.8	9

Further enhancing the advantages of GaN for HEMT and APD applications is the presence of spontaneous and piezoelectric polarization charges. Polarization induces an internal electric field in the material and leads to an equal and opposite sheet charge accumulation at the end faces of the crystal. The polar nature of the ionic bonds in GaN gives rise to spontaneous polarization, with the wurtzite structure having the highest symmetry compatible with the existence of spontaneous polarization [20]. Piezoelectric polarization in epitaxial layers is due to the strain introduced by the inherent lattice mismatch between the layers. Fortuitously, for HEMT applications where a tensile strained AlGaN is grown on GaN buffer layers, the piezoelectric and spontaneous polarizations point in the same direction and the total polarization is the sum of the individual components. At the abrupt AlGaN/GaN interface the net polarization charge density is the sum of the piezoelectric and spontaneous polarization components of the two materials and is positive in the case of AlGaN grown on top of GaN with Ga-face polarity. To compensate this polarization induced charge density, free electrons accumulate in the triangular quantum well at the AlGaN/GaN interface and form a two dimensional electron gas (2DEG) with sheet charge densities on the order of $1 \times 10^{13}/cm^2$, which is significantly higher than in GaAs ($5 \times 10^11/cm^2$) [21, 22]. The large sheet charge density enables AlGaN/GaN HEMTs to achieve channel currents well in excess of 1A/mm [21].

High-power, high-frequency applications such as microwave power amplifiers fundamentally require large current and voltage capabilities along with small control terminal capacitance. The large current and voltage directly yield large power, while small control terminal capacitance allows fast switching required for high-frequency operation. Large current capability is achieved by high carrier mobility and high carrier densities. Modulation doped AlGaN/GaN HEMT structures in which a 2DEG is formed in the undoped channel, excel in both of these capabilities. Electron mobility is very high in the undoped channel due to the low density of ionized impurities, and the 2DEG has a high electron sheet charge density. A direct result of the wide bandgap of GaN is the high breakdown voltage, which allows large biases to be applied across the device for a given feature size, compared to narrower-bandgap material systems [23]. Due to the 2DEG, the HEMT channel is normally "on" and a relatively short gate is sufficient to pinch-off the channel to turn the device off. This results in a low gate capacitance. All these features combined with the good thermal conductivity of GaN and AlGaN [18, 19, 24] make this material system an excellent candidate for high-power, high-frequency device applications [23, 25, 26].

GaN is also well suited for solar-blind radiation detection in the deep UV frequencies ranging from 360nm to well below 250nm. GaN-based APDs offer the potential for high sensitivity, low noise, and low dark current density. The large breakdown field strength of 3MV/cm [15–17] allows the device to be operated at high fields resulting in avalanche photocurrent gains in excess of 10^4 [27]. The wide bandgap results in low dark current densities below 10^{-7} A/cm^2 [27] and the direct bandgap allows higher quantum efficiency. Heterojunctions with AlGaN provide design opportunities for tailoring the field profile to maximize gain and quantum efficiency, while bandgap engineering with heterojunctions enables tuning the absorption spectrum. Geiger mode operation for single photon detection is possible by briefly biasing the APDs above the steady-state breakdown voltage.

1.3 Motivation and objectives

The complex nature of charge transport in the high-field and high-power regimes in which GaN devices are typically operated demands full bandstructure calculations and accurate models for the microscopic processes that influence electrical and thermal transport. Gaining insight into device operation through simulation is crucial for the optimal design of these high performance devices. For instance, in high-power, high-frequency HEMTs, the power-added efficiency is thought to be limited by parasitic thermal effects [28, 29], and these devices have to be designed accordingly. Key design aspects that influence the performance of HEMTs are gate-drain spacing, gate length, barrier thickness, aluminum mole fraction in the barrier, placement of electrical and thermal contacts, and other design features such as the addition of source- or gate-connected field plates. Likewise, the key design considerations for Geiger mode APDs for single-photon detection applications are the influences of dopant profile, active region thickness and spatial distribution of photon absorption on single-photon detection efficiency. Hence, an accurate charge transport model for the GaN material system and a reliable tool to simulate the model are critical for exploring the design aspects of HEMTs and APDs.

Charge transport in wurtzite GaN has been studied through the stochastic solution of the semiclassical Boltzmann transport equation (BTE) using the Monte Carlo method [30–35]. The Monte Carlo method allows direct simulation of carrier trajectory in devices and physical information can be tracked to obtain the solution of the BTE [36–43]. The complexity of the models included determines the accuracy of the solution and detailed models are required for important phenomena, particularly models appropriate for the high-field regime and for thermal aspects of transport. These include models for non-equilibrium phonon dynamics, including all significant optical and acoustic phonon modes, an accurate lattice heat transport model for performing electrothermal analysis, dynamic models for temperature and density dependent scattering rates, and an accurate model for impact ionization in GaN.

The objective of this research is twofold: (a) to develop a comprehensive, self-consistent,

full-band Monte Carlo device simulator incorporating charge transport models appropriate for the high-field, high-power regime, and (b) to leverage it for predictive studies into the operation of wurtzite GaN-based devices such as high electron mobility transistors (HEMTs) and avalanche photodiodes (APDs) at the microscopic level and demonstrate optimized designs based on the deeper understanding which theoretical modeling provides.

CHAPTER II

MODELING CHARGE TRANSPORT IN WURTZITE MATERIALS

Charge transport in semiconductors can be described in the semi-classical limit by the distribution function of the charge carriers. Under non-equilibrium conditions, the distribution function evolves under the action of an applied electric field. Knowledge of the non-equilibrium distribution function allows direct calculation of all semiclassical observables such as current, carrier energy. The Boltzmann transport equation (BTE) provides a general method for obtaining the non-equilibrium distribution function in the semi-classical approximation [37, 43–48]. In this chapter, a brief overview of the BTE is presented followed by a detailed description of the Monte Carlo method used to solve it.

2.1 The Boltzmann Transport Equation

The distribution function f_n is a function of the real space coordinates $\vec{r}$, momentum space coordinates $\vec{k}$, and time t. The function $f_n(\vec{r}, \vec{k}, t)$ is defined as the probability that an electronic state in band n at position $\vec{r}$ with wavevector $\vec{k}$ is occupied at time t. The rate of change of the distribution function for electrons in the seven-dimensional space (3 in $\vec{k}$, 3 in $\vec{r}$, and t) is given by the BTE as [49, 50]

$$\frac{\partial f_n}{\partial t} = \frac{q}{\hbar}\vec{E}(\vec{r}) \cdot \nabla_k f_n - \vec{v}(\vec{k}) \cdot \nabla_r f_n + \left.\frac{\partial f_n}{\partial t}\right|_{scattering}. \tag{2.1}$$

Approximate solutions to the BTE may be obtained by the *method of moments* [37, 50]. The n^{th} moment equation is obtained by multiplying both sides of the BTE by $c_n\vec{k}^n$ and integrating over $\vec{k}$-space. Solving the zeroth-order moment equation yields the well-known continuity equations for electrons and holes. Applying the effective mass and parabolic energy band approximation along with the relaxation time approximation to the first-order moment equation yields an expression for the electron and hole current densities with drift, diffusion, thermocurrent, and convection terms. In the low-frequency limit, the thermocurrent and convection terms are neglected. The drift and diffusion terms,

combined with the continuity equations, is the standard system of drift-diffusion (DD) equations.

Numerical device solvers based on DD are relatively simple and computationally efficient [51–53]. However, the drastic approximations used in DD limit their range of validity and mask the features of the underlying transport phenomena [37, 40]. Methods employing higher-order moments of the BTE such as hydrodynamic or energy-transport models are an improvement over the DD model and account for carrier heating and non-local phenomena but fail to account for the bandstructure and scattering processes at high energies, limiting them to low-field applications. Moreover, the BTE requires knowledge of the electric fields inside the device, which in turn depend on the distribution of charge density via the Poisson equation and have to be determined self-consistently. Hence, to calculate the electronic current in a semiconductor device, the BTE needs to be solved in conjunction with the Poisson equation. The Monte Carlo method, is ideally suited to solve the BTE, including full bandstructure effects in the equations of motion and in the scattering integrals, and can be easily coupled with a Poisson equation solver to self-consistently determine the spatial distribution of electric field inside the device.

2.2 The Monte Carlo Method

The Monte Carlo technique first proposed by Kurosawa [44] is a statistical approach to the solution of the BTE. This method directly simulates charge carrier motion in a crystal under non-equilibrium conditions, where the particle trajectory is represented by a sequence of free flights and scattering events. The dynamics of the free flight account for the action of external forces and the free flights are interrupted by scattering events. The duration of the free flights are determined stochastically based on the scattering probabilities, which are calculated from the known probability distributions of microscopic processes. Electronic dispersion provides the energy–wave vector relationship of the charge carriers, which determines their dynamical properties under the influence of external forces. Observable quantities such as particle velocity and energy can be tracked and the final solution can be calculated by averaging over a large number of independent samples.

Using fast computers it is possible to simulate a large number of samples to obtain sufficiently accurate solution of the BTE for microscopic models of considerable complexity. The nature of the samples depend on the type of transport process under investigation. For steady-state, homogeneous phenomenon, it is sufficient to simulate the motion of one single particle over a long time, due to the principle of ergodicity. According to the ergodic theorem, tracking a sufficiently long trajectory of this sample particle would provide information about the steady-state behavior of the system. For non-homogeneous or transient processes, it is necessary to simulate a large number of particles and track their dynamic behavior to obtain information on the process. Simulating a large number of particles is also required for simulations involving the self-consistent solution of the Poisson equation to calculate the electric field strength inside the device.

The earliest application of Monte Carlo techniques for modeling charge transport dates back to the study of the hot electron problem by Kurosawa in 1966 [44]. The Malvern, Worcestershire, group made significant early contributions to the application of the Monte Carlo method for charge transport [45–47]. The significant early contributions were the introduction of the self-scattering scheme [54], incorporation of non-parabolicity effects [46]. Lebwohl and Price [48] demonstrated many-particle simulation by implementing the earliest self-consistent particle-field Monte Carlo device simulator. Wang and Hess [39] calculated electron velocity distribution in AlGaAs/GaAs HEMTs by including scattering due to phonons, impurities, defects, and electron-electron interactions. U. Ravaioli and D. K. Ferry [41] followed by simulating transport in GaAs HEMTs, accounting for quantization in the inversion layer. H. Shichijo and K. Hess [55] and J. Y. Tang and K. Hess [56] highlighted the strong role of the bandstructure and the importance of the correct density of states (DOS) on calculating electron-lattice scattering rates and impact ionization coefficients. Important contributions to matrix elements for electron-phonon coupling are reviewed in J. M. Ziman [57]. L. V. Keldysh [58] derived a simple formula for calculating the rate for impact ionization for electrons. E. O. Kane [59] introduced the random-$\vec{k}$ approximation for efficient computation of the impact ionization scattering rates.

Fischetti and Laux [42] developed DAMOCLES, a complete Monte Carlo device simulator that implements full bandstructure calculations, with consistently computed scattering rates and a self-consistent Poisson equation solver. Long-range and short-range interactions between carriers are also accounted for in their transport model. Details of the simulation tool and results obtained for n- and p-channel Si MOSFETs, GaAs MESFETs, and Si bipolar junction transistors are presented in [43].

For this present research, a state-of-the-art, comprehensive, self-consistent, full-band, electrothermal Monte Carlo simulator has been developed, the details of which are presented in the following sections.

2.3 Simulating charge transport

The overall design of the Monte Carlo (MC) device simulator is based on a full band ensemble device simulator developed by P. D. Yoder at Bell Labs for use with high-speed zincblende photodiodes. The present work adds new modules to simulate transport in two dimensional (2D) device structures using a wurtzite bandstructure stored as a three dimensional (3D) tetrahedral grid. The simulator consists of a grid module that reads 2D real space grids and 3D $\vec{k}$ - space grids, and holds them efficiently in an internal data structure. Carriers are treated as point-like semi-classical particles. Particle trajectories are tracked in both the real space and $\vec{k}$ - space based on equations of motion in a crystal [37] and stochastic scattering events.

Bandstructure, computed on a tetrahedral grid, provides the energy-wavevector relation. Efficient algorithms are used to propagate particles in both real and $\vec{k}$ - spaces as described in the following sections. The required physical information is collected over the entire simulation duration and the simulator implements several estimators to calculate both instantaneous and cumulative transport quantities. A 2D Poisson solver is coupled to self-consistently calculate the electric field profile on the 2D mesh, properly accounting for polarization charges and boundary conditions. Some critical design and implementation aspects of the simulator are presented here.

2.3.1 Finite Volume Grids

For device simulations, 2D unstructured meshes based on Delaunay tesselations and the OCTREE algorithm are used. These meshes may be generated by OMEGA [60, 61], CAMINO [62], MESH [63, 64] and other available public-domain or commercial packages. Such Delaunay grids are suitable for the finite volume integration of the Poisson equation, as they feature irregular yet exclusively acute angled triangular elements [65]. The grid spacing is refined to be smaller than the Debye length for the expected charge densities to ensure accurate solution of the Poisson equation. Details of the layers, material types, contacts, boundary elements, and layer interfaces are associated with the mesh nodes, edges and elements. The MC simulator also generates several additional information about the grid such as the list of neighboring elements for propagating particles, coefficients for particle-mesh coupling, and node volumes.

The 3D tetrahedral grid for bandstructure calculation is generated by *TetGen* [66]. The vertices of the tetrahedra are the coordinates of the wavevectors at which the energies are calculated. Similar to the 2D real space grid, the MC simulator generates additional information about the 3D grid such as wavevector-energy coupling coefficients, the energy gradient, and neighboring elements.

For both the 2D and 3D grids, the MC simulator implements efficient search algorithms to find the element containing a given point.

2.3.2 Propagating particles

The motion of particles is modeled as a series of free flights, interrupted by scattering events. Particles are propagated in the real space by updating their coordinates according to their group velocity, which is calculated based on their position in the $\vec{k}$ - space [50].

$$\vec{r}(t) = \vec{r}(0) + \int_0^t \vec{v}(t')\, dt' \tag{2.2}$$

The rate of change of the k-space coordinates is calculated using the electric field strength at the particle's position in real space [50]:

$$\frac{d\vec{k}}{dt} = \pm\frac{q}{\hbar}\,\vec{E}(\vec{r}) \tag{2.3}$$

where the leading + is for holes and − for electrons.

In real space, the particles are typically propagated between edges of the triangular elements and the current element is tracked using the precomputed neighbor information. Internal interfaces between different regions of the device, external edges, and contacts are detected and the following actions are taken. In the case of internal interfaces between different materials, particles with sufficient energy to overcome any energy barrier are transmitted into the new region or reflected otherwise. External edges reflect the particles back into the device and particles reaching the contacts are collected and removed from simulation.

Tracking particles in the $\vec{k}$-space is more complex, primarily due to the tetrahedral elements, which are connected at their faces. Due to symmetry considerations only the irreducible wedge (IRW) of the first Brillouin zone needs to be represented by the $\vec{k}$-space grid. Propagating particles in $\vec{k}$-space also involves performing symmetry operations to reflect them at the IRW boundaries to keep them in the IRW while maintaining rotation information so that group velocity may be calculated correctly. When a scattering event occurs, a new $\vec{k}$-space coordinate and band index are calculated according to the correct probability of the scattering mechanism. The present implementation is very efficient, and uses optimized data structures to track position, energy, and momentum. The scattering rate calculation and its implementation are described in the sections that follow.

A rotation matrix and its inverse are used to simulate transport in arbitrary crystal orientations. For instance, the rotation matrix can be set up such that the 2D real space represents transport in the $(11\bar{2}0)$ crystal plane. Such a rotation matrix and its inverse would be

$$R = \begin{pmatrix} \sqrt{3}/2 & 0 & -1/2 \\ 1/2 & 0 & \sqrt{3}/2) \\ 0 & -1 & 0 \end{pmatrix} \qquad R^{-1} = \begin{pmatrix} \sqrt{3}/2 & 1/2 & 0 \\ 0 & 0 & -1 \\ -1/2 & \sqrt{3}/2 & 0 \end{pmatrix}, \tag{2.4}$$

where R and R^{-1} map the real space $+x$ & $-y$ axis to the $\Gamma \rightarrow K$ & $\Gamma \rightarrow A$ directions, respectively in the $\vec{k}$ space, and vice versa.

2.4 *Wurtzite GaN Bandstructure*

Electronic dispersion provides the energy-wavevector relation, $E_n(\vec{k})$, for electronic particles moving in the periodic crystal lattice, where n is the band index. The energy E is a multiple valued function of the wavevector $\vec{k}$ and requires the band index to be specified to determine E for a given value of $\vec{k}$. For simulating charge transport, the bandstructure is constructed by calculating the energy of several bands at every point on a 3D finite element grid. The grid fully encompasses the irreducible wedge of the first Brillouin zone.

Due to its importance in the study and design of GaN-based devices, theoretical calculation of the GaN bandstructure has been extensively studied. First-principles bandstructure calculation of GaN has been performed by several investigators. The earliest comprehensive effort to compute the full bandstructure for wurtzite GaN was performed by Bloom *et al.* [67] using an empirical pseudopotential method (EPM) with the form factors adjusted to produce a bandstructure which agrees with the energies of a limited number of experimental reflectivity peaks.

Rubio *et al.* [68] have used the *ab initio* pseudopotential method (APM) within the local-density approximation (LDA) to investigate the electronic properties of wurtzite GaN. They employed the quasiparticle correction using the Green's function with screened Coulomb interaction approach to correct the band gap underestimation caused by the LDA.

Suzuki *et al.* [69] have computed the electronic bandstructure of wurtzite GaN using a self-consistent full-potential linearized-augmented plane-wave (FP-LAPW) method within the density functional approximation. They focus on electronic structures around the conduction band minimum and valence band maximum, and link the first-principles calculation of the electronic bandstructure with the effective-mass theory. They have also derived effective mass parameters, which can be used for the design of optical devices.

Kolnik *et al.* [31] have performed electronic bandstructure calculation of wurtzite GaN-based on the EPM. They used 19 non-zero form factors to describe the pseudopotential and approximately 110 plane waves in the basis set for the wurtzite material. The form factors were determined by comparing the bandstructure results with the results of first-principles

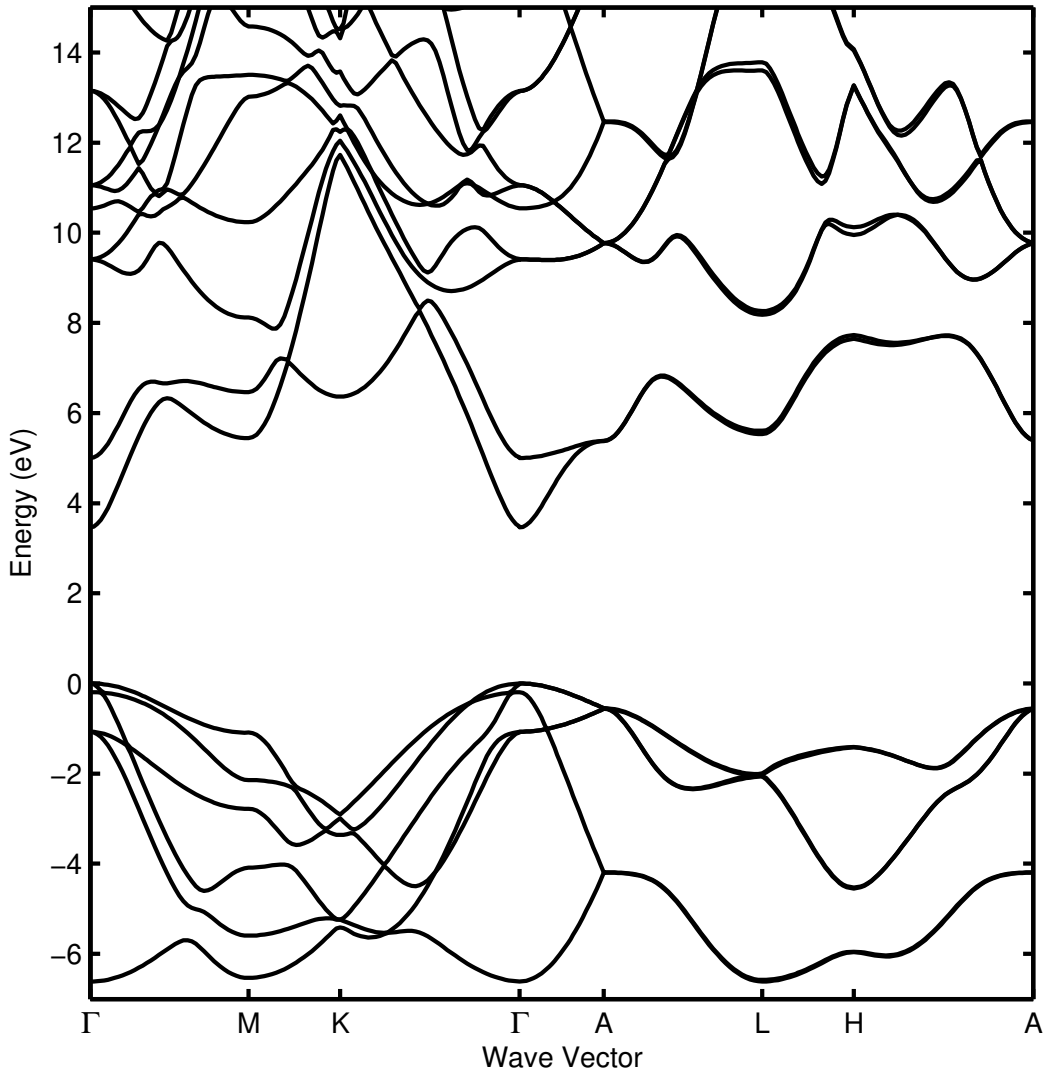

Figure 2.1: Bandstructure of wurtzite GaN

calculation and with experimental data for band gaps and effective masses.

Yeo *et al.* [70] have applied EPM, and adjusted the form factors of GaN to reproduce band features matching newer experimental data and valence bands of accurate first-principles calculations.

Goano, *et al.* [71] have presented nonlocal empirical pseudopotential calculations of the wurtzite GaN bandstructure based on *analytical* expressions for empirical atomic pseudopotentials for Ga, Al and N. Their calculated bandstructure is in good overall agreement with experimental/*ab initio* values. To date, no record exists in the scholarly literature documenting the successful reproduction of Goano's calculations.

For the present research, the bandstructure of wurtzite GaN has been calculated using the method of empirical pseudopotentials (EPM), with form factors calibrated to reproduce known effective masses and optical transition energies. The bandstructure is precomputed on a tetrahedral grid representing the IRW. Energies for wavevectors outside the IRW are computed by transforming them to the IRW using symmetry operators. The Brillouin zone is also divided into valleys Γ, A, M, L, H, and K corresponding to the symmetry points. Energies for up to ten conduction bands and eight valence bands are available, as shown in Figure 2.1. The implementation reads in the bandstructure data and precomputes the gradient of energy with respect to the wavevector, along with coupling coefficients for interpolation of energy. The range of energies are split in 10meV bins, and the density of states at the center of the bins are precalculated. The possibility of a band crossing exists in regions where adjacent band energies approach each other. Band crossings are detected using the particle's history and projected path, properly accounting for scattering events that may disrupt their trajectory in $\vec{k}$-space.

2.5 Scattering rates and final state selection

Scattering rates are calculated using Fermi's golden rule in the first Born approximation in a manner fully consistent with the bandstructure. Fermi's golden rule [50], which is derived from time-dependent perturbation theory, gives the transition probability per unit time (transition rate) of a particle from a state $|n, \vec{k}\rangle$ to a different state $|n', \vec{k}'\rangle$, due to interaction with a time-harmonic potential. The transition rate, long after the interaction with the potential ($> 10^{-14}$ s), is given by [50]

$$S(n, \vec{k}; n', \vec{k}') = \frac{2\pi}{\hbar} \left| \int_V \psi^*_{n',\vec{k}'} \, V(\vec{r}) \, \psi_{n,\vec{k}} \, d^3r \right|^2 \left[\delta(E_n(\vec{k}) - E_{n'}(\vec{k}') - \hbar\omega_{\vec{q}}) + \delta(E_n(\vec{k}) - E_{n'}(\vec{k}') + \hbar\omega_{\vec{q}}) \right], \tag{2.5}$$

where $\vec{q} = \vec{k}' - \vec{k}$.

The delta function in the above expression enforces energy conservation. The first term is the matrix element of the interaction, and performing the integration over the volume of the crystal enforces the conservation of crystal momentum. The three dimensional integral

of the matrix element may be denoted compactly using Dirac's notation as

$$\langle n', \vec{k}' | H_1 | n, \vec{k} \rangle = \int_V \psi^*_{n', \vec{k}'} \, V(\vec{r}) \, \psi_{n, \vec{k}} \, d^3 r. \tag{2.6}$$

The matrix element is time-independent and the total scattering rate is computed by integrating $S(n, \vec{k}; n', \vec{k}')$ over all possible final states $(n', \vec{k}')$ in the Brillouin zone. The possible set of final states is relatively small when the energy conservation is enforced beforehand.

The MC simulator includes a generalized set of algorithms to compute scattering rates and generate final states for different scattering mechanisms. Depending on details of the mechanisms, different matrix elements and perturbation frequencies are used for the various interactions. Intravalley, intervalley, and interband transitions are supported. Brillouin zone integration of the differential scattering rates is performed by summing over the incremental contribution of all possible final states. Both $\vec{k}$-dependent and $\vec{k}$-independent matrix elements are independently supported along with the option of precomputing computationally intensive rates that can be stored in and retrieved from a file system. Final state energy is determined by the final wavevector $\vec{k}'$ and the final band index n'. For scattering mechanisms involving phonon interaction such as deformation potential scattering, multiple phonon modes and the corresponding selection rules are also supported. The scattering rates are computed and stored as a function of energy in 10meV intervals. Rates for intermediate energies are calculated by linear interpolation.

The final state selection after scattering is implemented as a multi-step process. Isoenergy surfaces at the final state energy are considered, and a rejection technique [37] is used to randomly choose a final state element according to its differential scattering rate contribution. Next, a final state within the isoenergy surface intersecting this element is generated by randomly scaling the basis vectors defining the state.

The scattering mechanisms currently implemented are ionized impurity, dislocation, polar optical phonon, deformation potential, and impact ionization.

2.5.1 Ionized impurity scattering

The calculation of the scattering rate due to ionized impurities is presented here. Mobile electrons in a crystal are scattered by the perturbation in the periodic potential introduced

by an ionized impurity. The interaction is Coulombic and the matrix element for the interaction is obtained using the Brooks-Herring approach [50, 72], which accounts for the screening of the impurity potential by means of the Thomas-Fermi screening model [72]. The approach is valid only when there are sufficient mobile electrons to screen the impurity potential. The perturbing potential of a single impurity at the origin is then

$$V(\vec{r}) = \frac{e^2}{4\pi\epsilon_0\epsilon_r} e^{-q_s\vec{r}}, \tag{2.7}$$

where q_s is the reciprocal of the screening length. The screening length in this case is the Debye length, L_D, given by

$$L_D^2 = \frac{\epsilon_0\epsilon_r k_B T}{e^2 n}, \tag{2.8}$$

where k_B is the Boltzmann constant and n is the free electron density. The matrix element is

$$\begin{aligned}\langle\vec{k}'|V(\vec{r})|\vec{k}\rangle &= \int_V e^{-i\vec{k}'\cdot\vec{r}}\, V(\vec{r})\, e^{i\vec{k}\cdot\vec{r}} d\vec{r} \\ &= \frac{e^2}{V\,\epsilon_0\epsilon_r}\,\frac{1}{q^2+q_0^2}\,,\end{aligned} \tag{2.9}$$

where $q = |\vec{k} - \vec{k}'|$. The scattering rate is

$$S_n(\vec{k},\vec{k}') = \frac{2\pi}{\hbar}\,\frac{e^4}{V^2\,\epsilon_0^2\epsilon_r^2\,(q^2+q_0^2)^2}\,\delta(E_n(\vec{k}) - E_n(\vec{k}')). \tag{2.10}$$

The total scattering rate can be found by summing over all final states

$$S_n(\vec{k}) = \sum_{\vec{k}'} S_n(\vec{k},\vec{k}'). \tag{2.11}$$

The summation over the final states can be performed numerically but that requires searching the entire Brillouin zone for suitable final states. This process can be simplified by transforming the summation over $\vec{k}'$ into an integral over energy E and leveraging the property of the δ function

$$\int_{-\infty}^{\infty} f(E')\delta(E-E')dE' = f(E). \tag{2.12}$$

The transformation is accomplished by first transforming the summation over $\vec{k}'$ into an integral over $\vec{k}'$ using [50]

$$\frac{1}{V}\sum_{\vec{k}'} \to \int \left(\frac{1}{2\pi}\right)^3 d\vec{k}'. \tag{2.13}$$

For an arbitrary $E(\vec{k})$ relation,

$$\frac{1}{(2\pi)^3}\int d\vec{k} = \iint \frac{dS}{\left|\nabla_{\vec{k}} E(\vec{k})\right|\Big|_{E'}}, \tag{2.14}$$

where the integral dS is performed over the isoenergy surface E' in the Brillouin zone.

Combining the above steps and noting that the interaction is elastic ($E_n(\vec{k}) = E_n(\vec{k}')$), Equation (2.11) becomes

$$S_n(\vec{k}) = \frac{2\pi}{\hbar}\,\frac{e^4}{V\,\epsilon_0^2\epsilon_r^2} \iint\limits_{E_n(\vec{k})=E_n(\vec{k}')} \frac{dS'}{(q^2+q_0^2)^2\,|\nabla_{\vec{k}} E_n(\vec{k})|}. \tag{2.15}$$

The integral over the isoenergy surface is replaced by a summation over the discrete shapes that make up the isoenergy surface in each element of the $\vec{k}$-space grid. For each of those shapes, it is assumed that the grid is sufficiently refined so that the term $q = |\vec{k}' - \vec{k}|$ is a constant. The summation has been implemented efficiently by precomputing several terms such as $|\nabla_{\vec{k}} E_n(\vec{k})|$ and the matrix coefficients required for computing dS. To further speed up the simulation, the rates themselves are precomputed as a function of energy and band index in all valleys. $\vec{k}$-dependent rate calculation is still required for final state selection by the rejection method.

2.5.2 Dislocation scattering

The scattering rate due to line defects is considered here. Only the matrix element is derived here as the rest of the rate calculation and implementation follows the ionized impurity scattering described in the previous section. A line defect is modeled as an uniform line charge with linear charge density Q_l. The macroscopic line defect is essentially infinitely long when compared to the lattice spacing. The matrix element is derived for the case of a line defect along the z-axis at the origin. The final result may be transformed easily for line defects in other orientations. The screened potential due to a differential element dz of the infinite line charge, in cylindrical coordinates, is [73]

$$dV(r,z) = \frac{Q_l}{4\pi\epsilon_0\epsilon_r\sqrt{r^2+z^2}}\, e^{-q_s\sqrt{r^2+z^2}}\, dz, \tag{2.16}$$

where r is the perpendicular distance from the line defect and q_s is the reciprocal of the screening length as defined in the previous section. Integrating over all z yields

$$V(r) = \frac{Q_l}{4\pi\epsilon_0\epsilon_r} \int_{-\infty}^{\infty} \frac{e^{-q_s\sqrt{r^2+z^2}}}{\sqrt{r^2+z^2}}\, dz \tag{2.17}$$

Making the change of variable $z = r\tan\phi$, the integral may be rewritten as

$$V(r) = \frac{Q_l}{2\pi\epsilon_0\epsilon_r} \int_{0}^{\pi/2} e^{-q_s \sec\phi} \sec\phi\, d\phi \tag{2.18}$$

The matrix element is given by

$$\langle\vec{k}'|V(r)|\vec{k}\rangle = \int_V V(r) e^{-i\,(\vec{k}-\vec{k}')\cdot\vec{r}}\, d\vec{r}. \tag{2.19}$$

Using cylindrical coordinates and defining

$$\vec{r} \equiv (r\cos\theta, r\sin\theta, z)$$

$$\vec{q} = \vec{k} - \vec{k}'$$

$$\vec{q}\cdot\vec{r} = rq_r\cos(\theta - q_\theta) + zq_z,$$

the matrix element can be rewritten as

$$M_{\vec{q}} \equiv \langle\vec{k}'|V(r)|\vec{k}\rangle = \frac{Q_l}{2\pi\epsilon_0\epsilon_r} \int_{-\infty}^{\infty}\int_{-\infty}^{\infty}\int_{0}^{2\pi}\int_{0}^{\pi/2} e^{-q_s\sec\phi} \sec\phi\, d\phi\, e^{-i\,(rq_r\cos(\theta-q_\theta)+zq_z)}\, r\, d\theta\, dr\, dz, \tag{2.20}$$

Integrating e^{-izq_z} over dz yields the delta function $2\pi\delta(q_z)$. Using the integral

$$\int_0^\infty r\, e^{-ar}\, e^{-ibr}\, dr = \frac{a^2 - b^2 - i\,2ab}{(a^2+b^2)^2} \tag{2.21}$$

and performing the integration over dr and $d\theta$ reduces the matrix element to

$$\begin{aligned} M_{\vec{q}} &= \frac{2\pi Q_l\,\delta(q_z)}{\epsilon_0\epsilon_r} \int_0^{\pi/2} \frac{q_s\sec^2\phi}{(q_s^2\sec^2\phi + q_r^2)^{3/2}}\, d\phi \\ &= \frac{2\pi Q_l\,\delta(q_z)}{\epsilon_0\epsilon_r}\, \frac{1}{q_s^2+q_r^2} \end{aligned} \tag{2.22}$$

2.5.3 Deformation potential scattering

The short-range interaction of electrons and lattice vibrations is described in terms of deformation potentials [50, 72]. The state vector of the system consists of the electron and phonon configurations represented as $|n,\vec{k};\eta,\vec{c}\rangle$, where $|n,\vec{k}\rangle$ represents the state vector of the electrons and $|\eta,\vec{c}\rangle$ represents the state vector of the phonons. In the adiabatic approximation, the state vector can be written as

$$|n,\vec{k};\eta,\vec{c}\rangle = |n,\vec{k}\rangle|\eta,\vec{c}\rangle. \tag{2.23}$$

The transition probability per unit time from an initial state $|n,\vec{k};\eta,\vec{c}\rangle$ to a final state $|n',\vec{k}';\eta',\vec{c}'\rangle$ as determined by the Fermi's golden rule is given by

$$P(n,\vec{k},\eta,\vec{c};n',\vec{k}',\eta',\vec{c}') = \frac{2\pi}{\hbar}\left|\langle n',\vec{k}',\eta',\vec{c}'|H'|n,\vec{k},\eta,\vec{c}\rangle\right|^2 \delta\left(E_{n'}(\vec{k}') - E_n(\vec{k}) \mp \hbar\omega_{\eta,q}\right). \tag{2.24}$$

The perturbation is assumed to be harmonic, and it is convenient to expand the Hamiltonian H' as a Fourier series,

$$H'(\vec{r},\vec{y}) = \frac{(2\pi)^{3/2}}{V}\sum_{\vec{q}} H''(\vec{q},\vec{y})\, e^{i\vec{q}\cdot\vec{r}}\,, \tag{2.25}$$

where V is the volume of the crystal and the Hamiltonian acts on the position $\vec{r}$ of the electron and the phonon displacement $\vec{y}$. The matrix element in Equation (2.24) for the transition rate becomes

$$\langle n',\vec{k}',\eta',\vec{c}'|H'|n,\vec{k},\eta,\vec{c}\rangle = \frac{(2\pi)^{3/2}}{V}\sum_{\vec{q}}\langle\eta',\vec{c}'|\, H''(\vec{q},\vec{y})\,|\eta,\vec{c}\rangle \int \Psi^*_{n,\vec{k}}(\vec{r})\, e^{i\vec{q}\cdot\vec{r}}\,\Psi_{n',\vec{k}'}(\vec{r})\, d^3r, \tag{2.26}$$

where the normalized Block states are given by

$$\Psi_{n,\vec{k}}(\vec{r}) = \frac{1}{\sqrt{N}} u_{n,\vec{k}}(\vec{r})\, e^{i\vec{k}\cdot\vec{r}} \tag{2.27}$$

and N is number of unit cells in the crystal.

The integral over all $\vec{r}$ can be expressed as an integral over the unit cell multiplied by the sum over all cells. This can be expressed as

$$\int \Psi^*_{n,\vec{k}}(\vec{r})\, e^{i\vec{q}\cdot\vec{r}}\,\Psi_{n',\vec{k}'}(\vec{r})\, d^3r = \sum_{\vec{R}} e^{i(\vec{k}-\vec{k}'+\vec{q})\cdot\vec{R}}\,\frac{1}{N}\int_{\text{cell}} u_{n',\vec{k}'}(\vec{r}\,'')\, u^*_{n,\vec{k}}(\vec{r}\,'')\, e^{i(\vec{k}-\vec{k}'+\vec{q})\cdot\vec{r}\,''}\, d^3r''. \tag{2.28}$$

The sum over the direct lattice vector $\vec{R}$ yields N if $\vec{k}-\vec{k}'+\vec{q}=\vec{G}$ or vanishes otherwise, where $\vec{G}$ is a reciprocal lattice vector and N is the number of unit cells in the crystal. Transitions corresponding to $\vec{G}=0$ are called "Normal" processes and those corresponding to $\vec{G}\neq 0$ are called "Umklapp" processes. The integral over the unit cell is given by the overlap integral

$$\zeta = \left| \int_{\text{cell}} d^3r \; u^*_{n,\vec{k}}(\vec{r}) \; u_{n',\vec{k}'}(\vec{r}) \; e^{i\vec{G}\cdot\vec{r}} \right|^2 , \tag{2.29}$$

The electron states $(n,\vec{k})$ and $(n',\vec{k}')$ determine whether the transition is normal or Umklapp. For electrons, intravalley transitions, in general, are normal process due to the small distance between $\vec{k}$ and $\vec{k}'$ compared to the extent of the Brillouin zone and the overlap integral in this case is close to unity [37]. Likewise, intervalley transitions can be Umklapp process because of the large values associated with $\vec{k}$ and $\vec{k}'$ and the difference $\vec{k}-\vec{k}'$ depends largely on the valleys involved in the transition. The overlap integral is almost constant within each type of intervalley transition and its value may be included in the coupling constants associated with each type of transition. Collecting these results, the transition rate becomes

$$P(n,\vec{k},\eta,\vec{c};n',\vec{k}',\eta',\vec{c}') = \frac{(2\pi)^4}{\hbar V^2} \left| \sum_{\eta,\vec{q}} \langle \eta',\vec{c}' |\, H''(\vec{q},\vec{y}) \,| \eta,\vec{c}\rangle \right|^2 \zeta \; \delta\left(E_{n'}(\vec{k}') - E_n(\vec{k}) \mp \hbar\omega_{\eta,\vec{q}}\right). \tag{2.30}$$

Further evaluation of the transition rate requires explicit forms of the Hamiltonian H'. The deformation potential tensor Ξ_{ij} relates the strain S_{ij} in the lattice to the perturbing Hamiltonian of the phonon interaction. The perturbing Hamiltonian is given by [37]

$$H' = \sum_{ij} \Xi_{ij} S_{ij} \tag{2.31}$$

The strain can be written as the derivative of the displacement of the unit cell [37]

$$S_{ij} = S_{ji} = \frac{1}{2}\left(\frac{\partial u_i}{\partial x_j} + \frac{\partial u_j}{\partial x_i}\right) \tag{2.32}$$

where $\vec{u}$ is the displacement of the unit cell. Further, the displacement can be written in terms of phonon creation and annihilation operators, $a^\dagger_{-\vec{q}}$ and $a_{\vec{q}}$, respectively. In the case of phonons the creation and annihilation operators create or destroy a quantum of energy

equal to that of a phonon in the crystal. The harmonic displacement in terms of the creation and annihilation operators is given by [37]

$$\vec{u} = \sum_{\vec{q}} \sqrt{\frac{\hbar}{2\rho V \omega_{\vec{q}}}} \left(a_{\vec{q}} + a^{\dagger}_{-\vec{q}} \right) \vec{\xi}\, e^{i\vec{q}\cdot\vec{r}} \tag{2.33}$$

where ρ is the crystal density, V is the volume of the unit cell, $\omega_{\vec{q}}$ is the phonon frequency, and $\vec{\xi}$ is the phonon polarization vector. Differentiating $\vec{u}$ with respect to $\vec{r}$, and substituting $d\vec{u}/d\vec{r}$ for the strain tensor yields the perturbing Hamiltonian:

$$H' = \sum_{\vec{q}} i \sqrt{\frac{\hbar}{2\rho V \omega_{\vec{q}}}} \left(a_{\vec{q}} + a^{\dagger}_{-\vec{q}} \right) \Xi_{ij}\, \vec{q}_i \cdot \vec{\xi}\, e^{i\vec{q}\cdot\vec{r}} \tag{2.34}$$

Deformation due to zone-center phonons in wurtzite GaN conserve the C^4_{6v} space-group's symmetry and the strain tensor takes the diagonal form [74]. Though the diagonal elements are not all equal, the differences are small and can be assumed to be equal [75]. This reduces the deformation potential tensor Ξ_{ij} to a scalar value Ξ. The Hamiltonian H' acts on only the initial and final states $|\eta, \vec{c}\rangle$, and $|\eta', \vec{c'}\rangle$ through the operators $a_{\vec{q}}$ and $a^{\dagger}_{-\vec{q}'}$ respectively. In the sum over $\vec{q}$, the matrix element vanishes for all but the following two cases

$$\left| \langle \eta', \vec{c'} |\, a_{\vec{q}}\, | \eta, \vec{c} \rangle \right|^2, \qquad \left| \langle \eta', \vec{c'} |\, a^{\dagger}_{-\vec{q}}\, | \eta, \vec{c} \rangle \right|^2 \tag{2.35}$$

corresponding to the absorption and emission of a phonon with wavevector $\vec{q} = \vec{k'} - \vec{k}$, respectively. The first matrix element is $N_{\eta,\vec{q}}(\hbar\omega_{\eta,\vec{q}})$, the number of phonons in the state $|\eta, \vec{c}\rangle$, and the second matrix element is $N_{\eta,\vec{q}}(\hbar\omega_{\eta,\vec{q}}) + 1$ [76]. In the special case of phonons in equilibrium with a reservoir at temperature T, $N_{\eta,\vec{q}}(\hbar\omega_{\eta,\vec{q}})$ is given by the Bose-Einstein distribution

$$N_{\eta,\vec{q}}(\hbar\omega_{\eta,\vec{q}}) = \left(e^{\frac{\hbar\omega_{\eta,\vec{q}}}{k_B T}} - 1 \right)^{-1} \tag{2.36}$$

Equation (2.34) is an explicit form of the Fourier series expansion of Equation (2.25). Substituting for the Fourier series expansion and noting that only the absorption and emission terms remain, the matrix element reduces to

$$\left| \langle n', \vec{k'}, \eta', \vec{c'} | H' | n, \vec{k}, \eta, \vec{c} \rangle \right|^2 = \frac{\hbar}{2\rho V \omega_q} \begin{bmatrix} N_{\eta,\vec{q}} \\ N_{\eta,\vec{q}} + 1 \end{bmatrix} \left| \Xi_{ij}\, \vec{q}_i \cdot \vec{\xi} \right|^2 \zeta, \tag{2.37}$$

and the transition rate becomes

$$S(n,\vec{k};n',\vec{k}') = \frac{\pi}{\rho V \omega_{\eta,\vec{q}}} \begin{bmatrix} N_{\eta,\vec{q}} \\ N_{\eta,\vec{q}}+1 \end{bmatrix} \left| \Xi_{ij}\, \vec{q}_i \cdot \vec{\xi} \right|^2 \zeta\, \delta\left(E_{n'}(\vec{k}') - E_n(\vec{k}) \mp \hbar\omega_{\eta,\vec{q}}\right), \tag{2.38}$$

where the upper and lower symbols correspond to absorption and emission, respectively. The total scattering from an initial state $|n,\vec{k}\rangle$ is obtained by summing over all final states that satisfy energy conservation. The total scattering rate due to the deformation potential interaction is given by

$$S(n,\vec{k}) = \frac{\pi}{\rho V} \sum_{\eta,\vec{q}} \frac{1}{\omega_{\eta,\vec{q}}} \begin{bmatrix} N_{\eta,\vec{q}} \\ N_{\eta,\vec{q}}+1 \end{bmatrix} \left| \Xi\, \vec{q} \cdot \vec{\xi} \right|^2 \zeta\, \delta\left(E_{n'}(\vec{k}') - E_n(\vec{k}) \mp \hbar\omega_{\eta,\vec{q}}\right). \tag{2.39}$$

The above equation can be applied to specific cases of intra- and inter-valley transitions due to optical and acoustic phonons. For the simplest case of intravalley scattering of electrons by optical phonons, the phonon wavelength can be assumed to equal the lattice constant due to the fact that atoms within the same unit cell vibrate in opposite directions. The scattering probability in this case can be written by replacing $\left|\Xi\,\vec{q}\right|^2$ with a squared optical coupling constant ${D_p}^2$ [37], which may include the overlap factor ζ. Since the intra-valley transition involves low energies and since the optical phonon dispersion at low energies is almost flat, the energy associated with the intra-valley optical phonon can be assumed to be a constant $\hbar\omega_{op}$. Likewise, the phonon occupation number also becomes a constant N_{op}. The resulting scattering rate is

$$S(n,\vec{k}) = \frac{\pi}{\rho V} \sum_{\vec{q}} \begin{bmatrix} N_{op} \\ N_{op}+1 \end{bmatrix} \frac{{D_p}^2}{\omega_{op}}\, \delta\left(E_{n'}(\vec{k}') - E_n(\vec{k}) \mp \hbar\omega_{op}\right), \tag{2.40}$$

with the upper and lower symbols corresponding to absorption and emission, respectively. Inter-valley transition of electrons due to acoustic and optical modes can also be treated similarly. The phonon wavevector $\vec{q}$ involved in an inter-valley transition is very close to the distance between the minima of the initial and final valleys due to the large separation of valleys within the Brillouin zone. For a given phonon mode between two valleys, the phonon energy and occupation number are almost constant as in the case of intra-valley scattering by optical phonons. Hence, the inter-valley scattering can be treated in the same way as intra-valley optical phonons. The squared coupling constant ${D_p}^2$ depends on the

initial and final valleys and the phonon mode involved in the transition and may include the overlap factor.

2.5.3.1 *Special case: Long-wavelength intra-valley longitudinal acoustic phonon scattering*

Intra-valley scattering of electrons by long-wavelength (small wave vector) longitudinal acoustic (LA) phonons is a special case of the deformation potential interaction. The flat phonon dispersion assumed in the previous section is no longer valid as the LA mode phonons have a linear dispersion at low energies [37]. In the sum over electron final-state vectors, both the phonon energy and the phonon occupation number are not constant, and correct expressions need to be included for calculating the scattering rate.

For LA mode phonons, it is convenient to use the longitudinal sound velocity v_s in the crystal as it is the slope the phonon dispersion curve:

$$v_s = \frac{\omega_{ac}}{|\vec{q}|}. \tag{2.41}$$

As explained in the previous sub-section, for zone-center phonons the deformation potential tensor reduces to a scalar and the overlap integral is close to unity. Applying these, and noting that the phonon mode η is fixed, the scattering rate becomes

$$S(n,\vec{k}) = \frac{\pi\Xi^2}{\rho v_s V} \sum_{\vec{q}} \begin{bmatrix} N_{\vec{q}} \\ N_{\vec{q}}+1 \end{bmatrix} |\vec{q}|\, \delta\left(E_{n'}(\vec{k'}) - E_n(\vec{k}) \mp \hbar\omega_{\vec{q}}\right). \tag{2.42}$$

$N_{\vec{q}}(\hbar\omega_{\vec{q}})$ can be expanded as a Taylor's series [37]

$$N(x) = \frac{1}{x} - \frac{1}{2} + \frac{x}{12} - \frac{x^3}{720} + \frac{x^5}{30240} + \cdots \tag{2.43}$$

where $x = \hbar\omega_{\vec{q}}/k_B T$. Substituting the expansion of $N_{\vec{q}}$, the scattering rate for absorption is

$$S(n,\vec{k}) = \frac{\pi\Xi^2}{\hbar\rho v_s^2 V} \sum_{\vec{q}} \left(1 \mp \frac{x}{2} + \frac{x^2}{12} - \frac{x^4}{720} + \frac{x^6}{30240} + \cdots\right) \delta\left(E_{n'}(\vec{k'}) - E_n(\vec{k}) \mp \hbar\omega_{\vec{q}}\right) \tag{2.44}$$

where $x = \hbar\omega_{\vec{q}}/k_B T$, and the upper and lower symbols correspond to absorption and emission, respectively. The summation over $\vec{q}$ can be transformed into an integral over $\vec{k'}$ using [50]

$$\frac{1}{V}\sum_{\vec{q}} \rightarrow \int \left(\frac{1}{2\pi}\right)^3 d^3k'. \tag{2.45}$$

The final scattering rate in

$$S(n,\vec{k}) = \frac{1}{4\pi^2}\,\frac{\Xi^2 k_B T}{\hbar\rho v_s^2}\int_{\vec{q}}\left(1 \mp \frac{x}{2} + \frac{x^2}{12} - \frac{x^4}{720} + \frac{x^6}{30240} + \cdots\right)\delta\left(E_{n'}(\vec{k'}) - E_n(\vec{k}) \pm \hbar\omega_{\vec{q}}\right)d\vec{k} \tag{2.46}$$

where $x = \hbar\omega_{\vec{q}}/k_B T$ & $\vec{q} = \vec{k'} - \vec{k}$.

The above derivation and its implementation are verified by numerically evaluating the scattering rate on an hypothetical material with perfectly-parabolic bandstructure so that the scattering rate can be compared with analytic expression derived using simplifying assumptions. When $\hbar\omega << k_B T$, all higher order terms of the integrand become small and can be ignored (equipartition approximation). The absorption and emission rates are comparable ($N_{\vec{q}} >> 1$, $N_{\vec{q}} \approx N_{\vec{q}} + 1$) and the integral reduces to the density of states expression. Assuming a parabolic band, the total scattering rate due to both absorption and emission reduces to

$$S(n,\vec{k}) = 2\,\frac{\Xi^2 k_B T\sqrt{2m^{*3}}}{4\pi^2\hbar^4\rho v_s^2}\sqrt{E_n(\vec{k})} \tag{2.47}$$

The parameter values of the hypothetical material used to estimate the scattering rate are

$$\rho = 6150 \text{ Kg/m}^3$$

$$v_s = 8000 \text{ m/s}$$

$$m* = 0.18 m_0 \text{ Kg}$$

$$\Xi = 4.5 \text{ eV}$$

The accuracy of the numerical implementation is evaluated by populating the $\vec{k}$ space grid with energy values of the perfectly-parabolic band and computing the rates in the Γ valley under the same approximations used in Equation (2.47). Figure 1 shows the numerically integrated scattering rates, which are in excellent agreement with the rates computed using Equation (2.47). Figure 2.2 also shows the rate computed using the same parabolic band, but using several terms of the integrand and using $N_{\vec{q}}$ and $N_{\vec{q}} + 1$ terms for absorption and emission respectively. This exercise demonstrates that the equipartition approximation is indeed very good at low energies.

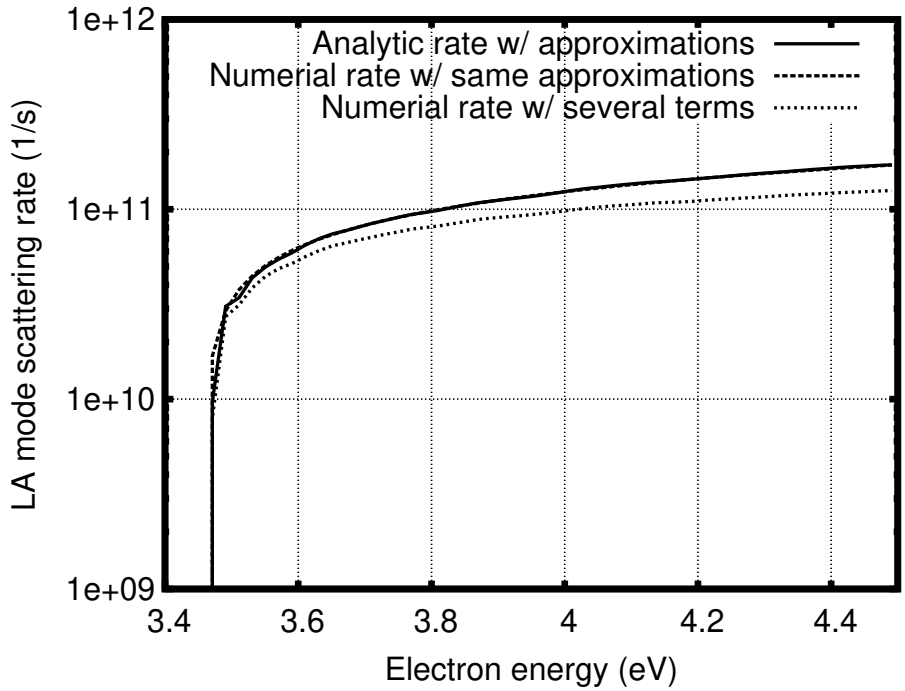

Figure 2.2: Longitudinal acoustic phonon scattering rate in the Γ valley of an hypothetical material.

2.5.4 Polar-optical phonon scattering

In polar materials like GaN, in addition to the deformation potential interaction described in the previous section, the vibrations of oppositely charged atoms give rise to long-range macroscopic perturbation of the crystal potential, which causes additional scattering referred to as the Fröhlich interaction. When the vibrations of the differently charged atoms are in opposite directions, the frequency of oscillations is very high and these vibrations are called polar-optical phonons. The polar-optical phonon (POP) interaction is the dominant scattering mechanism in GaN. In wurtzite GaN the electron-phonon coupling through the Fröhlich interaction involves both longitudinal-optical (LO) and transverse-optical (TO) modes [77, 78]. The Fröhlich Hamiltonian is derived using the macroscopic dielectric continuum model and the uniaxial model of Loudon [79].

Ionic vibrations of the polar-optical phonons can generate electric fields and affect the dielectric function $\epsilon(\omega)$. Taking the c axis along the z direction and denoting the basal plane

as $\perp$, the direction-dependent dielectric functions $\epsilon_\perp(\omega)$ and $\epsilon_z(\omega)$ are given by [77]

$$\epsilon_\perp(\omega) = \epsilon_\perp^\infty \frac{\omega^2 - \omega_{\perp \mathrm{L}}^2}{\omega^2 - \omega_\perp^2}, \tag{2.48}$$

$$\epsilon_z(\omega) = \epsilon_z^\infty \frac{\omega^2 - \omega_{z\mathrm{L}}^2}{\omega^2 - \omega_z^2}, \tag{2.49}$$

where $\omega_\perp$ (ω_z) is the TO phonon frequency, $\omega_{\perp \mathrm{L}}$ ($\omega_{z\mathrm{L}}$) is the LO phonon frequency, and $\epsilon_\perp^\infty$ (ϵ_z^∞) is the high-frequency dielectric constant perpendicular to (along) the c axis. The corresponding static dielectric constants are given by $\epsilon_\perp^0 = \epsilon_\perp^\infty \omega_{\perp \mathrm{L}}^2/\omega_\perp^2$ and $\epsilon_z^2 = \epsilon_z^\infty \omega_{z\mathrm{L}}^2/\omega_z^2$.

The allowed optical phonon modes satisfy the classical electrostatic equations, which when combined with the equations describing the stress and strain in the medium, fully describe the Fröhlich interaction. In the absence of free charge:

$$\nabla \cdot \vec{D}(\vec{r}) = 0, \tag{2.50}$$

where $\vec{D}(\vec{r}) = \epsilon_0 \vec{E}(\vec{r}) + \vec{P}(\vec{r})$ is the electric displacement and $\vec{P}$ is the polarization. For a traveling wave with wavevector $\vec{q}$, Equation (2.50) reduces to

$$\vec{q} \cdot \vec{D}(\vec{r}) = 0. \tag{2.51}$$

With finite $\vec{q}$, two categories of solution are possible:

$$\vec{D}(\vec{r}) = 0 \text{ (longitudinal)}, \tag{2.52}$$

$$\vec{D}(\vec{r}) \neq 0 \text{ (transverse)}. \tag{2.53}$$

For long wavelengths the polarization is related to the longitudinal ionic displacement $\vec{u}(\vec{r})$ by

$$\vec{P}(\vec{r}) = \frac{e^* \vec{u}(\vec{r})}{V_0}, \tag{2.54}$$

where e^* is the effective ionic charge and V_0 is the volume of the unit cell. With $\vec{D}(\vec{r}) = 0$, the electric field corresponding to the LO mode becomes

$$\vec{E}(\vec{r}) = \frac{-e^* \vec{u}(\vec{r})}{\epsilon_0 V_0}. \tag{2.55}$$

The scalar potential $\phi(\vec{r})$ associated with this field is the basis of the Fröhlich interaction.

The solution for $\phi(\vec{r})$ can be obtained by assuming a harmonic dependence in space and time and applying the macroscopic equations of motion to relate $\vec{E}(\vec{r})$ and $\vec{u}(\vec{r})$ [77]. The allowed phonon modes satisfy

$$\epsilon_{\perp}(\omega)\sin^2\theta + \epsilon_z(\omega)\cos^2\theta = 0, \tag{2.56}$$

where θ is angle between the phonon wavevector $\vec{q}$ and the z axis. The Hamiltonian is given by

$$H = \sum_{\vec{q}} -e\,\phi(\vec{q})\,e^{i\vec{q}\cdot\vec{r}}\,(a_{\vec{q}} + a^{\dagger}_{-\vec{q}}), \tag{2.57}$$

where $\phi(\vec{q})$ is the Fourier transform of $\phi(\vec{r})$ and $a^{\dagger}_{-\vec{q}}$ and $a_{\vec{q}}$ are the creation and annihilation operators, respectively. The Hamiltonian acts on only the initial and final states through the creation and annihilation operators as outlined in the previous section. Expanding the Hamiltonian [80] and summing over all states yields the matrix elements [77]. For the TO mode, the solution of Equation (2.56) $\omega = \Omega_{\mathrm{T}}$ is

$$\Omega_{\mathrm{T}}^2 = \omega_z^2\,\sin^2\theta + \omega_{\perp}^2\cos^2\theta, \tag{2.58}$$

and the matrix element is given by [77]

$$|M_{\vec{q}}^{\mathrm{T}}|^2 = \frac{2\pi e^2\hbar}{Vq^2\,\Omega_{\mathrm{T}}}\,\frac{(\omega_{\perp}^2-\omega_z^2)^2\,\sin^2\theta\,\cos^2\theta}{(\epsilon_{\perp}^2-\epsilon_{\perp}^{\infty})\,\omega_{\perp}^2\cos^2\theta + (\epsilon_z^2-\epsilon_z^{\infty})\,\omega_z^2\sin^2\theta} \times \begin{bmatrix} N_{\vec{q}} \\ N_{\vec{q}}+1 \end{bmatrix}, \tag{2.59}$$

where $N_{\vec{q}}$ is the phonon occupation number and the upper and lower terms correspond to phonon absorption and emission, respectively. Similarly for the LO mode, the solution of Equation (2.56) $\omega = \Omega_{\mathrm{L}}$ is

$$\Omega_{\mathrm{L}}^2 = \omega_{z\mathrm{L}}^2\,\cos^2\theta + \omega_{\perp\mathrm{L}}^2\sin^2\theta, \tag{2.60}$$

and the matrix element is given by [77]

$$|M_{\vec{q}}^{\mathrm{L}}|^2 = \frac{2\pi e^2\hbar}{Vq^2\,\Omega_{\mathrm{L}}}\left[\frac{\sin^2\theta}{(1/\epsilon_{\perp}^{\infty}-1/\epsilon_{\perp}^{0})\,\omega_{\perp\mathrm{L}}^2} + \frac{\cos^2\theta}{(1/\epsilon_z^{\infty}-1/\epsilon_z^{0})\,\omega_{z\mathrm{L}}^2}\right]^{-1} \times \begin{bmatrix} N_{\vec{q}} \\ N_{\vec{q}}+1 \end{bmatrix}, \tag{2.61}$$

where $N_{\vec{q}}$ is the phonon occupation number and the upper and lower terms correspond to phonon absorption and emission, respectively. The total scattering rate is computed by using Fermi's golden rule and summing over all final states as described in the previous section.

The phonon frequencies for wurtzite GaN are obtained from experimental measurements [77, 78, 81]: $\hbar\omega_z = 66.08$ meV, $\hbar\omega_{zL} = 91.13$ meV, $\hbar\omega_\perp = 69.55$ meV, and $\hbar\omega_{\perp L} = 92.12$ meV. Since ϵ^∞ is due to only electrons with no ionic contribution, ϵ_z^∞ and $\epsilon_\perp^\infty$ are taken to be equal. The dielectric constants are $\epsilon_\perp^0 = 9.28$, $\epsilon_z^0 = 10.1$, and $\epsilon_z^\infty = \epsilon_\perp^\infty = 5.29$ [77]. It has been confirmed that the TO mode scattering rate is more than two orders of magnitude weaker than the LO mode over the entire extent of the Brillouin zone [78] and its contribution can be omitted. Also, the scattering rate due to LO mode phonons is insensitive to the angle θ [77]. Thus, the direction dependence of the total scattering rate due to the Fröhlich interaction in wurtzite GaN is small and the Hamiltonian of the cubic interaction is a good approximation [77, 78].

2.6 Solution of the Poisson equation

The Poisson equation provides the relation between the electrostatic potential ϕ and the charge density ρ.

$$\nabla \cdot [\epsilon(x, y)\, \nabla\phi(x, y)] = -[\rho(x, y) + \rho^{pol}], \tag{2.62}$$

where $\rho(x, y)$ is the three-dimensional charge density in C/m^3, $\epsilon(x, y)$ is the permittivity tensor, and ρ^{pol} is given by,

$$\rho^{pol} = -\nabla\sigma, \tag{2.63}$$

where σ is the polarization-induced sheet charge density.

The Monte Carlo simulator solves the Poisson equation by means of a finite volume discretization scheme. The electric field profile derived from the electrostatic potential is used to propagate the particles, which in turn affects the charge distribution, making the process self-consistent. The Poisson equation is solved synchronously at sub-femto second intervals [82]. The solver works on the same real space irregular grid that is used for particle propagation. The applied bias on the device contacts are used as the Dirichlet boundary conditions for the Poisson equation, and all other device boundaries are treated as von-Neumann boundaries. In the case of the AlGaN/GaN material system, the appropriate mole-fraction dependent polarization charges [21] is also applied at the top, bottom, and internal material interfaces. The solver uses an efficient sparse matrix solver and the

nodes are reordered using the Reverse Cuthill-McKee (RCM) minimum degree ordering algorithm [83, 84] to reduce the connectivity of the grid. Node reordering, polarization charge assignment, and LU factorization steps are performed only once, while the potential profile is computed efficiently for time-dependent changes to charge distribution by means of simple backfill operations.

2.7 Estimators

Information about physical quantities such as velocity, energy, density, etc., are collected over the duration of the simulation. A set of "estimators" are used to compute averages and variances of the collected data. Instantaneous charge density is required for the synchronous, self-consistent solution of the Poisson equation. Time averaged quantities such as the energy loss rate are also calculated for use in the self-consistent solution of the thermal equation.

The physical quantities are collected on the vertices of the real space grid. A Cloud-in-Cell [85] algorithm is used to distribute the contribution of the observable quantity to the three vertices of the real space element. Particles are assigned weights denoting their relative statistical significance. This is required for representing fractional number of particles corresponding to arbitrary charge densities. The nearest whole number of particles are created with fractional weights such that the sum of the weights equal the total fractional number of particles. A particle's contribution to the estimators is scaled by its weight. It is important for the weights to be close to unity, as particles with small weight contribute very little to the estimators, and particles with large weight exert disproportional influence; both of these situations result in higher statistical variance of the estimators, and longer simulation times. For this reason, the particle weights are monitored in the Ohmic buffer regions where particles are continually created or removed to maintain charge neutrality. When the distribution of weights exceed a preset threshold, the weights are redistributed between the nearest whole number of particles. For example, if the total number of particles required is 8.32, the redistribution will leave 8 particles with a weight of 1.04 each. New particles may be created or excess particles may be removed to achieve this.

The terminal currents in a device with arbitrary geometry are estimated by using the Ramo-Shockley theorem [86]. For a device with N_c contact, N_e electrons, and N_h holes, the instantaneous current I_k flowing into a terminal k is given by

$$I_k = -\left[-q\sum_{j=1}^{N_e}\vec{v}_{e_j}\cdot\nabla h_k(\vec{r}_j) + q\sum_{l=1}^{N_h}\vec{v}_{h_l}\cdot\nabla h_k(\vec{r}_l) + \sum_{\substack{m=1\\m\neq k}}^{N_c} C_{mk}V'_{mk}\right], \tag{2.64}$$

where,

$$\begin{aligned}
\vec{v}_{e_j} &= \text{Velocity of the } j^{th} \text{ electron,}\\
\vec{v}_{h_l} &= \text{Velocity of the } l^{th} \text{ hole,}\\
\vec{r}_{e_j} &= \text{Position of the } j^{th} \text{ electron,}\\
\vec{r}_{h_l} &= \text{Position of the } l^{th} \text{ hole,}\\
C_{mk} &= \text{Capacitance between contacts } m \,\&\, k, \text{ and}\\
h_k(\vec{r}) &= \text{Harmonic function associated with } k^{th} \text{ contact.}
\end{aligned}$$

The harmonic function, also known as the test function, is defined such that

$$\begin{aligned}
\nabla^2 h_k(\vec{r}) &= 0, \text{ with the boundary conditions}\\
h_k(\vec{r}) &= 1 \text{ on contact } k\\
&= 0 \text{ on all other contacts.}
\end{aligned} \tag{2.65}$$

2.7.1 Device Boundaries

Propagation of particles at the device boundaries require special treatment. Particles incident on external device boundaries are reflected back into the device. The particle is reflected such that the component of its crystal momentum tangential to the external edge is conserved, while the normal component is reversed. The $\vec{k}$-state after reflection is found by searching the Brillouin zone for a matching isoenergy state with the required tangential and normal components of crystal momentum. Heterojunction interfaces are handled in a similar manner while accounting for the band offsets. Particles with energy less than the barrier height are reflected similar to reflection performed at external boundaries, while

particles with energy higher than the barrier are transmitted into the new material. The $\vec{k}$-state in the new material is again found by searching the Brillouin zone of the new material for a state meeting the energy and momentum constraints.

Ohmic contacts are modeled by a charge neutral buffer region with very high particle density. Charge neutrality is rigorously enforced at sub femto-second time scales by creating or removing particles within the elements of the Ohmic region. Particles weights are also conditionally redistributed to enforce accurate charge neutrality, and to reduce the variance of the particle weight distribution. Electrostatic boundary conditions are applied at the boundary of device domain and Ohmic buffer regions, so that the electrostatics inside the device remain unaffected, and proper boundary conditions are presented to the Poisson solver. Particles are allowed to freely enter and exit the Ohmic region, closely modeling a real Ohmic contact.

CHAPTER III

SIMULATION AND CALIBRATION OF TRANSPORT IN BULK GAN

In this chapter, the study and calibration of charge transport in bulk GaN through Monte Carlo simulation are presented. The chapter begins with a brief review of the previous studies of transport in bulk GaN. This is followed by the details of transport parameter calibration and a discussion of the results. Finally, a study of temperature and doping dependence of mobility in bulk GaN is presented.

3.1 Review

Monte Carlo study of the fundamental aspects of electron and hole transport in bulk wurtzite GaN has been performed by many groups. Several aspects of transport in bulk GaN have been independently investigated including high-field transport, stationary and transient phenomena such as velocity overshoot and ballistic transport, anisotropy of transport, influence of defects and impurities, and hot carrier effects.

Experimental measurements of temperature and doping dependent electron mobility in bulk wurtzite GaN have been presented in [87, 88]. Kolnik *et al.* have performed full band Monte Carlo calculation of stationary electron transport in bulk wurtzite GaN using four conduction bands [31], while Oguzman *et al.* have performed the same for hole transport in wurtzite GaN [89]. Albrecht *et al.* studied the temperature, field strength, and doping dependence of electron mobility in wurtzite GaN using a Monte Carlo model, and derived analytical expressions for mobility as a function of temperature and doping concentration using parameters determined from the Monte Carlo results [33]. Foutz *et al.* studied transient electron transport in wurtzite GaN using partial band Monte Carlo simulations [90]. Barker *et al.* built test structures with an etched construction to determine velocity-field characteristics of bulk GaN at high-field strengths using a pulsed input, four point measurement system. Their measured velocity-field profile was compared favorably

with the Monte Carlo results of Kolnik *et al.* [31].

Wraback *et al.* performed experimental measurements and theoretical Monte Carlo calculations of transient electron velocity overshoot in bulk GaN [91]. Wraback *et al.* also investigated the direction dependence of high-field transient electron transport in GaN [92]. O'Leary *et al.* have published a review of the steady-state and transient electron transport within III-Nitride semiconductors [93].

However, a well calibrated model that includes all the relevant effects for the electrothermal study of high-field transport is still lacking. In the present research, a comprehensive transport model is developed incorporating full GaN bandstructure and the effects of scattering interactions with phonon, defects, and impurities. All significant phonon modes are considered and the non-equilibrium phonon population is self-consistently calculated. Up to ten conduction bands and eight valence bands are included to allow modeling transport at high-field strengths. The transport parameters were calibrated to match experimental measurements of mobility and drift velocity. Using the model, several important aspects of transport such as anisotropic stationary and transient electron velocity, and temperature and doping dependence of mobility are studied. The results are presented in the remainder of this chapter.

3.2 Stationary electron velocity

Monte Carlo simulation of transport in bulk GaN was performed to calibrate scattering rate parameters at room temperature. The influence of both the polar optic and deformation potential electron-phonon interactions were considered and the calibrated scattering rates are shown in Figures 3.1 & 3.2, where the reference energy level is the valence band maxima. The bulk device was set up using an one element real space grid as the bulk transport quantities are spatially invariant. A static electric field was applied, and the device orientation matrix was used to study transport along different directions in the crystal.

Steady-state electron drift velocity was calculated as a function of electric field for transport in both the basal plane the *c*-axis, and were compared with previously reported values [94]. The scattering rate parameters were adjusted to obtain a good match. Calculations

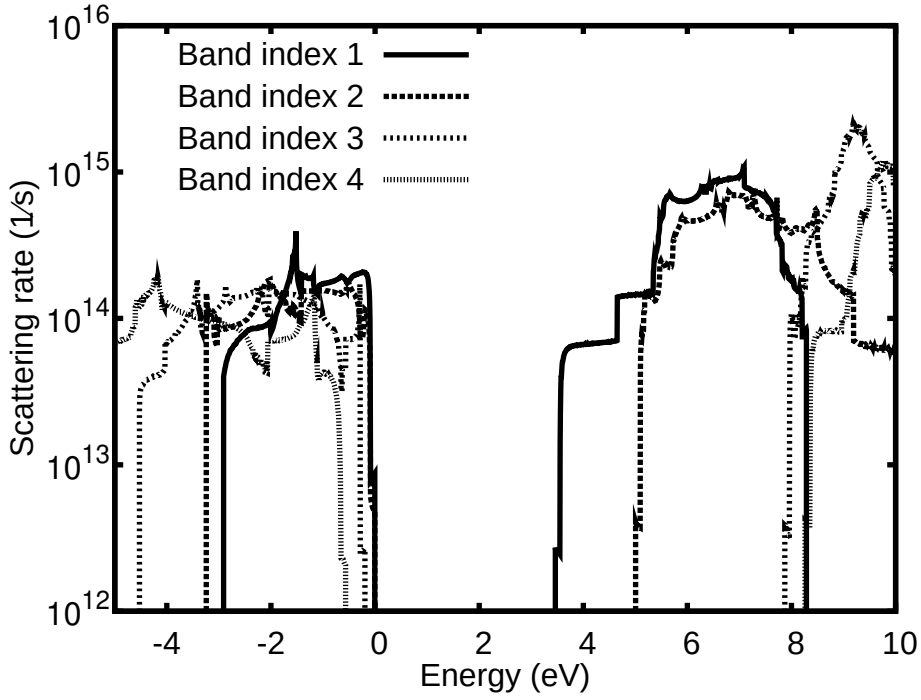

Figure 3.1: Calibrated polar optic phonon scattering rate for electrons and holes.

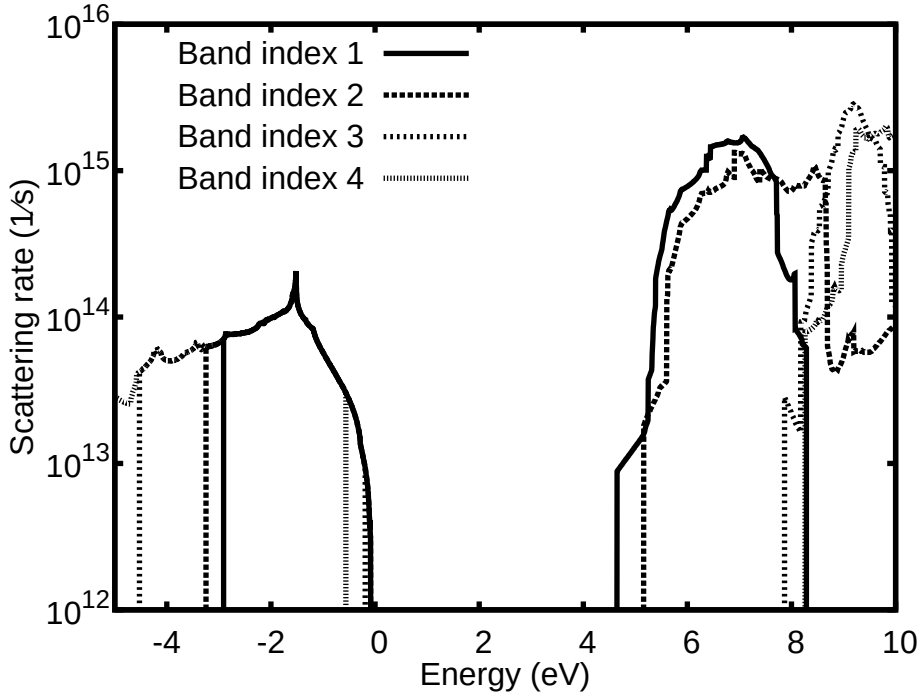

Figure 3.2: Calibrated deformation potential scattering rate for electrons and holes.

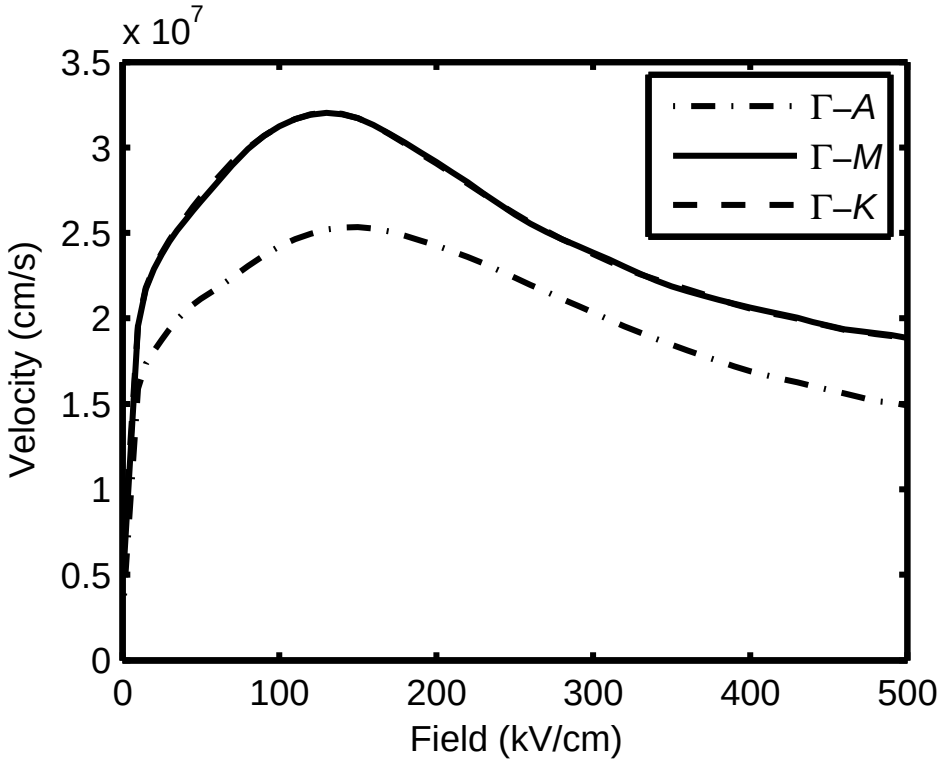

Figure 3.3: Calibrated steady-state electron drift velocity in bulk GaN as a function of field strength for different crystal orientations

of steady-state drift velocity are presented in Figure 3.3, as a function of field strength and crystal orientation. Peak drift velocities are reached at field strengths of 150 kV/cm in the $\Gamma \rightarrow A$ direction and 110 kV/cm in the $\Gamma \rightarrow M$ and $\Gamma \rightarrow K$ directions. Significantly, both: 1) peak electron velocity; and 2) saturated electron velocity are higher for transport in the basal plane than along the *c*-axis. This finding is exactly opposite to previously reported results [92] based on different band structures [68, 95].

Simulation of transient electron velocity was also performed in bulk GaN. Figures 3.4 and 3.5 show the transient evolution of electron velocity in bulk material for electric fields of various magnitudes, applied instantaneously at time $t = 0$ in the $\Gamma \rightarrow A$ and $\Gamma \rightarrow M$ directions. Simulations reveal that peak velocity overshoot occurs slightly earlier for transport along the *c*-axis, but the magnitude of the peak is significantly higher for transport within the basal plane. It is also interesting to consider the time integral of the transient electron velocity, shown in Figure 3.6, from the point of view of its influence on intrinsic

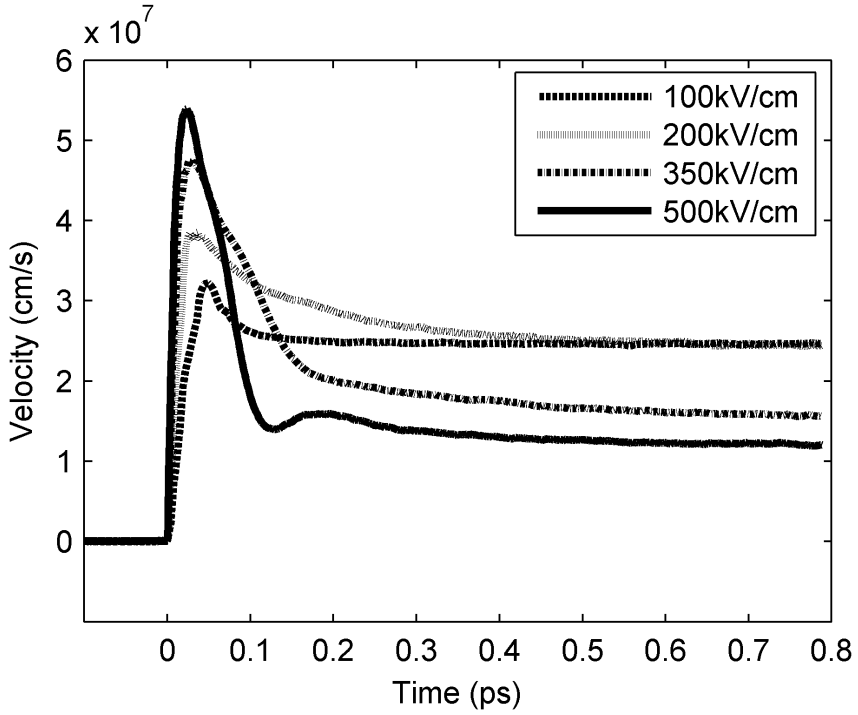

Figure 3.4: Transient velocity overshoot for a field applied along the $\Gamma \rightarrow A$ direction

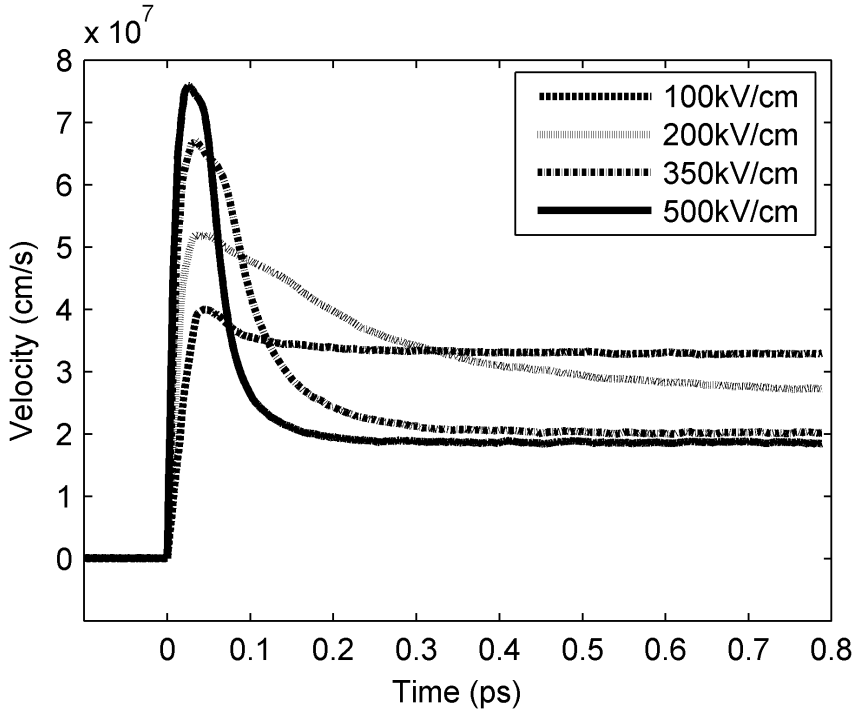

Figure 3.5: Transient velocity overshoot for a field applied along the $\Gamma \rightarrow M$ direction

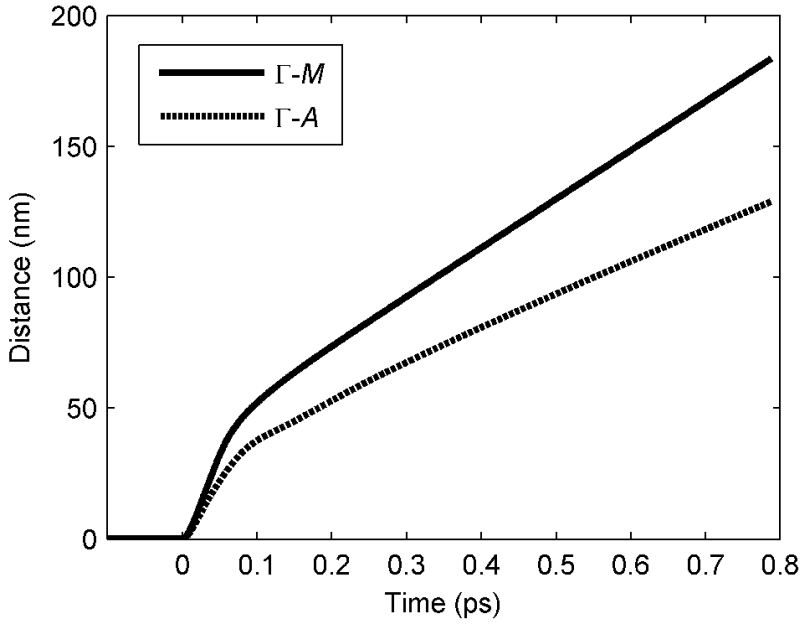

Figure 3.6: Time-integrated transient electron velocity suggests transit-time advantages for devices designed with charge transport oriented perpendicular to the *c*-axis.

transit time in GaN-based high-voltage switches and power amplifiers. Clear advantages are indicated for charge transport perpendicular to the *c*-axis.

Electron group velocity within the Γ valley of the first conduction band is shown in Figure 3.7 as a function of energy along the $\Gamma \rightarrow M$ and $\Gamma \rightarrow A$ directions, based on the calculations of several authors. As described in [92], the position of peak group velocity corresponds to the point in the Γ valley where the concavity of the band changes, leading to the onset of negative effective mass. Group velocity exhibiting a steeper dependence on energy (at low energies) for transport along the $\Gamma \rightarrow M$ direction than along the *c*-axis indicates a smaller effective mass in the former direction.

The higher peak group velocity for transport along the $\Gamma \rightarrow M$ direction leads directly to the higher peak transient overshoot velocity. As electrons in the transient simulations start from a thermal distribution, the occurrence of peak group velocity at higher energy for the case of transport along the $\Gamma \rightarrow M$ direction results in the longer time required to reach peak velocity. For transport in the $\Gamma \rightarrow A$ direction, peak group velocity occurs at a lower energy, leading to the onset of velocity overshoot at lower fields and on shorter time scales.

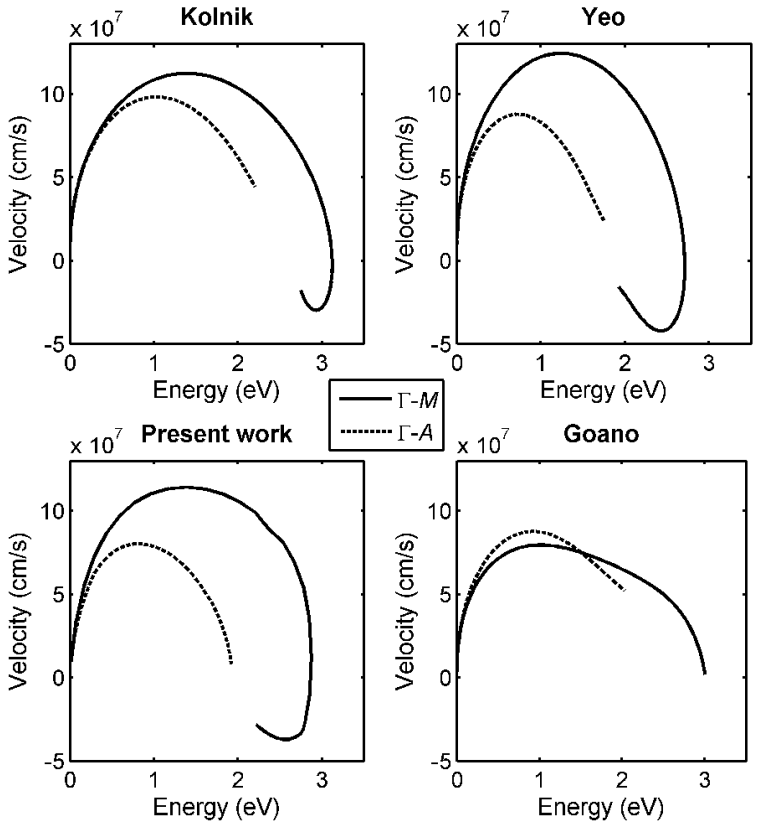

Figure 3.7: Electron group velocity versus energy, extracted from electronic dispersion published by Kolnik *et al.* [31], Yeo *et al.* [70], and Goano *et al.* [95], and calculated directly from the dispersion used in this study.

However, the significantly higher peak group velocity along the $\Gamma \rightarrow M$ direction more than compensates for both the delay in reaching overshoot and the higher fields required to produce overshoot. At lower fields, even with little or no transient overshoot, transport in the basal plane is still faster than along the *c*-axis due to the higher stationary velocities. These trends suggest a clear transit-time advantage for electron devices exploiting charge transport perpendicular to the *c*-axis.

3.3 Temperature and doping dependence

The performance of high-power GaN HEMTs used in micro- and millimeter-wave applications is limited by parasitic thermal effects, as channel electron mobility is degraded through Joule heating [96]. The dependence of electron mobility on temperature and

dopant density is important for device design, and has been experimentally measured by several authors [97–99]. Monte Carlo calculations of temperature dependent electron transport in GaN based on an analytic, isotropic multi-valley bandstructure model have been previously reported [33]. Recent full-bandstructure Monte Carlo investigations of stationary and transient electron velocity in bulk GaN at room temperature indicate the significance of anisotropy [100].

In this section, the temperature and doping dependence of steady-state electron velocity in bulk wurtzite GaN by means of full-band Monte Carlo charge transport simulation is presented. The simulation includes models appropriate for a wide range of ambient temperatures and free-carrier densities. The anisotropy and high-field effects of electron transport at elevated temperatures, for which experimental data is scarce, are also studied. These results provide valuable new insight into electron transport for high-performance device design.

A non-equilibrium population of LO phonons is computed and applied self-consistently to all simulations, based on stochastic emission and absorption events as well as LO phonon lifetime [101–103], which itself depends on free electron density through the plasmon-phonon interaction. The occupation number of all other phonon modes is assumed to be described by a single temperature. In this section, the Monte Carlo model is used to study the dependence of electron velocity on lattice temperature, free carrier density, dopant density, and field orientation, explicitly considering the temperature-dependence of partial ionization.

Calculations of electron drift mobility along the $\Gamma \rightarrow M$ direction as a function of donor concentration were performed at room temperature (300K). An activation energy of 25meV was used for the Si donors [98, 104] and a constant compensation ratio of 0.2 was assumed. A screw dislocation density of $10^9/\text{cm}^2$ was used and the edge dislocation density was assumed to be negligible. The low field drift mobilities were calculated by isothermal ensemble Monte Carlo simulation. Electron drift velocity was estimated by sampling group velocity for over 6ms, and the standard deviation of the estimator was two orders of magnitude smaller than the calculated drift velocity. A small number of

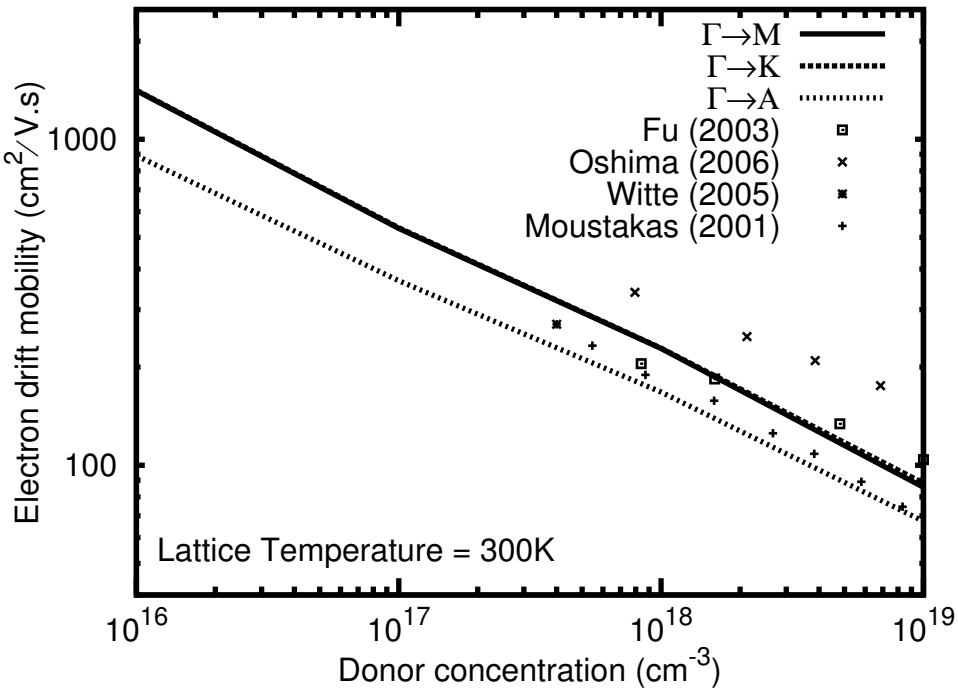

Figure 3.8: Low-field electron mobility degrades as a function of increasing donor concentration with no noticeable anisotropy within the basal plane. Mobility along the c-axis is consistently lower at all concentrations.

electron-phonon deformation potentials were treated as adjustable parameters for the calibration of low-field electron mobility to experimental measurement. Results are presented in Figure 3.8, in which measured Hall mobilities [97–99, 105] were converted into drift mobilities using appropriate Hall factors [99]. Simulated mobilities are in good agreement with experimental values, with the lower measured values corresponding to samples with high dislocation density. Simulations indicate that low-field mobility is nearly isotropic within the basal plane. Mobility along the *c*- axis, however, is slightly lower for all donor concentrations, and is directly attributable to the higher electron effective mass along this direction. Figure 3.9 shows the calculated electron drift velocity in the basal plane as a function of field strength at 300K for different donor concentrations, which is in good agreement with values reported in [106] for low donor concentrations. At low field strengths, a pronounced decrease in electron group velocity is observed with increasing dopant density. At high field strengths, the influence of ionized impurities on saturated drift velocity is far less severe, and consistent with the reduction in Coulombic scattering cross-section

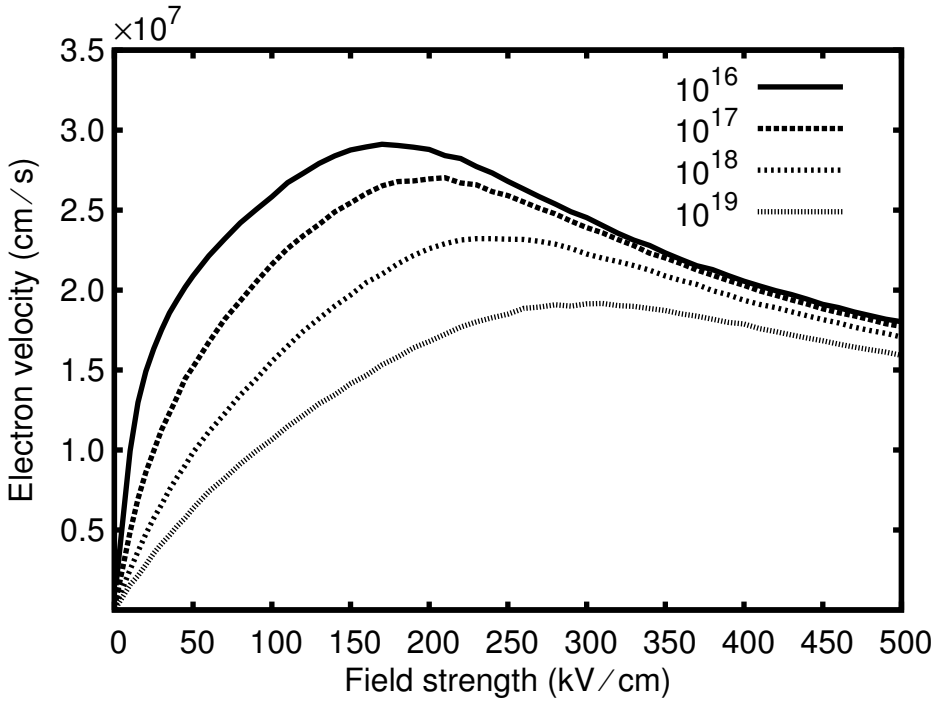

Figure 3.9: Electron group velocity for transport in the basal plane as function of field strength for various donor concentrations. T = 300K.

with increasing electron energy. With increasing ionized impurity density, Figure 3.9 also demonstrates an upward shift in the electric field strength required to achieve peak electron velocity, as well as a substantial degradation of peak electron velocity itself.

At moderate doping densities, simulations indicate that peak low-field mobility in the basal plane is achieved at 150K, the temperature at which the influences of Coulombic and electron-phonon scattering are comparable. This result, illustrated in Figure 3.10 and obtained using simulation parameters matching the experimental conditions, is in good agreement with the reported Hall measurements [98]. For transport along the *c*- axis, and in the limit of moderate dopant density, electron mobility is consistently lower than in the basal plane, and peaks at the same temperature. Figure 3.11 shows electron drift velocity as a function of field strength for lattice temperatures between 300K and 600K.

In HEMT structures, unlike transport in bulk materials, the free carrier density in the channel is significantly higher than the level of background dopants and the effect of ionized impurity and dislocation scattering is diminished due to increased screening by

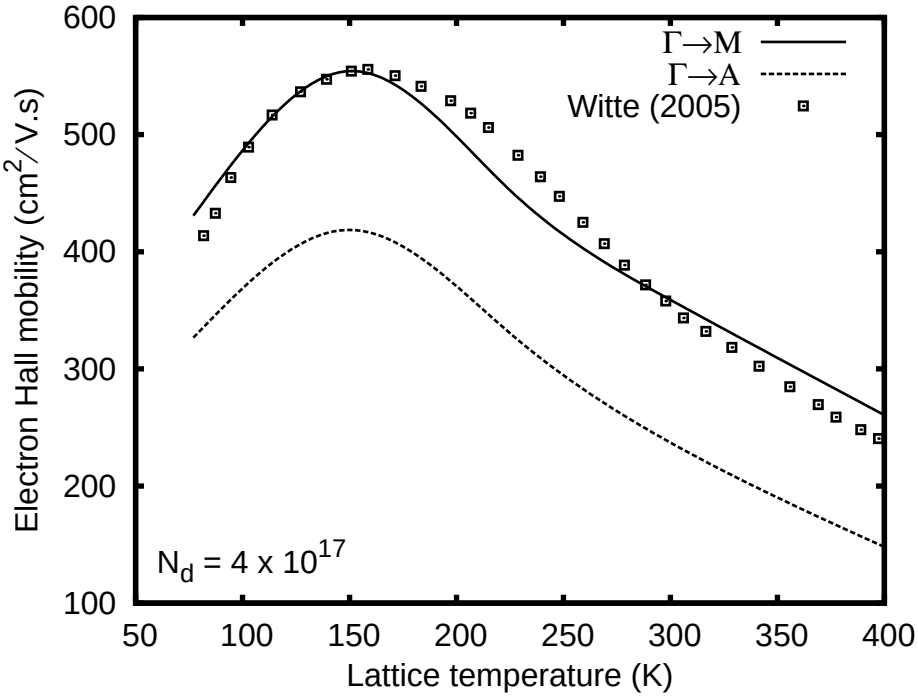

Figure 3.10: Electron mobility as a function of lattice temperature peaks at 150K at moderate dopant levels for transport in the basal plane, while the mobility for transport along the *c*-axis is consistently lower.

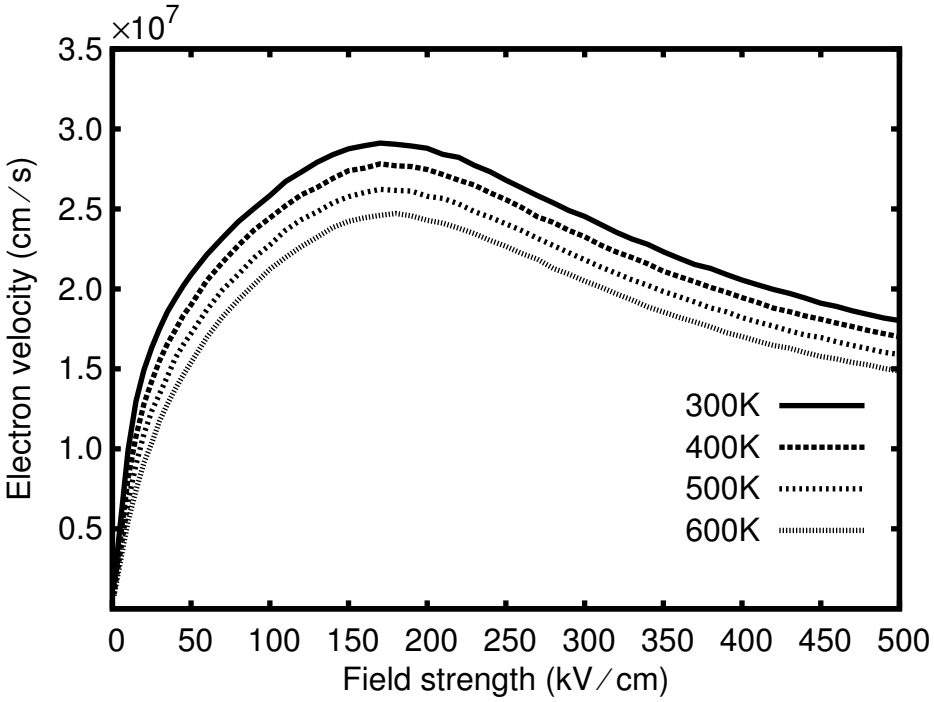

Figure 3.11: The reduction in electron drift velocity with ambient temperature is slightly more pronounced around 180kV/cm than at other field strengths.

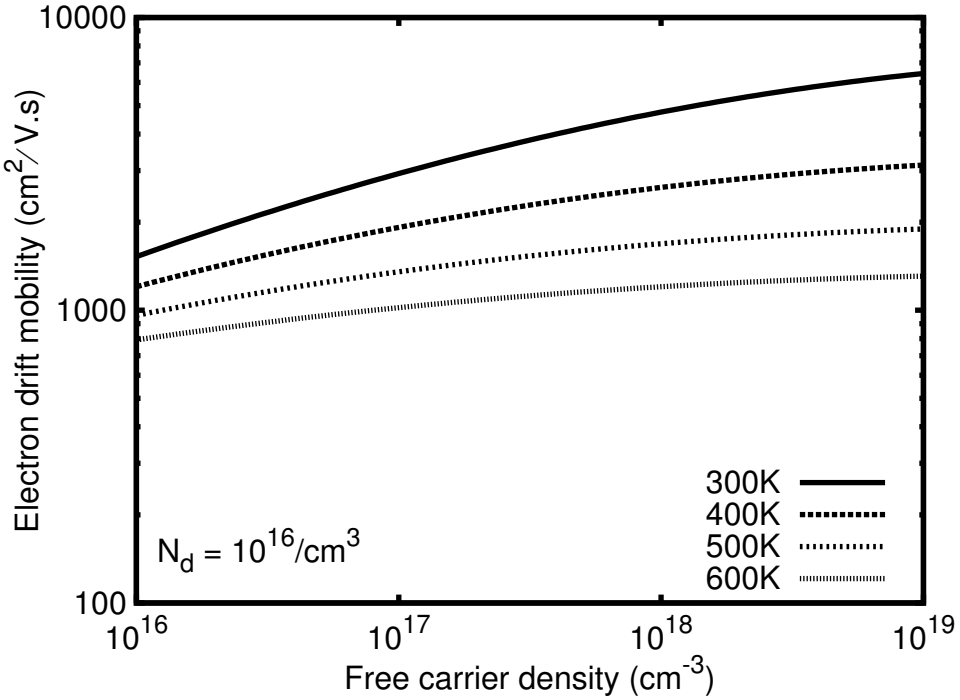

Figure 3.12: Enhancement of low-field electron mobility with increasing free-carrier density is diminished at high ambient temperature.

the free carriers. The related effect of variations in the free-carrier density on bulk electron mobility is modeled, holding the background doping fixed at $10^{16}/cm^3$ and the dislocation density fixed at $10^9/cm^2$. Results are depicted in Figure 3.12. The lifetime of LO phonons is a strong function of free-carrier density due to plasmon-assisted decay. Electron mobility at an ambient temperature of 300K improves significantly with increasing free-carrier density due to more effective screening of the ionized impurities. At elevated temperatures, the rise in mobility with free-carrier density is less pronounced due to the greater impact of electron-phonon interactions through the deformation potential interaction, in spite of the role of plasmons in the reduction of LO phonon lifetime.

This study of transport under the influence of high free-carrier densities but with low doping density, where the effect of ionized impurity scattering is diminished by a combination of low ionized impurities and high screening, is unique to this research. This is the mode of transport in AlGaN/GaN HEMTs and theoretical studies of mobility under these conditions have not been previously reported in literature. These results,

for instance, enable evaluation of mobility tradeoff between the free-carrier density and the lattice temperature in the channel. The free-carrier density can be tuned by band-gap engineering of the AlGaN/GaN heterojunction and the channel temperature can be calculated as demonstrated in [96].

CHAPTER IV

ISOTHERMAL STUDY OF CHARGE TRANSPORT IN ALGAN/GAN HEMTS

The study and calibration of charge transport in AlGaN/GaN HEMTs are presented in this chapter. The chapter begins with a brief introduction to AlGaN/GaN HEMTs followed by a description of the Monte Carlo simulation pertaining to HEMTs. The results of the isothermal study of charge transport in AlGaN/GaN HEMTs are presented next along with an analysis of the results. Finally, a design solution to improve the device performance is proposed and evaluated.

4.1 AlGaN/GaN HEMTs

High electron mobility transistors (HEMTs) are field effect transistors (FETs), where a gate electrode controls a channel formed between the source and drain regions. In a simple MESFET, the drive current of the device can be increased by increasing the doping, but at the expense of degraded mobility due to increased ionized impurity scattering. To overcome this problem, a HEMT device is modulation doped, where the dopant atoms are spatially separated from the conduction channel. This is accomplished by a structure shown in Figure 4.1, where the n-type doped region in the top wide bandgap material close to the interface is depleted. The electrons donated by the dopant atoms form an accumulation layer at the top of the i-GaAs layer forming a channel with high mobility. The corresponding band diagram in Figure 4.2 shows energy barriers on either side of the channel confining electrons to the potential well, and preventing vertical motion. This forms a layer of sheet charge density know as the 2D electron gas (2DEG). The electrons in the 2DEG have a higher mobility than electrons in a n-type doped bulk material because they are spatially separated from the dopants in the barrier region virtually eliminating the effects of mobility degrading ionized impurity scattering. The longitudinal field due to the drain-source bias causes a lateral flow of these high-mobility electrons in the channel yielding high drive

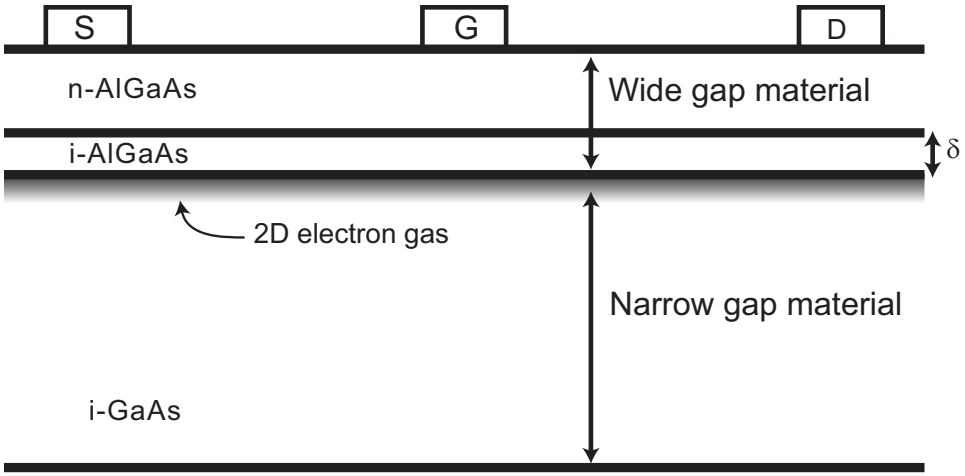

Figure 4.1: Example of modulation doping

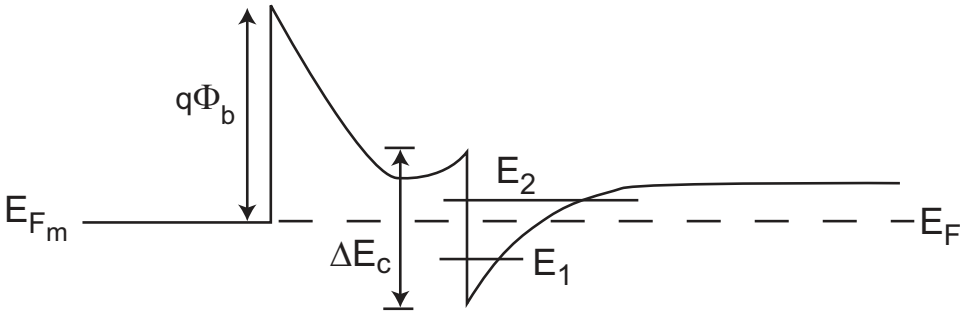

Figure 4.2: Energy band diagram of GaAs HEMT

current. These modulation-doped heterostructures have been fabricated using various material systems, and have been in production for several years.

HEMT devices based on wurtzite AlGaN/GaN heterojunction, however, have unique properties that make them attractive for high-power, high-speed applications. A schematic representation of an AlGaN/GaN HEMT is shown in Figure 4.3. They are widely used in RF power amplification, and are excellent candidates for micro- and millimeter wave devices. Their wide bandgap yields high breakdown field strength, enabling high-power operation, and the large difference in the bandgap between GaN and AlN enables very effective modulation-doped structures with high electron mobility. Another key feature of the AlGaN/GaN material system is the presence of polarization charges [21]. GaN and AlGaN are strongly polar materials, and exhibit spontaneous polarization that leads to equal and opposite sheet charge accumulation at the end faces of the crystal. However,

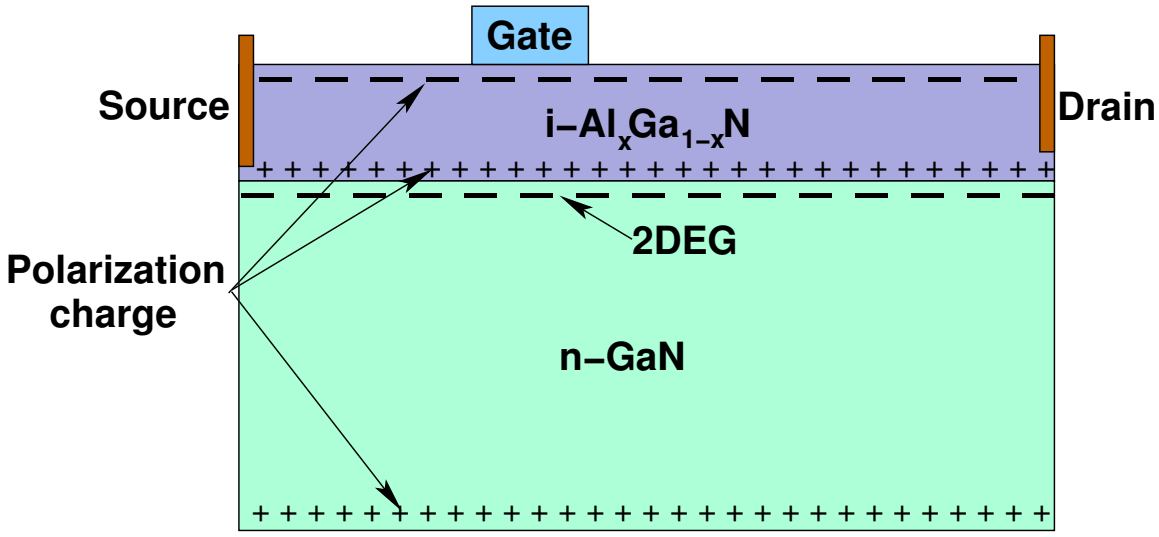

Figure 4.3: Schematic representation of AlGaN/GaN HEMT

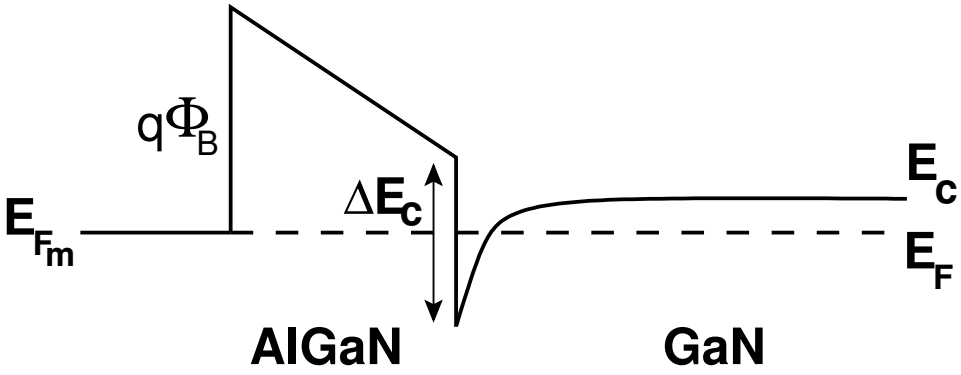

Figure 4.4: Energy band diagram of AlGaN/GaN HEMT

the difference in the magnitude of the spontaneous polarization between AlGaN and GaN results in a net polarization charge at the heterojunction interface. Furthermore, the lattice mismatch between AlGaN and GaN produces tensile strain that induces piezoelectric polarization adding to the spontaneous polarization at the interface. This results in a net positive polarization at the AlGaN/GaN interface, which is balanced by electrons in the 2DEG. The resulting net charge density is on the order of 1×10^{13} electrons/cm^2 at the interface, which is about four to five times higher than AlGaAs/GaAs HEMTs, resulting in significantly higher current drive capability. The higher bandgap of AlGaN yields a conduction band offset at the interface, which aids in confining the 2DEG by providing a potential barrier for the electrons in the channel as shown in Figure 4.4.

Due to these advantages of AlGaN/GaN HEMTs, these devices are typically operated in the high-field regime, which require detailed full bandstructure calculations to accurately model charge transport in these devices.

The development of III-nitride material systems such as AlGaN/GaN posed many challenges. The material system suffered poor crystalline quality, high n-type background concentration resulting from native defects, poor p-type doping, difficulty making Ohmic contacts, and lacked a suitably lattice matched substrate. Advances in the fabrication technology has enabled high-quality, low-defect devices using Sapphire and SiC substrates. Different growth techniques such as MOCVD and MBE have been employed to obtain high-quality single-crystal GaN films with background concentrations as low as $10^{16}/\text{cm}^3$. Electron concentration of $2\times10^{19}/\text{cm}^3$ has been achieved for Si-doped n-type GaN, and Mg-doped p-type GaN with hole concentrations of $3 \times 10^{18}/\text{cm}^3$ has also been demonstrated. When compared against SiC, which is a competing wide bandgap semiconductor with demonstrated n- and p-type doping and excellent high-power performance, III-nitride devices form direct bandgap heterostructures, have better Ohmic contacts, and in the case of GaN, has an electron saturation velocity of $3 \times 10^7\text{cm/s}$. A good review of AlGaN/GaN HEMT development, device operation and applications are presented in [23].

Several groups have been working on different aspects of the development of AlGaN/GaN HEMTs. Notable contributions include Mishra (UCSD), Morkoc (VCU, UIUC), Shur (RPI), Palacios (MIT), Eastman (Cornell). The key areas of development are the growth process for better material quality, suitable substrates, p- and n-type doping, good Schottky and Ohmic contacts, sub-micron gate, reduced gate leakage, recessed gate [107] to improve RF power, use of source/gate field plates, improved power added efficiency, and flip-chip bonding. Contemporary devices are capable of producing about 10W/mm of output power, which is one-order of magnitude improvement over conventional HEMTs [23].

AlGaN/GaN HEMTs have also been commercially available, and have been evolving with the continuous introduction of higher performance devices. Some of the leading commercial vendors are Nitronex (Si substrate), Cree (SiC substrate), Fujitsu, and Toshiba.

Devices capable of delivering 100W at RF are commercially available.

4.2 Monte Carlo Simulation of GaN-based HEMTs

A full band Monte Carlo device simulation of a complete AlGaN/GaN HEMT presents several challenges. The Brillouin zone (BZ) of wurtzite GaN has several important valleys that play a significant role in high-field transport. Due to the symmetry of the wurtzite crystal, the BZ can be reduced to an irreducible wedge containing only $1/24^{th}$ of the BZ, and the rest of the BZ can be constructed by symmetry operations. Only the energy-wavevector relation within the irreducible wedge needs to be represented, but with sufficient resolution to accurately capture transport phenomena. The presence of several significant scattering mechanisms combined with a large number of *k*-states in the BZ makes simulation of particle trajectory in the *k*-space computationally expensive. Likewise, the need for a well refined real space mesh due to the high-field strengths in the channel, combined with relatively long channel lengths, yields a real space grid with a large number of elements. The high electron density in the channel and the high-field strengths generated by the strong polarization charges necessitates a large ensemble of simulation particles to ensure stable self-consistent solution of the Poisson equation. Due to these constraints, the implementation of the Monte Carlo algorithm needs to be computationally efficient to be able to perform useful device simulations in a reasonable amount of time. Trade offs such as performance vs. accuracy, CPU vs. memory, etc. are often required for the simulation of realistic devices. Computational techniques such as the pre-tabulation of scattering rates are often used to improve simulation performance.

The Arizona State University group has modeled transport in GaN using a full band *cellular* Monte Carlo (MC) method, which uses the cellular automata (CA) approach. The CA simulation method offers physical content comparable to traditional MC, but is significantly faster and has the potential to take advantage of parallel processing. In the CA approach the *k*-space is discretized into a finite number of cells each representing a state in the momentum space. Scattering rates are computed between cells, and the total rate for all mechanisms combined is stored in a scattering rate table requiring a rather large

N_k^2 entries, where N_k is the number of cells in the BZ. Information about the exact type of scattering process involved is lost [35], as only the total rate between cells is stored. This makes it impossible to refine the k-vector within the final cell, and the center of the final cell is typically chosen as the final state leading to inexact energy conservation. Final state selection and energy conservation can be improved by increasing the number of cells to achieve finer resolution in the k-space, and by using separate scattering tables for each mechanism, both of which prohibitively increase the memory requirements.

Saraniti *et al.* attacked this problem in 2 ways. By analyzing the trade offs between the accuracy of final state energy, and the memory required for the k-space mesh, a non-uniform grid in the k-space was introduced. A coarse grid requires a relatively smaller scattering table, and the coarseness of the grid was determined by considering physical features of the bandstructure such as the density of states. For example, a very fine grid is required around the highly populated, low energy minima of the Γ valley of the first conduction band in GaN. Secondly, to improve energy resolution and reduce memory requirements, a hybrid MC/CA approach was adopted. The more accurate MC scattering tables were used in high-energy regions of BZ, where the particle population is reduced, and in regions where the scattering rates were lower, whereas the CA tables were used everywhere else. The idea was that the selective use of computationally more expensive MC algorithm in regions of low particle population and in regions of low scattering probabilities would not significantly degrade the overall performance of the simulation.

However, the problem of generating a non-uniform grid is non-trivial. Firstly, the non-uniform grid introduces energy discretization error that is not constant over the entire BZ. Secondly, the process of generating the grid is long and computationally expensive. Algorithms such as a recursive branch-on-need bisection produce excellent grids with respect to energy conservation and symmetry, but are completely unsuitable for tracking particles along their Newtonian trajectories. There are no robust algorithms to *efficiently* follow a particle from one cell to another, when the number of neighbors at each cell side is arbitrary [34]. Additional constraints were introduced such that the cells may be non-uniformly spaced, but the cell size had to be an integer multiple of the spacing of a

finer mesh. In addition, the MC scattering selection algorithm required the inversion of the energy-momentum relation for final state selection. To find all the cells intersecting a isoenergy surface, a recursive 3-D binary search tree was added to the table structure. These solutions to the challenges associated with the CA and MC/CA hybrid approaches introduce additional complexity and overhead, and cuts into the computational advantage of the CA approach, while requiring large amounts of memory. The memory requirements for a full bandstructure including 10 conduction bands and 8 valence bands of GaN, for example, would require several gigabytes of memory to hold the entire scattering table.

For the simulation of full band AlGaN/GaN HEMTs, Yamakawa *et al.* [108] have included *ab initio* calculations of phonon dispersion in GaN and have accounted for the non-equilibrium LO phonon distribution based on phonon lifetime. These are sufficient for the simulation of transport under isothermal conditions.

4.3 Simulation of AlGaN/GaN HEMTs

Simulations of AlGaN/GaN HEMTs were performed to obtain drain current vs. source-drain bias characteristics. Simulation of a full device presented several challenges, which required careful selection of the simulation parameters such as time steps, particle weights, initial conditions, etc. The simulations were performed using an ensemble of particles, and the Poisson equation was solved synchronously to obtain self-consistent solution to the BTE. The steady-state distribution of electrons density was estimated, and the device was pre-populated with electrons to approximately match steady-state conditions. Poor initial conditions result in simulations that take very long to converge, and the transients skew the estimators. The initial conditions were fine tuned both by trial and error, and information from completed simulations.

Initial self-consistent simulations failed to reach steady-state, and estimators of the transport quantities indicated the presence of plasma oscillations. The time step for synchronization with the Poisson solver was then calculated based on [82]. Careful choice of the synchronization time step and grid refinement were required to eliminate plasma oscillations. An oxide layer was added to the top of the device to provide a path for the

flux lines originating from the polarization charges applied at the top of the AlGaN layer. This was required to obtain correct solution to the Poisson equation.

The terminal currents were estimated by applying the Ramo-Shockley theorem [86]. Test functions for the current estimator were assigned to each of the contacts. The simulator reports instantaneous current at regular time intervals. The source and drain contacts were modeled as Ohmic contacts, implemented with Ohmic buffer regions. The gate contact was modeled as a Schottky contact with a Ni/Au metal stack.

4.3.1 Isothermal Simulation of AlGaN/GaN HEMTs

In high-power applications where the devices are operated under steady-state bias conditions, strong self-heating effects severely degrade electron mobility, resulting in a thermal droop in the drain current with increasing bias [109, 110]. Several groups have reported upon theoretical investigations of charge transport in GaN-based HEMTs using Monte Carlo simulation [108, 111, 112]. These studies have focused on either isothermal transport at field strengths below 500kV/cm or electrothermal transport at high-field strengths. Self-heating, however, is not as severe for narrow pulse operation at low duty cycle as it is in the steady-state, even under conditions of high bias, due to the lower average rate of energy transfer from the electron system to the crystal lattice. Low duty cycle applications include high-power pulsed X-band radars [113], ground penetrating radar (GPR) [114], and ultra wide band (UWB) communications [115, 116]. GaN-based HEMTs are suited for these applications as high large biases may be applied without inducing breakdown.

Isothermal simulations, corresponding to low duty cycle (< 1%) narrow pulse operation of GaN-based HEMTs, were performed. Figure 4.5 shows the simulated drain current for V_{gs} ranging from -3V to +2V and V_{ds} up to 25V. The simulations were performed for the case of a 300K ambient temperature. Under high gate bias, the I-V curves in Figure 4.5 indicate a droop in the drain current with increasing V_{ds}. Drain current droop in GaN HEMT pulsed I-V measurements has been previously reported [117]. The cause of current droop in the absence of self-heating was investigated through the analysis of transport quantities in the channel.

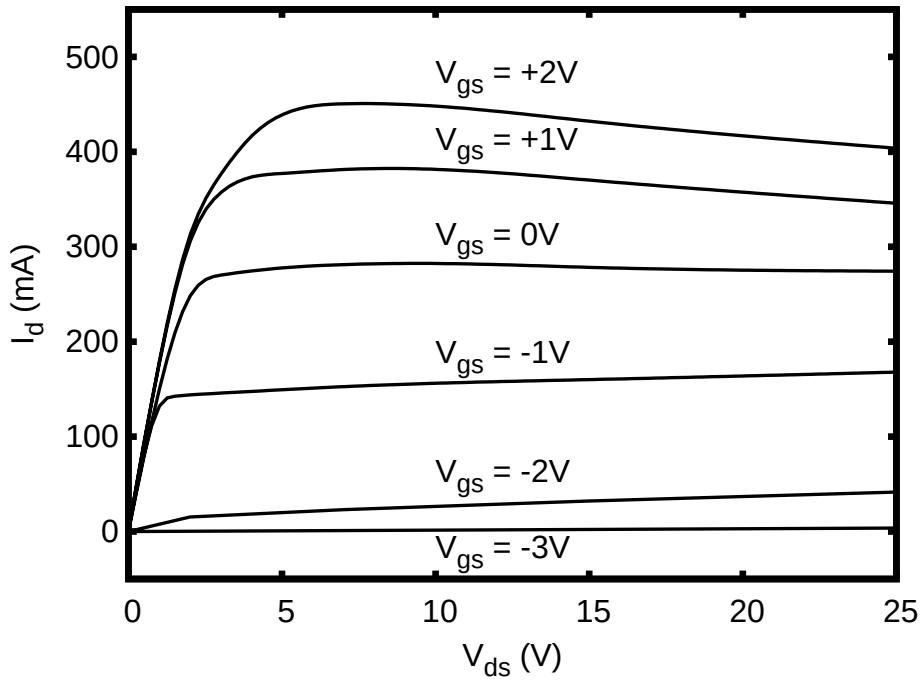

Figure 4.5: Isothermal simulations show a drop in drain current at higher drain and gate bias.

A plot of the longitudinal components of the electron velocity and electric field strength along the channel is shown in Figure 4.6 for V_{gs} = 2V and V_{ds} = 7V and 25V. In the channel region below the gate contact, electrons experience a significant increase in longitudinal electric field strength, and are accelerated to higher energies in the Γ_1 valley where the group velocity is large (point A in Figure 4.7). Upon exiting the gate region, the electrons encounter a *field spike* – a consequence of field crowding at the drain edge of the gate electrode characterized by a sharp increase in the lateral electric field – across which a large fraction of V_{ds} is dropped. This field accelerates the electrons further up the Γ_1 valley as they gain energy and velocity. The large vertical field due to the polarization charges at the AlGaN/GaN interface also accelerates electrons upwards in energy along the $\Gamma - A$ -axis in k-space. Above approximately 7V V_{ds} and 2V V_{gs}, an appreciable number of electrons gain sufficient energy for transfer out of the Γ_1 valley, through a deformation potential scattering. With increasing drain bias, a larger fraction of electrons is transferred to the L, M, and A valleys, where electron group velocity is lower. As a direct consequence,

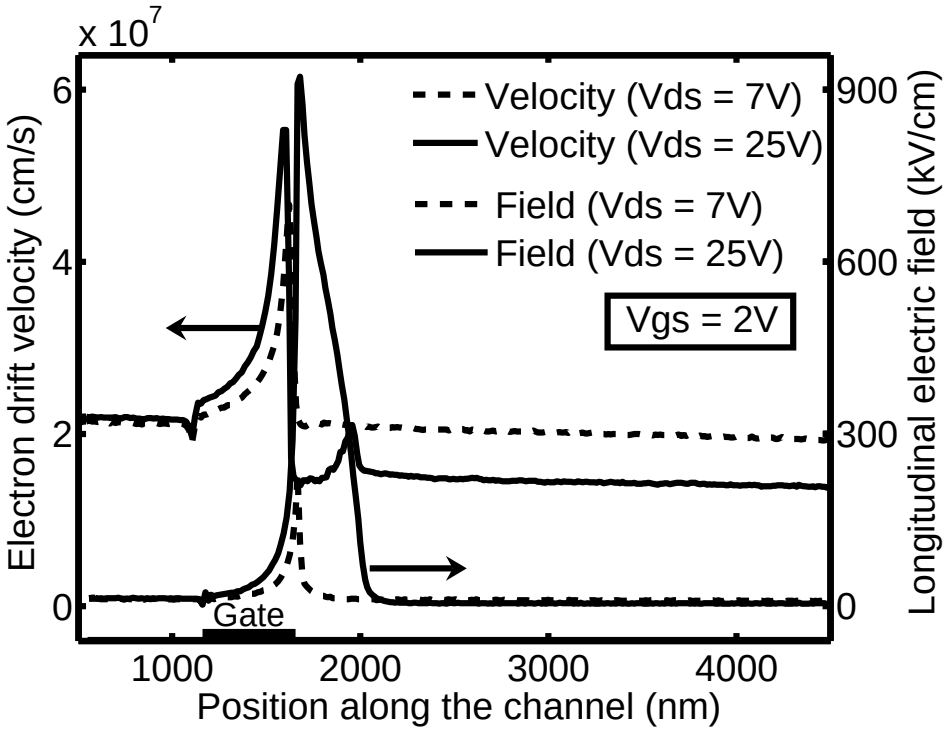

Figure 4.6: The field spike at the drain end of the gate for Vds = 25V significantly increases the electron energy and transfers them to the satellite valleys where the electron group velocity is lower.

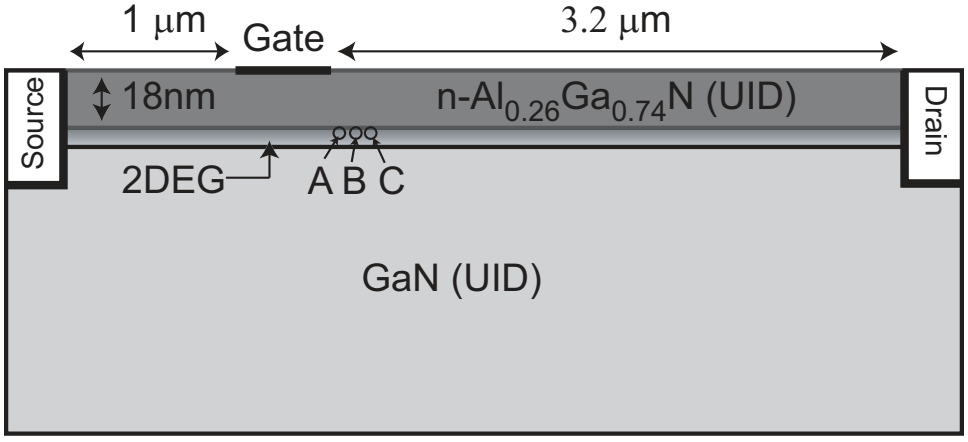

Figure 4.7: Schematic structure of the simulated $Al_{0.26}Ga_{0.74}N$/GaN HEMT highlighting channel points of interest A, B & C

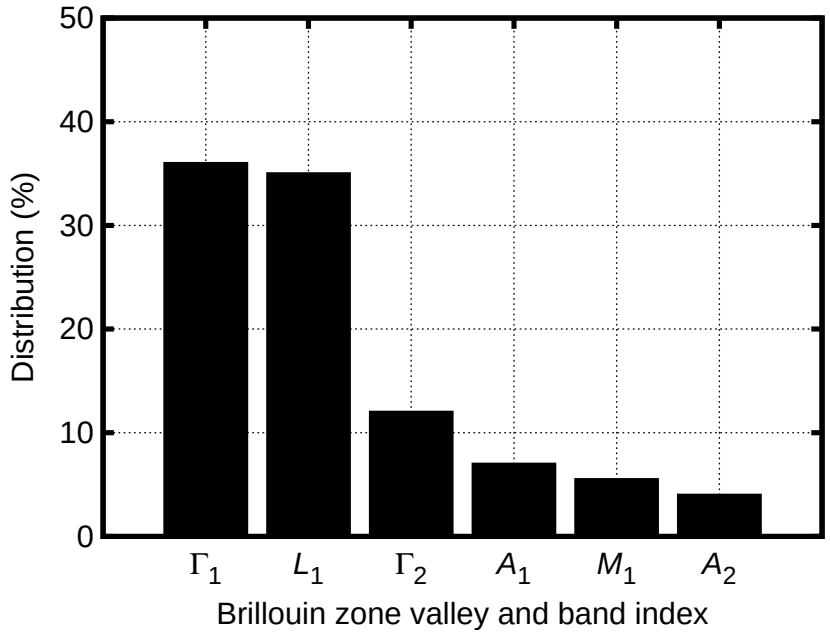

Figure 4.8: Distribution of particles at point B shifts significantly to L_1, Γ_2, A_1 and M_1 valleys.

a drop in average electron velocity is observed at point B in the device, as indicated in Figure 4.6. To confirm this, the *k*-space distribution of electrons within the Brillouin zone was calculated at locations within the device channel marked A, B & C in Figure 4.7. For V_{ds} = 25V it was found that while the particles were predominantly (> 99.5%) in the Γ_1 valley at point A, the distribution at point B shifted significantly to the L_1 (≈ 35%), Γ_2 (≈ 12%), A_1 (≈ 7%), M_1 (≈ 5.5%) and A_2 (≈ 4%) valleys, while the occupation of the Γ_1 valley was reduced to (≈ 36%), as shown in Figure 4.8.

The double peak in the velocity profile of Figure 4.6 for the case of 25V drain bias is, in fact, the fingerprint of intervalley transfer first out of and then back into the Γ_1 valley. Increasing V_{ds} to 25V also broadens the high-field region, delaying velocity and energy relaxation (see Figure 4.6). Although the peak electron velocity is larger at higher drain bias than at lower drain bias, it is important to recognize that this velocity overshoot only occurs in a narrow region of the channel. Of greater significance is that with increasing drain bias, a larger fraction of the applied bias V_{ds} is dropped across this field spike, lowering the average field in the pinched off region of the channel. This is directly attributable to

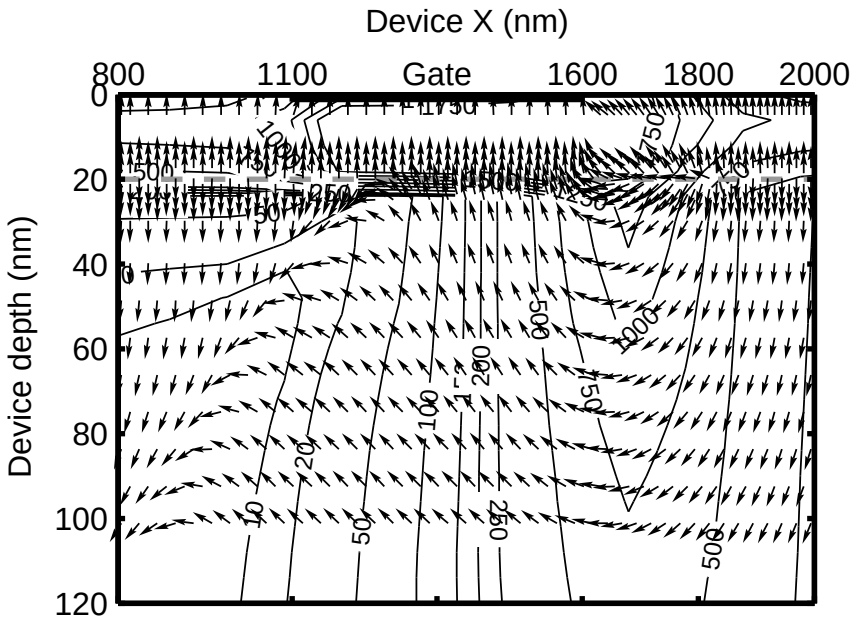

Figure 4.9: Vector plot of field profile below the gate contact shows a -2V gate bias inverting the vertical component of the field over a significant portion of the channel under the gate. Contour plot shows magnitude of field (kV/cm).

intervalley transfer, which causes a disproportionate increase in the differential electrical resistance within the region of the field spike with increasing drain bias, as the average electron group velocity in the satellite valleys is lower than that of the Γ_1 valley. This phenomenon cannot be understood in the context of bulk velocity-field profiles (such as in Figure 3.3) since charge transport in the region of the field spike is nearly ballistic. Because the average field strength in the pinched off region of the channel beyond the field spike is below approximately 10 kV/cm, the lower average field at higher drain biases leads directly to a reduction in average electron velocity (see Figure 3.3), and hence to drain-source current as well. It is emphasized that the explanation provided above for the droop in drain current shown in Figure 4.5 - equivalent to short pulse measurements performed at low duty cycle - involves basic principles of isothermal charge transport, and is independent of both Joule heating and parasitic series resistance.

At a low gate bias of -2V and V_{ds} = 25V, the negative bias on the gate overcomes the polarization sheet charge and inverts the vertical component of the field in the channel starting from the drain end of the gate and extending towards the source end of the gate

with decreasing gate biases as shown in Figure 4.9. This moves electrons away from the interface, depleting a significant portion of the channel under the gate. The electron current propagates around the field spike without transferring to the satellite valleys. The field spike remains narrow, and a constant fraction of V_{ds} is dropped in the high-field region. The average lateral field strength in the pinched-off region remains proportional to the drain bias, explaining the absence of drain current droop at low gate bias.

To study ways to minimize or eliminate the droop, transport in different directions within the basal plane were simulated by rotating the channel orientation from $\Gamma \rightarrow M$ to $\Gamma \rightarrow K$ in 3 steps. No noticeable change in the I-V characteristics were observed, and the I-V characteristics are identical to the one shown in Figure 4.5 for $\Gamma \rightarrow M$. It is concluded that the droop in drain current is independent of the channel orientation within the basal plane, and is attributed largely to the nearly isotropic electronic dispersion perpendicular to the growth axis, within the Γ valley of the first conduction band. A similar trend has previously been reported for electron velocity in bulk material [100]. Furthermore, the M, K, and H valleys were found to be least occupied, and do not play a significant role in device operation over the range of biases considered here, making the channel orientation within the basal plane less important.

The efficacy of source field plates (SFPs) and gate field plates (GFPs) to reduce or eliminate drain current droop was also investigated. The objective was to reduce the field crowding effect at the drain end of the gate contact, and thereby reduce the magnitude of the field spike responsible for the drain current droop. Figure 4.10 depicts cross sections of devices for which the source and gate field plate arrangements completely eliminate current droop. The optimal field plate geometry and placement for both the SFP and GFP designs were determined based on a thorough search through a design subspace. Isothermal I-V characteristics for both solutions are shown in Figure 4.11, up to a gate bias of +2V. Higher gate biases are of less practical interest, as the Schottky gate contact eventually becomes forward biased, resulting in a large leakage current.

The field plates effectively suppress the magnitude of the field spike by introducing an additional "soft" peak as shown in Figure 4.12, while distributing the potential drop over

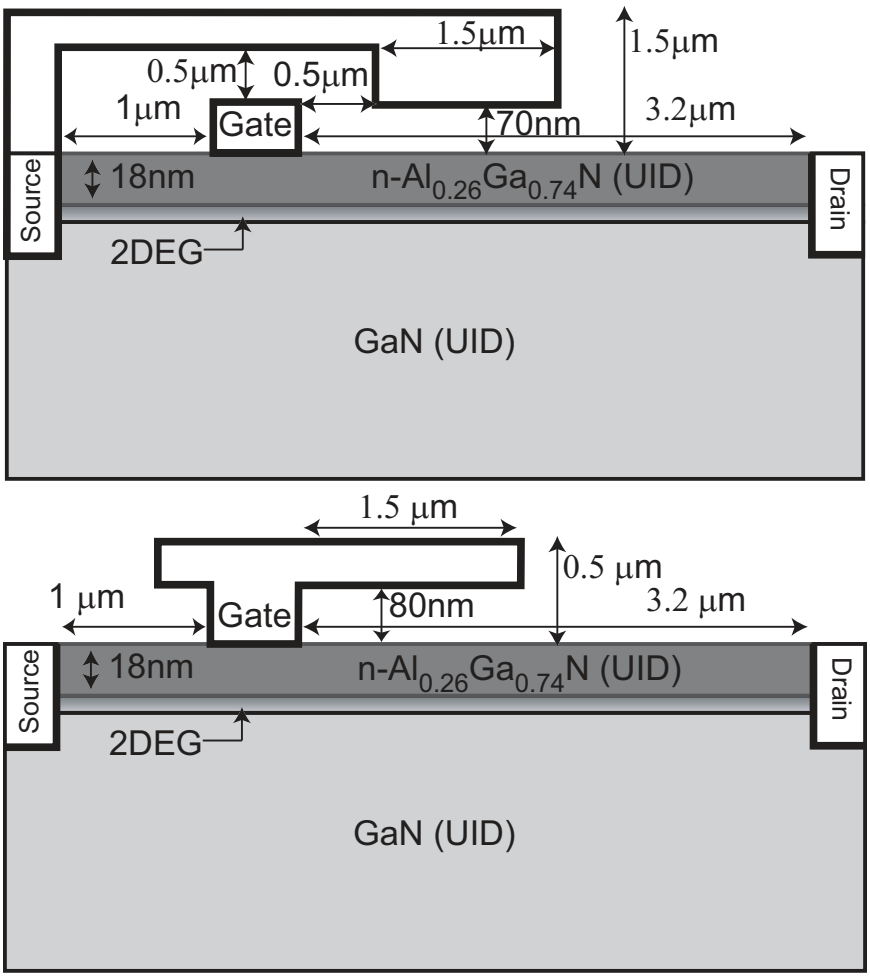

Figure 4.10: Schematic of the device with source and gate field plates that were used to eliminate the droop in the isothermal drain-source current.

a larger fraction of the channel between the gate and the drain contacts. The position of second field peak corresponds to the drain end of the field plate, and is not as sharply peaked as the field spike below the drain end of the gate contact due to the increased vertical separation of the field plate from the channel. Increasing the vertical separation between the channel and gate contact would also reduce the magnitude of the original field spike, but that would adversely affect the transconductance and the cutoff voltage of the device. The present arrangement of the field plates does not reduce the gate contact's electrostatic control over the channel, as evidenced by the simulated I-V characteristics (Figure 4.11) which show no change in the cutoff voltage and, in fact, a slightly enhanced transconductance. By eliminating the droop, the drain current increases by 16% at V_{gs} =

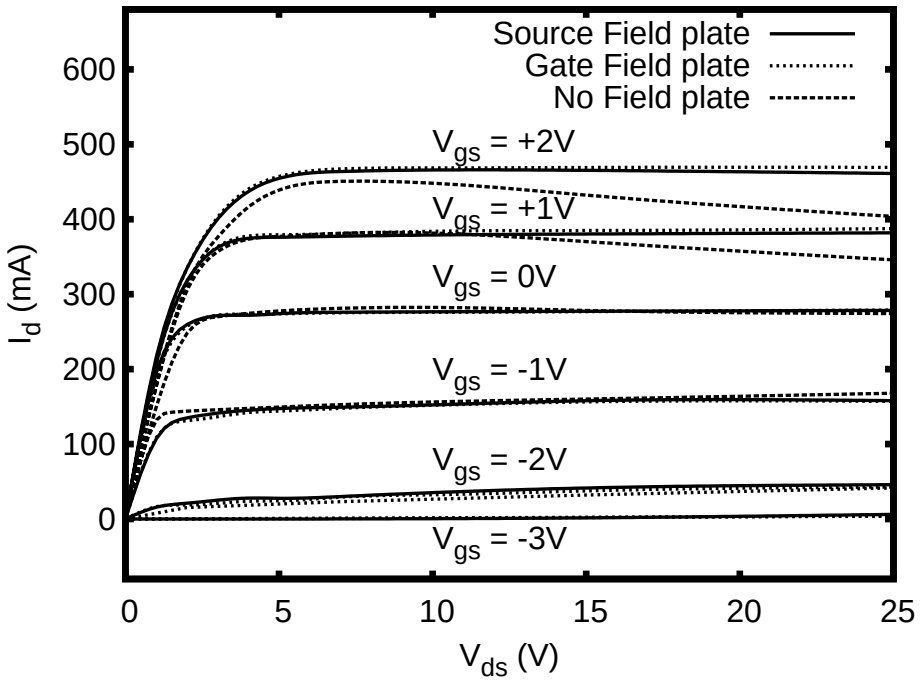

Figure 4.11: Using field plates, the droop in the isothermal drain-source current have been eliminated.

+2V and V_{ds} = 25V. The presence of the second peak in the lateral component of the electric field in the channel prevents the large drop in electron drift velocity after the initial overshoot, and further accelerates the electrons to higher velocities over the rest of the channel all the way up to the drain contact. A comparison of the electron velocity profiles for the cases with and without the field plates is shown in Figure 4.13. It is this increase in average electron velocity due to the introduction of a field plate which leads directly to an increase in the drain-source current.

Since both SFP and GFP were effective in eliminating the drain current droop, their effect on the gate capacitance becomes the primary concern for X-band applications. The use of a source field plate increases C_{gs}, but due to the large separation of the field plate from the gate contact, and the absence of the Miller effect, the increase in C_{gs} is minimal. The use of a gate field plate, however, leads to a large increase in C_{gd} due to 1) the large addition to the gate contact metallization, 2) a significantly reduced separation from the drain contact, and 3) the difference amplified by the Miller effect. The superiority of SFP over GFP for

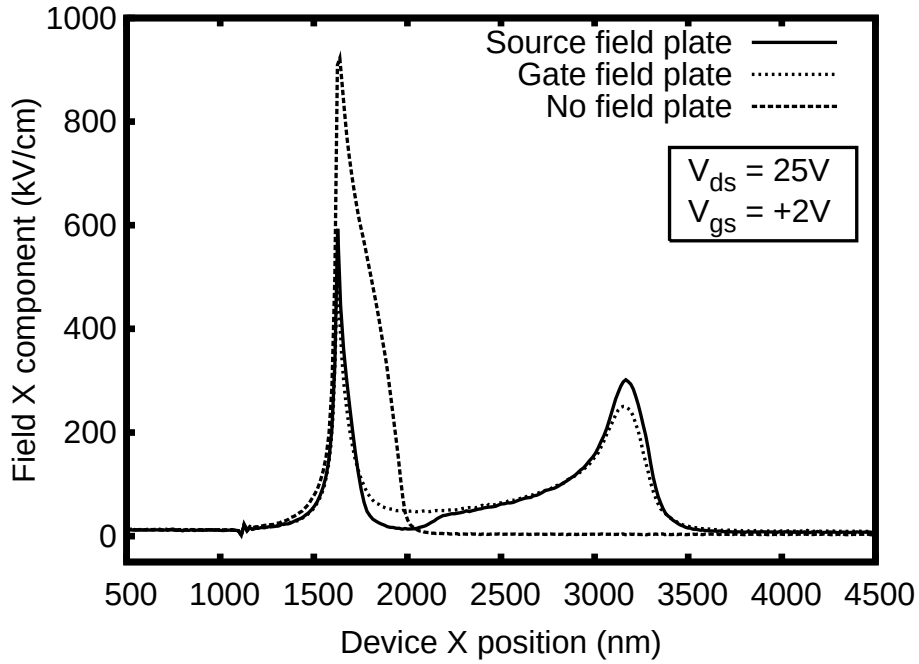

Figure 4.12: The field plates reduce the magnitude of the original field spike by introducing an additional "soft" peak.

power-added efficiency (PAE) and large-signal gain at 4GHz has been demonstrated in [25]. Hence, it is concluded that the use of a well designed source field plate is the best solution to eliminate isothermal drain current droop in high-performance AlGaN/GaN HEMTs.

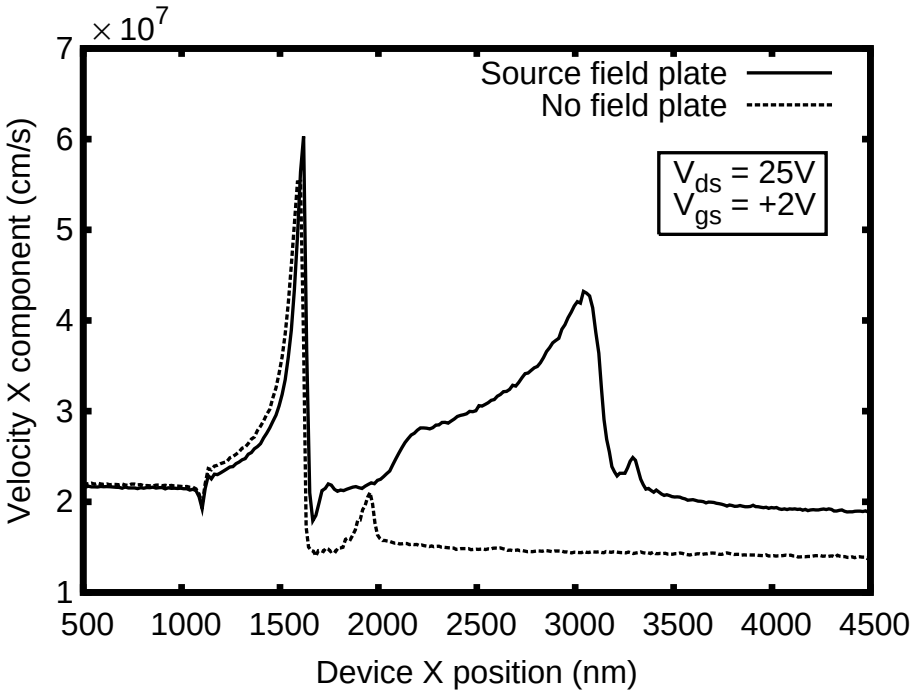

Figure 4.13: The electron drift velocity is significantly improved by the use of the field plate leading directly to an increase in the isothermal drain-source current.

CHAPTER V

ELECTROTHERMAL STUDY OF CHARGE TRANSPORT IN ALGAN/GAN HEMTS

In this chapter an electrothermal study of charge transport in AlGaN/GaN HEMTs is presented. The chapter begins with a review of the electrothermal transport in AlGaN/GaN HEMTs followed by a description of the Monte Carlo method used to simulate it. The results of the electrothermal study of short and long channel HEMTs are presented next.

5.1 Review of Electrothermal Transport in AlGaN/GaN HEMTs

Unlike pulsed mode operation, high-power steady-state operation of GaN-based HEMTs is severely limited by self-heating effects [28]. Applications include micro- and millimeter-wave power amplification [1, 26] and power switching [118], where performance is limited by parasitic thermal effects.

In order to realize the full potential of these materials a deep understanding of the *coupled* electrical and thermal transport is essential. In a typical AlGaN/GaN HEMT electrons gain energy while being accelerated by the electric field in the device, which are calculated self-consistently by solving the Poisson equation at small time steps. These hot electrons lose energy predominantly through the emission of LO phonons, which, due to the relatively long LO mode lifetime decay relatively slowly leading to an increase in the local non-equilibrium LO phonon population. This in turn may lead to a reduction of electron mobility through enhanced stimulated emission and absorption.

The LO phonons decay by directly or indirectly transferring energy to acoustic mode phonons, which then transport thermal energy away from the active region of the device to the substrate. The phonon population is calculated by a system of rate equations and the thermal transport via acoustic modes is treated in the diffusive limit through a two-dimensional lattice heat equation.

An ensemble Monte Carlo simulation with self-consistent electrical and thermal transport models provides good insight into the device operation [119] under various conditions such as applied bias and device geometry. Electrothermal study of AlGaN/GaN devices have been reported by a few authors. Sadi *et al.* [110] have performed self-consistent electrothermal Monte Carlo simulation of AlGaN/GaN HEMTs using a 5-valley bandstructure model of Albrecht, Wang, Brennan [33]. They have used a heat diffusion equation (HDE) solver to translate the power density distribution into a spatially varying temperature distribution by means of an analytical thermal resistance matrix method developed in [120]. They also used an equilibrium optical phonon population assuming that the increase in the optical phonon population in a limited region of k-space will cause an increase in both phonon absorption and emission rates and hence little change in the net rate of phonon generation. However, the use of partial bandstructure limits their ability to model high-field transport, where the equilibrium phonon population approximation also breaks down. Sadi *et al.* have continued to use the partial bandstructure and equilibrium phonon population even in their later work [112, 121, 122], where they consider short channel GaN HFETs. Yamakawa *et al.* [108] have considered the full bandstructure and non-equilibrium phonon population but limit their analysis to 300K.

5.2 Monte Carlo Simulation of Electrothermal Transport in AlGaN/GaN HEMTs

In this section, an electrothermal study of high-power HEMTs using the charge transport model detailed in chapter 2 is presented. An AlGaN/GaN HEMT with a fixed geometry is considered and the spatial dependence of non-equilibrium phonon population with applied bias and its influence on the terminal current are analyzed. The I/V characteristics with and without thermal feedback is also compared to study the impact of elevated non-equilibrium phonon population in the channel.

Thermal transport was simulated on a grid constructed as a non-uniform extension of the electrical grid due to the different length scales for electrical and thermal transport. The LO phonon mode was approximated as dispersionless, the spatial dependence of its

occupation number was solved using the system of rate equations.

$$\frac{dN_q^s}{dt} = \frac{-(N_q^s - N_{eq}^s)}{\tau_s} + G_e^s$$

where N_q^s is the non-equilibrium phonon population, N_{eq}^s is the equilibrium phonon population, τ_s is the phonon lifetime, G_e^s is the net phonon emission rate, and s is the phonon mode.

Thermal transport via acoustic modes was treated in the diffusive limit, through a two-dimensional lattice heat equation.

$$\nabla \cdot \kappa(x, y) \nabla T(x, y) = s(x, y)$$

where T is the acoustic mode temperature, s is the net power transferred per unit volume from optical phonons to acoustic phonons, and κ is the thermal conductivity tensor.

Several individual isothermal simulations were initially performed for different bias conditions to calibrate adjustable deformation potential constants to reproduce drain current measurements extracted at low (< 1%) duty cycle as detailed in the previous chapter. The drain-source bias was swept from 1V to 40V, while the gate-source bias was varied from 2V to 5V. Detailed energy balance was verified by comparing the net energy loss rate to phonons with the net energy gain rate due to the applied field ($\vec{J} \cdot \vec{E}$).

The Monte Carlo simulations indicate that at low drain-source bias (V_{ds} = 5V), the lateral electric field in the channel is, in general, very small (< 5kV/cm) across most of the channel, with the exception of a spike due to field crowding under the drain end of the gate electrode, as illustrated in Figure 5.1.

Upon encountering the field spike, channel electrons experience an abrupt rise in their rate of energy gain, and consequently exhibit a localized transient overshoot in both velocity and energy. These hot electrons transfer their energy to the crystal predominantly through the emission of LO phonons, leading to a local increase in the non-equilibrium LO mode population (see Figure 5.2), and a local "hot spot" in the acoustic mode temperature.

Channel electrons achieve their peak transient velocity at the drain end of the gate, where the lateral electric field is highest, resulting in nearly ballistic transport over a short

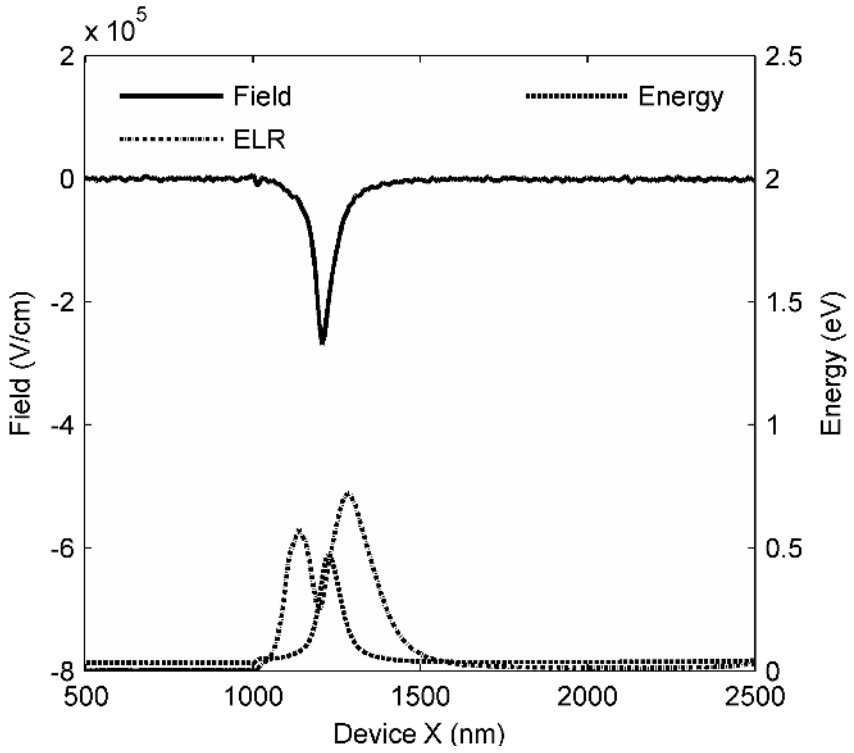

Figure 5.1: Plot of electric field, average energy, and energy loss rate (arbitrary units) profiles along the channel for the device under low drain-source bias (V_{ds} = 5V).

distance before scattering processes relax the electron "overshoot velocity" back to its steady-state, saturated value.

Under steady-state conditions, the requirement for current continuity dictates a drop in local electron density at a position corresponding to the peak transient velocity overshoot. The combined effect of the nearly ballistic transport and the decrease in electron density result in a decrease in the local energy loss rate. Immediately after the high field region, the electron drift velocity relaxes to its steady-state value as electrons approach the drain contact. At this low bias, the occupation numbers of acoustic and optic phonons are not sufficiently elevated to influence terminal current in a significant way.

At high drain-source bias (V_{ds} = 40V), there is little change in the channel region between the source and gate contacts. The gate to drain region, however, has a peak lateral electric field that is much higher than in the low bias case, as shown in Figure 5.3. Although the peak lateral electric field occurs in the channel region under the gate, the high field region is no longer confined to this part of the channel, but rather extends all

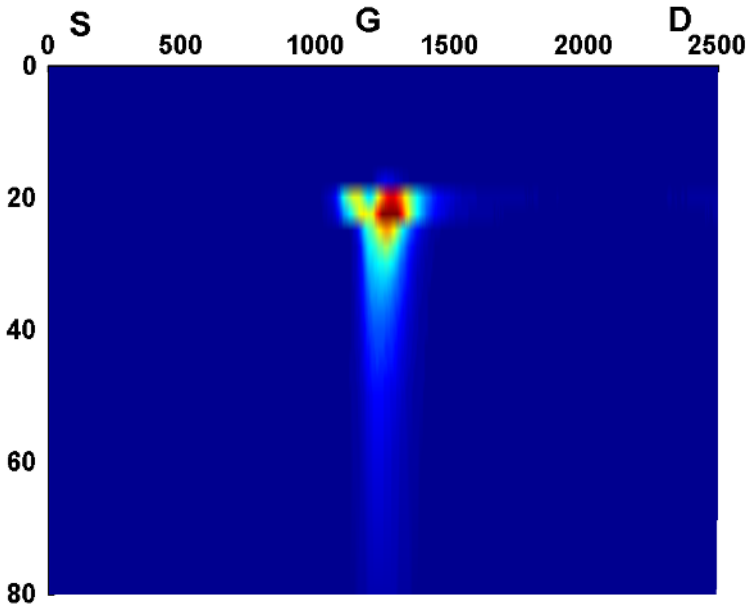

Figure 5.2: Spatial distribution of the non-equilibrium LO mode phonon occupation number for the device under low drain-source bias (V_{ds} = 5V).

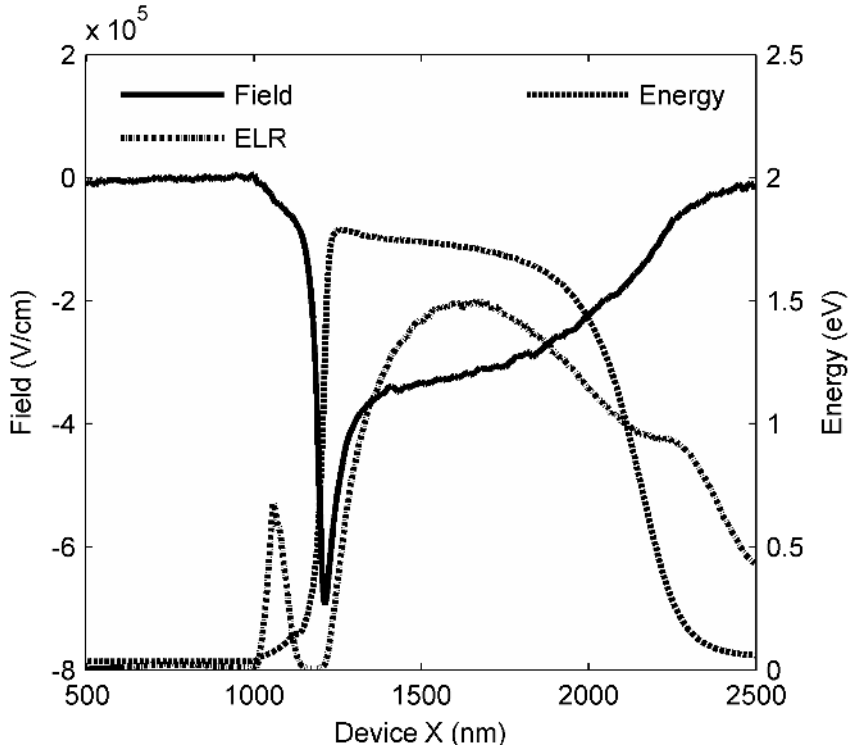

Figure 5.3: Plot of electric field, average energy, and energy loss rate (arbitrary units) profiles along the channel for the device under high drain-source bias (V_{ds} = 40V).

the way to the drain, and the device operates in saturation. The field strength in this region remains relatively high (between 200kV/cm and 400kV/cm), resulting in an increase in the average electron energy, and consequently an elevated rate of energy loss to lattice vibrations; a perceptible non-equilibrium LO phonon population extends throughout the channel between the gate and drain contacts, as shown in Figure 5.4.

Enhanced emission of LO phonons, however, results in an elevation of only a few percent in the LO phonon occupation number. LO mode phonons decay and transfer their energy to acoustic modes, resulting in an elevated acoustic mode temperature in the channel, and ultimately a degradation of channel mobility. At a 40V drain-source bias, the lattice heat equation is solved for the acoustic mode temperature on an extended thermal grid with the substrate acting as the sole thermode, which is held at 300K. The simulations indicate a peak acoustic mode phonon temperature of 420K in the gate-drain region of the channel as shown in Figure 5.5 at a position slightly displaced from the site of the localized hot spot at lower bias. Contrary to previous suggestions [28], the simulations indicate that it is the elevated acoustic mode temperature, rather than the direct influence of a non-equilibrium LO phonon population, which exerts the greater influence on the degradation of channel electron mobility over a broad range of applied bias.

5.3 Electrothermal Transport in long channel AlGaN/GaN HEMTs

In this section, an electrothermal study of transport in a long channel AlGaN/GaN HEMT is presented. A 4.2 micron device was considered and simulations were performed with the same calibrated setup detailed in the previous section. The device was studied at three applied biases of V_{ds} = 5V, 10V, and 25V representing low-, medium-, and high-bias conditions, respectively. The gate electrode was maintained at 2V. The results are presented in Figures 5.6 - 5.11. At low drain-source bias the lateral electric field in the channel is small across most of the channel as in the short channel case. The field spike at the drain end of the gate electrode is also small resulting in only a small elevation in the local non-equilibrium LO phonon population as shown in Figure 5.6. The corresponding field profile, average electron energy, and the energy loss rate (ELR) are presented in Figure 5.7.

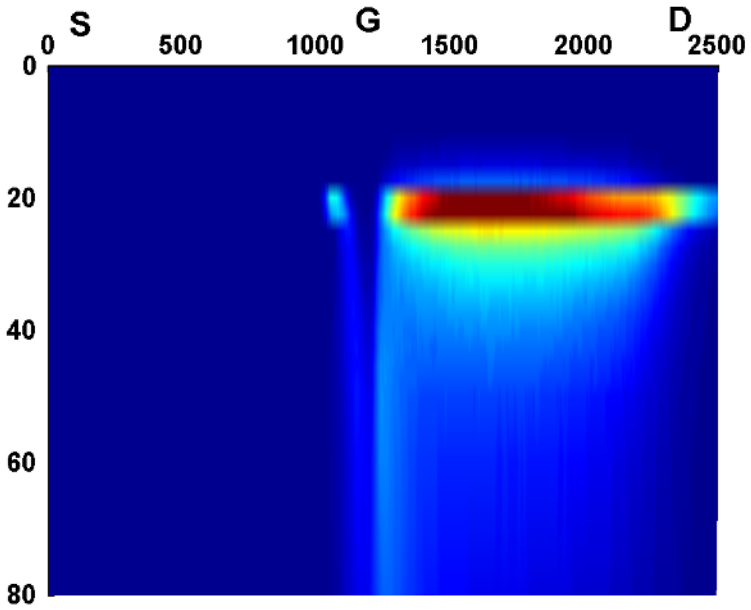

Figure 5.4: Spatial distribution of the non-equilibrium LO mode phonon occupation number for the device under high drain-source bias (V_{ds} = 40V).

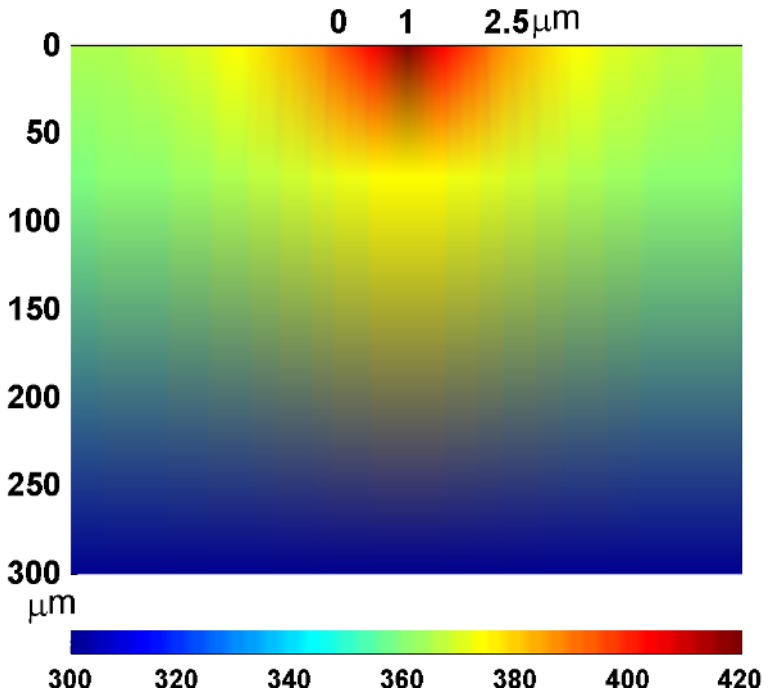

Figure 5.5: Plot of the acoustic phonon temperature on an extended grid under high drain-source bias.

At the medium drain-source bias of 10V, the field spike in the channel is more pronounced resulting in a transient overshot of both velocity and energy of the channel electrons. The effect remains local and results in a localized elevation of the non-equilibrium LO phonon population, which rapidly decay into the acoustic mode phonons [ref]. Increasing the bias to 25V results in a much higher peak of the field spike and significantly increases the local electron energy. The average electron energy at this point in the channel is about 2eV which is sufficient to transfer them to the satellite valleys where the electron group velocity is lower. This is similar to the isothermal case described in chapter 4 except for the additional influence of non-equilibrium phonon population. The drop in electron group velocity results in a local increase in the electron density and a subsequent widening of the field spike. However, unlike the short channel case, the high field region does not extent all the way to drain contact. Consequently, the increased electron energy and the elevated non-equilibrium phonon population remain local. Increasing the applied bias further results in self-sustaining millimeter-wave oscillations due to traveling dipole domains. A study of traveling dipole domains is presented in chapter 8.

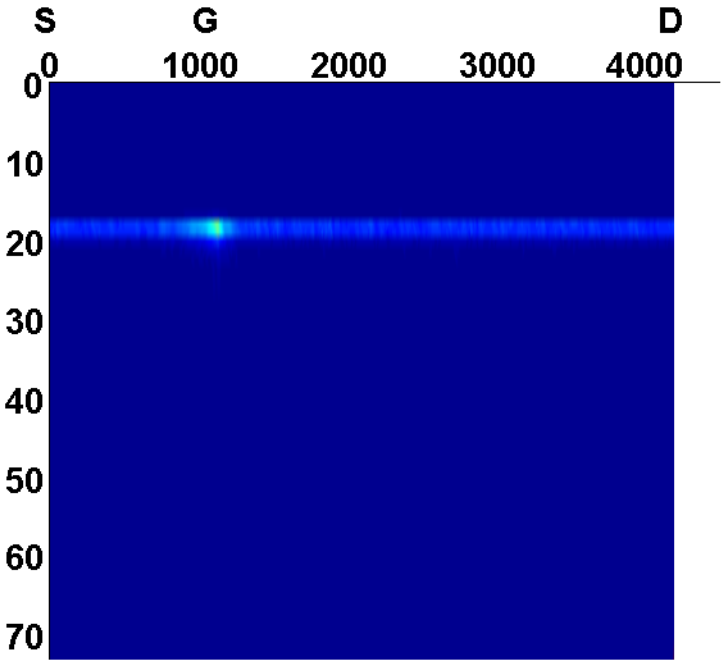

Figure 5.6: Spatial distribution of the non-equilibrium LO mode phonon occupation number for the long channel device under low drain-source bias (V_{ds} = 5V).

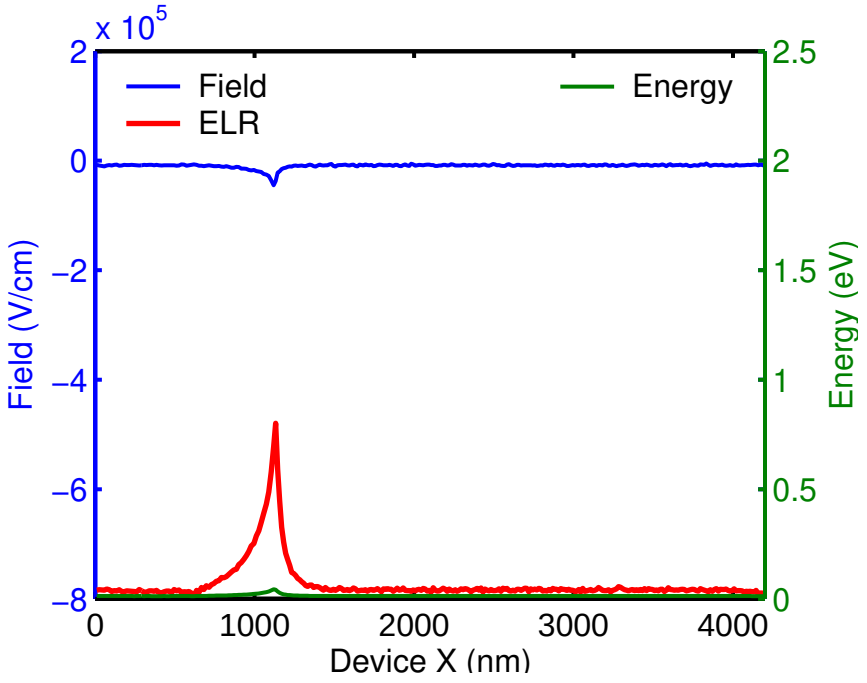

Figure 5.7: Plot of electric field, average energy, and energy loss rate (arbitrary units) profiles along the channel for the long channel device under low drain-source bias (V_{ds} = 5V).

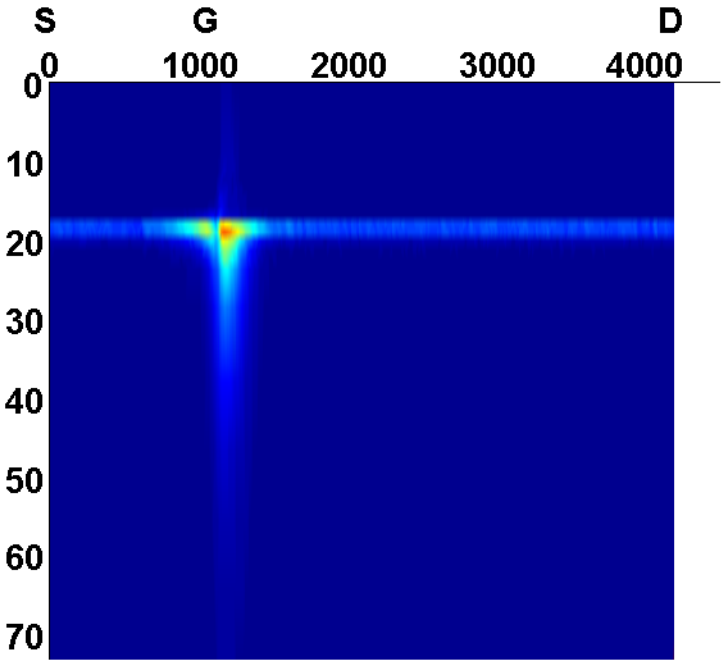

Figure 5.8: Spatial distribution of the non-equilibrium LO mode phonon occupation number for the long channel device under medium drain-source bias (V_{ds} = 10V).

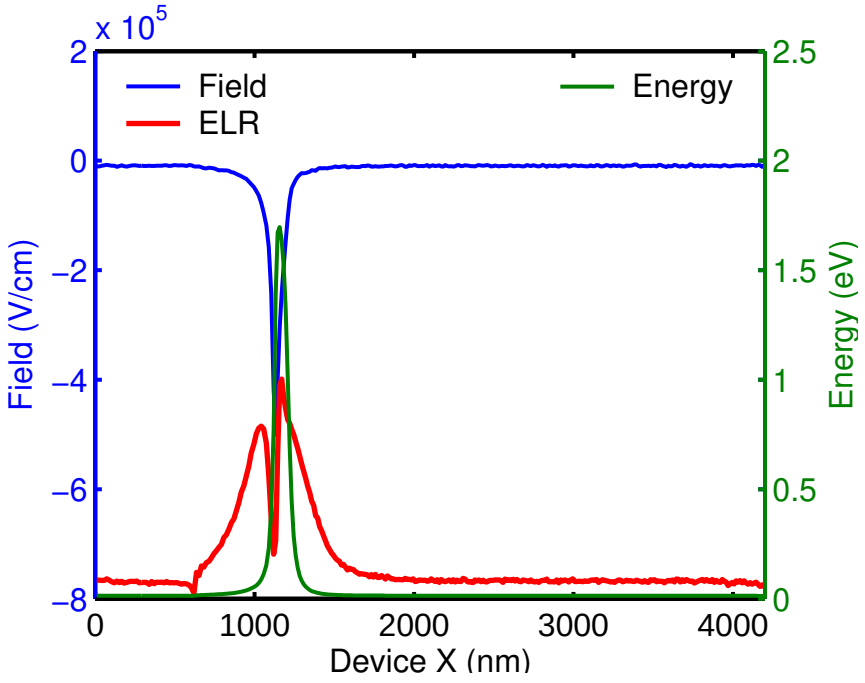

Figure 5.9: Plot of electric field, average energy, and energy loss rate (arbitrary units) profiles along the channel for the long channel device under low drain-source bias (V_{ds} = 10V).

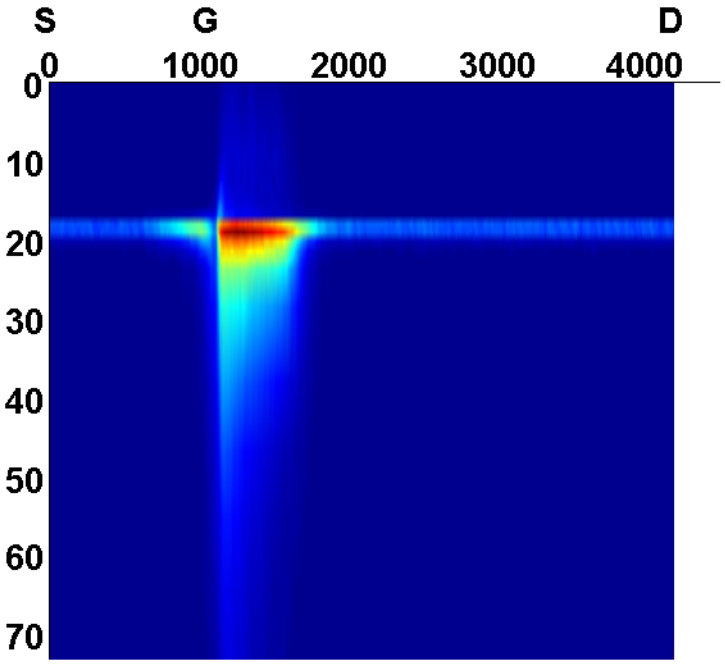

Figure 5.10: Spatial distribution of the non-equilibrium LO mode phonon occupation number for the long channel device under high drain-source bias (V_{ds} = 25V).

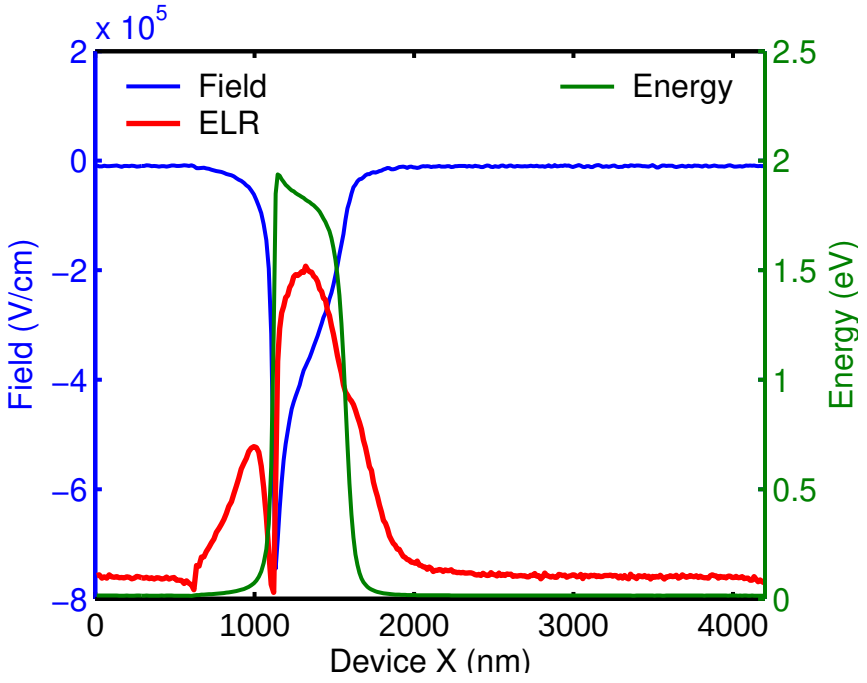

Figure 5.11: Plot of electric field, average energy, and energy loss rate (arbitrary units) profiles along the channel for the long channel device under low drain-source bias (V_{ds} = 25V).

CHAPTER VI

STUDY OF GEIGER MODE HOMOJUNCTION AVALANCHE PHOTODIODES

In this chapter, the design and study of Geiger mode homojunction avalanche photodiodes (APDs) through Monte Carlo simulation is presented. The chapter begins with an introduction to APDs and their Geiger mode operation, followed by the details of modeling and simulation of homojunction APDs. The chapter concludes with the analysis of the simulation results to gain insight into the design of APDs for different applications.

6.1 Avalanche Photodiodes

Avalanche photodiodes (APD) are specially constructed photodiodes that are operated near the avalanche breakdown point. APDs utilize the avalanche multiplication process to achieve large amounts of photo-signal gain without significantly increasing the dark current, resulting in improved signal-to-noise ratio. Development of APDs was driven by high speed fiber optic communications where receivers utilizing APDs provided 5-10 dB better sensitivity [123]. In these applications an APD is used to measure the intensity of an optical signal by taking advantage of the internal gain. An absorbed photon creates, on average, a finite number of electron-hole pairs in the device, and the carriers are extracted faster than they can multiply, causing the current to decay and die out. For a fixed bias below the breakdown voltage, a steady optical illumination produces an average terminal current that is proportional to the incident optical intensity, and this is known as the *linear mode* of operation.

This multiplication process adds an additional component of noise over the amplified shot noise of a regular photodiode. Since impact ionization is a statistical process, the actual gain of the APD can vary significantly from the *average* gain. This fluctuation in gain produces *excess noise*, or *multiplication noise*.

6.1.1 Geiger Mode Operation

APDs are also used in applications that require single photon detection capabilities. These applications include time resolved spectroscopy, laser detection and ranging (LADAR) [124], positron emission tomography (PET) [125], UV-based biological-agent detection systems [126], and measuring temperature of outer space (NASA). Single photon detection using unity gain photodiodes or linear mode APDs would generate terminal currents that are too small to detect. For single photon detection applications APDs are operated in the Geiger mode (GMAPD), where the applied bias temporarily exceeds the breakdown voltage, allowing the possibility of a photogenerated carrier triggering breakdown. The carriers multiply faster than they can be extracted and the current level quickly saturates due to device resistance and space charge effects. The APD thus functions as a digital switch, and is switched on by the detection of a single photon. An external bias circuitry is required to detect the APD turn-on and then turn the APD off to restore it to its initial state for the detection of the next photon. This operation is referred to as quenching. The GMAPD detects a single photon event without adding any read noise to the detection process, and therefore is a true photon detector. However, a thermally generated electron hole pair in the multiplication region can also trigger a breakdown that is indistinguishable from a photon detection event, resulting in a false positive. The number of such events per second is the *dark count rate*. The performance of a GMAPD is measured by its single photon detection efficiency (SPDE), which is a combination of its optical quantum efficiency and breakdown probability. The optical quantum efficiency is the ratio of photogenerated carriers produced to the number of incident photons, while breakdown probability is the probability that a photogenerated carrier triggers breakdown. The main objective in the design of an APD is to maximize SPDE while minimizing dark count rate.

6.1.2 UV Detection

Solid state photodetection in the ultraviolet (UV) spectral region has been a challenge. Wide bandgap (WBG) semiconductors promise several advantages for UV photodetection including solar blind operation and low dark current. WBG *p-i-n* UV photodiodes based

on 4H-SiC with high avalanche gain have been explored for some time. The hole ionization coefficient in 4H-SiC is about 50 times higher than the electron ionization coefficient (k = 0.02), making the hole-initiated impact ionization as the dominant process. A separate absorption-multiplication (SAM) APDs based on 4H-SiC has the advantage of providing single carrier injection and high quantum efficiency. Recently 4H-SiC-based SAM APD having gains as high 1000 have been reported [127].

Wurtzite III-nitride materials are also receiving considerable attention due to recent advances in material quality, fabrication and processing techniques, which have enabled the demonstration of state-of-the-art GaN-based avalanche photodiodes (APDs) with photocurrent gains in excess of 10^4 and dark currents < 10^{-7} A/cm^2 [27]. In order to minimize the dislocation density of the devices, these GaN *p-i-n* APDs are grown by metal-organic chemical vapor deposition (MOCVD) on low defect *n*-type "bulk" GaN substrates. The electron and hole ionization coefficients as a function of electric field strength in GaN are relatively similar, which is not favorable for noise and speed performance characteristics of linear mode APDs. For improving the noise performance of GaN-based linear mode APDs and SPDE of Geiger mode APDs, SAM structures incorporating heterojunction, and impact ionization engineering in the multiplication are being explored.

6.1.3 Modeling and Simulation of APDs

McIntyre [128] studied the multiplication in uniform avalanche diodes, and derived expressions for the noise spectral density of thick multiplication regions under different injection conditions. McIntyre [129] further derived expressions for the distributions of gains that can be used to calculate the average gain and the mean square deviation from the average for any electric field distribution. His derivations were based on the assumption that the electron and hole ionization coefficients were functions of only the local electric field. According to this local-field avalanche theory, both the multiplication noise and the gain-bandwidth product of APDs are determined by the material's electron (α) and hole (β) ionization coefficients in the multiplication region, and better performance is achieved when the ratio of the ionization coefficients (k) is markedly different from unity i.e. when

one carrier (electron or hole) dominates the impact ionization process.

McIntyre's model is a poor approximation for short multiplication regions, as the nature of the impact ionization process is nonlocal, and depends greatly on the history of the particle. Also, the ionization coefficient is not only a function of the local electric field, but also a function of the field gradient, as a particle at a particular field strength is more likely to ionize if it has just left a region of higher field than if it is from a region of low field. Newer models have been developed [130] that take into account the history of the carriers, and employ a new set of field-profile-independent parameters to characterize ionization properties. These models are applicable to arbitrary structures, but may require numerical or Monte Carlo techniques to compute history dependent ionization coefficients.

While McIntyre's initial work primarily focused on the multiplication process below breakdown, Oldham *et al.* [131] studied the breakdown triggering phenomena in avalanche *p-n* junction diodes operating above the breakdown voltage. They derived a set of two differential equations that can be used to compute the breakdown probability, and compared the results favorably with experimental measurements. However, this set of differential equations was hard to solve as it required simultaneous integration of two coupled differential equations, and required numerical methods in practical cases. McIntyre [132] combined these differential equations and applied the approximation $k = \beta/\alpha$ to make them integrable. He derived simpler expressions for the breakdown probabilities involving only the field independent constant k, and demonstrated the validity of the approximation by using known values of k to reproduce previously published calculations of the avalanche initiation probability.

Chandramouli, Maziar, and Campbell have studied excess noise factor, effects of the multiplication layer thickness focusing on thin multiplication regions, and breakdown probabilities in InP APDs using a full band InP Monte Carlo simulator [133, 134]. They have used a wavevector dependent anisotropic threshold energy model for impact ionization based on the Keldysh formula. Neil Goldsman [135] developed a random-k approximation based on the Kane formulation to incorporate impact ionization in numerical solution of the BTE.

Spinelli and Lacaita [136] have developed both a deterministic and a stochastic model using simplified Monte Carlo to model avalanche multiplication in single photon avalanche detectors (SPADs). They have investigated the effects of the statistics of ionizing events, spreading dynamics of the avalanche process, and dead space on timing resolution performance.

The University of Sheffield group has done several studies on the performance of APDs. Chief among them are numerical studies on the avalanche multiplication noise [137–139], random path length based Monte Carlo simulation of the avalanche process [139, 140], effects of dead space on bit-error rate [141, 142], and Monte Carlo device simulation of GaAs [143] and InP-based APDs. A significant portion of their work is on linear mode APDs for communication applications focusing on multiplication noise and gain-bandwidth product. Recently, they have investigated the statistics of current build up in single photon detectors [144] for timing applications, improving on the model by Spinelli and Lacaita.

6.2 Simulation of APDs

Rates for impact ionization, the fundamental process in avalanche photodiodes, are calculated using efficient numerical algorithms that reduce the variance associated with the deterministic and stochastic integration of the differential scattering rates. The additional carriers created by the impact ionization process are carefully tracked. Numerical solution of the Poisson equation provides the electric field strength in the APD, accounting for the applied bias, and any applicable polarization charges at the heterojunction interfaces. The photon absorption probability decays approximately exponentially from the surface, and the spatial distribution of photogenerated electron-hole pairs is determined according to the previously reported field-dependent absorption spectrum of a GaN homojunction p-i-n diode [27]. Photogenerated charge carriers are driven to the high energies required for avalanching by strong internal electric fields in the depletion region of the device. Carriers leaving the high field region become majority carriers in the quasi neutral regions surrounding the depletion region, where they lose their energy through phonon scattering, and are collected at the contacts. The device current is calculated using a current estimator

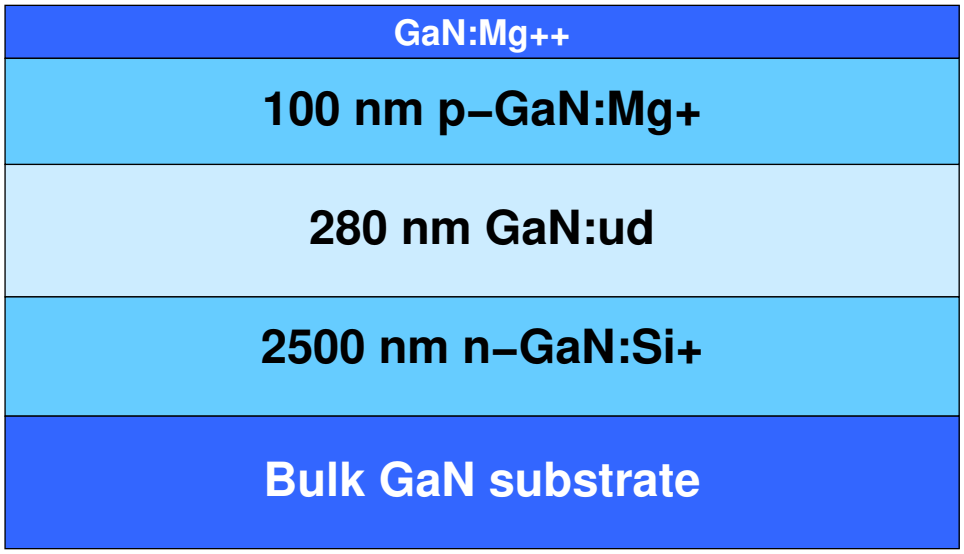

Figure 6.1: Schematic structure of the homojunction APD device.

based on the Ramo-Shockley theorem. Gain calculation is achieved by counting the number of collected particles from each photogenerated carrier. The simulation is performed as a series of impulse responses initiated by a photogeneration event.

Validation of the impact ionization model was achieved through direct comparison of gain and breakdown voltage with previously reported device measurements [3],[ref Dupuis7]. The schematic structure of the measured devices is shown in Figure 6.1. A careful adjustment of high-energy inter-valley and inter-band carrier-phonon deformation potential constants was sufficient to achieve the level of agreement demonstrated in Figures 6.2, 6.3 without significantly influencing the prior calibration of bulk drift velocities. Extraction of bulk impact ionization coefficients from simulation further reveals that the hole ionization coefficient is larger than that of electrons over a wide range of electric field strength as shown in Figure 6.4.

6.2.1 Homojunction APDs

Theoretical investigations into the operation of wurtzite GaN-based homojunction APDs for photon counting applications were performed and the results are presented here. Key design considerations for photon counting applications are the influences of dopant profile, active region thickness and spatial distribution of photon absorption on single photon

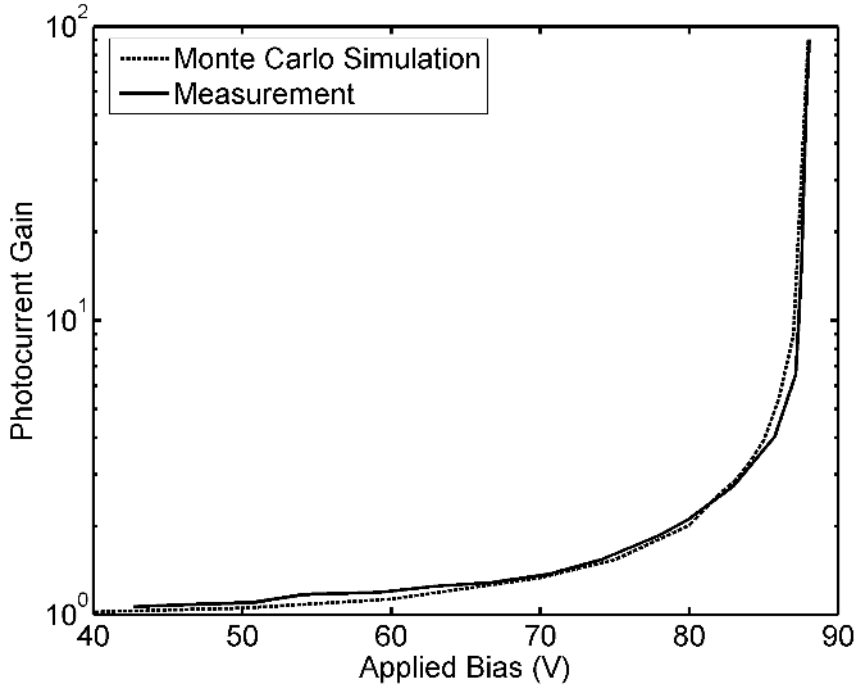

Figure 6.2: Measured [3] and theoretical gain for a GaN APD device A with 280 nm active region thickness.

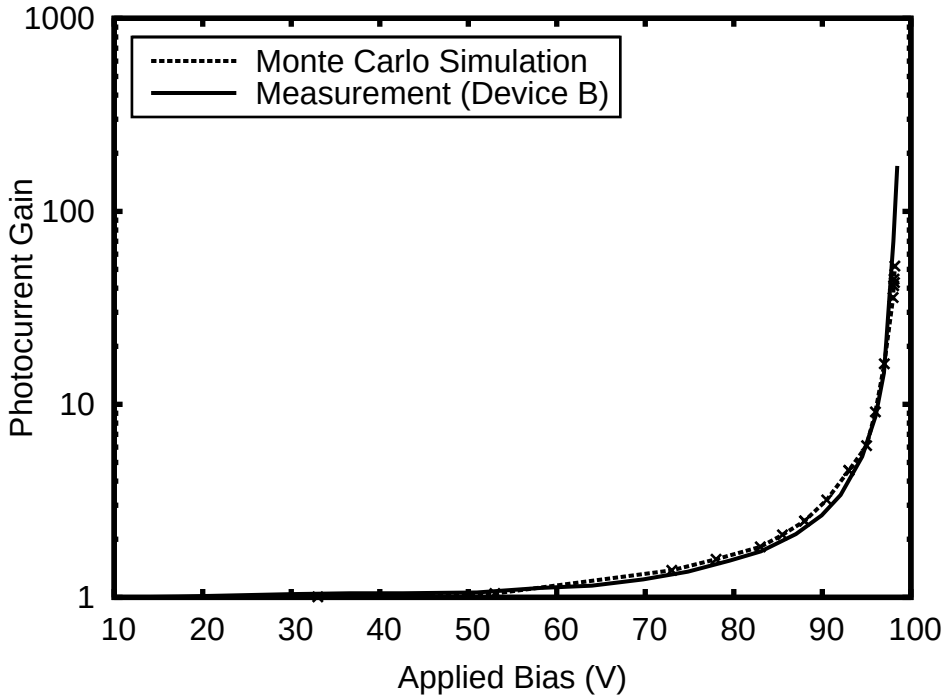

Figure 6.3: Measured [ref Dupuis7] and theoretical gain for a GaN APD device B, also with 280 nm active region thickness but with different device profile.

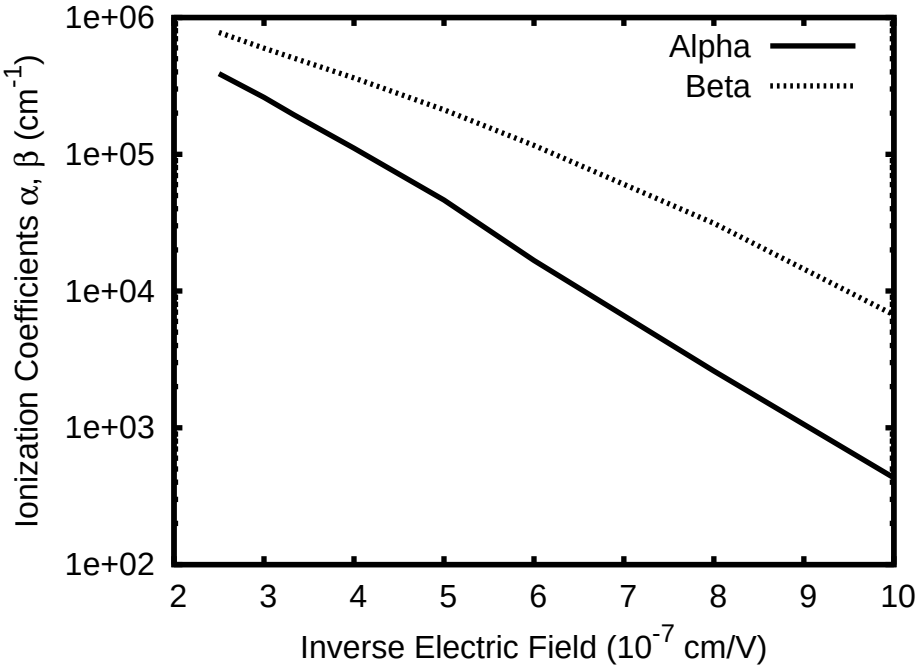

Figure 6.4: Bulk impact ionization coefficients α and β as a function of inverse field strength.

detection efficiency (SPDE). Ultimate limitations imposed by charge transport on avalanche initiation and growth rate likewise influence the maximum precision available for photon timing applications. The relationships between design parameters and device operation were quantified through Monte Carlo simulations to obtain the stochastic solution of the semiclassical Boltzmann transport equation (BTE).

p-up GaN homojunction APD designs under top-illumination were studied using the above model. The epitaxial layer structure considered consists of a 2.50 μm n+ region followed by an intrinsic GaN multiplication region (280-500 μm), on top of which is grown a 0.1 μm thick p+ layer. Due to low minority electron lifetime in GaN material, the p-type quasi-neutral region at the top of the device must be thin enough to avoid any substantial amount of band-to-band recombination, yet thick enough to avoid becoming fully depleted under bias. Based on the results of our simulations, the influences of dopant profile, active region thickness and photon absorption profile on SPDE, are discussed in the following section.

For the case of steady UV illumination and bias, Figure 6.5 demonstrates that the

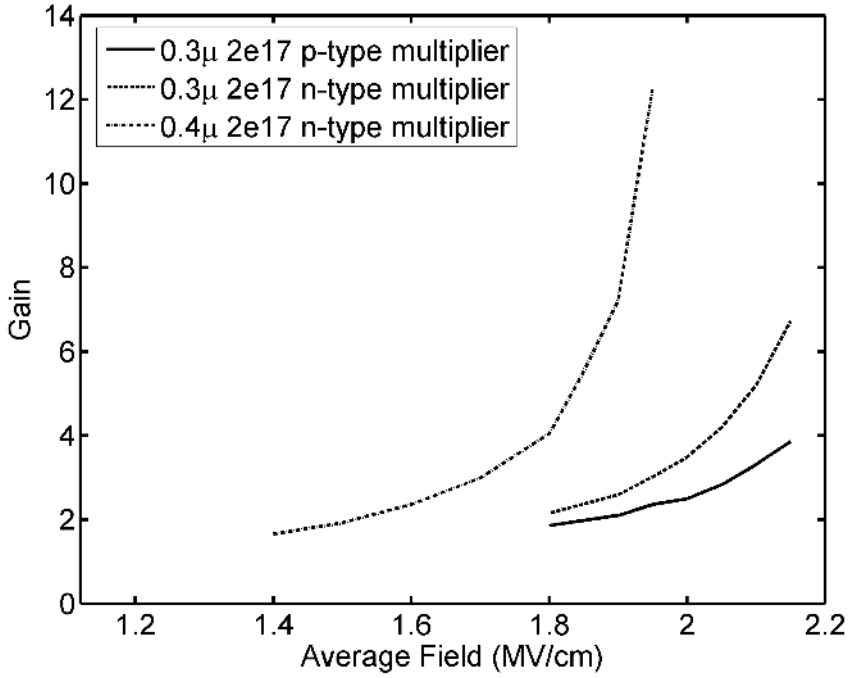

Figure 6.5: Both multiplication region thickness and dopant profile can exert significant influence on gain.

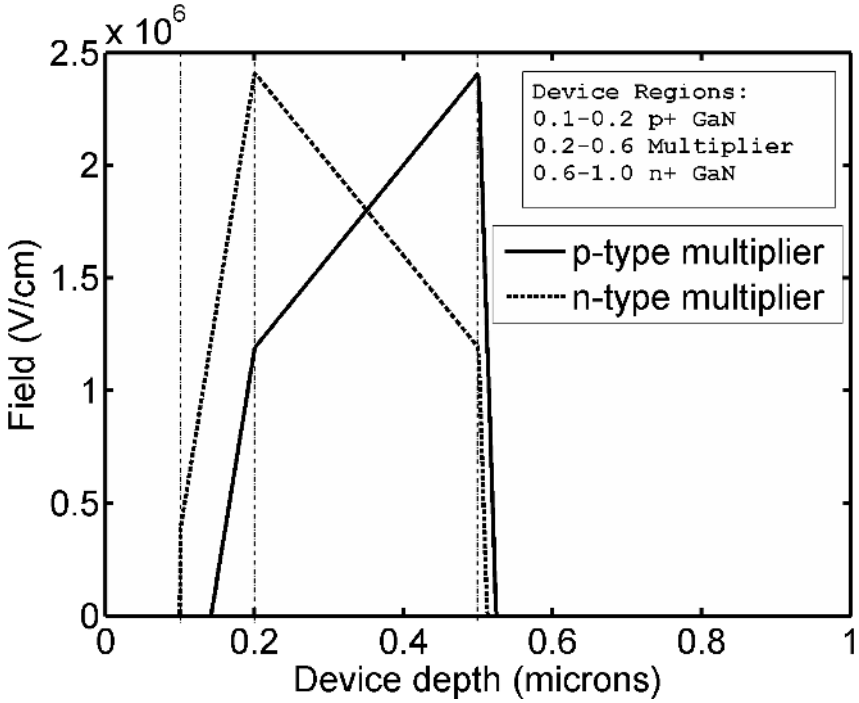

Figure 6.6: Electric field profiles may be designed for optimal photocurrent gain through control over dopant distribution.

electric field strength required to achieve a given gain is a function of multiplication region thickness, enabling flexibility of design to partially suppress dark current. For a given multiplier thickness, Figure 6.5 also shows that photocurrent gain is sensitive to the detailed field profile, and not simply to the average field. As a direct consequence of topside illumination and the dominance of hole-initiated impact ionization in GaN, n-type doping of the multiplication region leads to significantly higher gain for a given applied bias. Field profiles for both dopant species, corresponding to identical applied bias, are shown in Figure 6.6 for illustration.

During the detection cycle of Geiger mode operation, applied bias temporarily exceeds the steady-state breakdown voltage, and electron-hole pairs photogenerated inside or within a diffusion length of the high-field active region may initiate a finite number of impact ionization events, none at all, or trigger breakdown. The probability of the latter depends on both the position of photogeneration (see Figure 6.7), as well as the amount of overbias. Calculations of breakdown probability as a function of overbias ratio are shown in Figure 6.8, and demonstrate that the probability of triggering breakdown is enhanced by the use of thicker multiplication regions. The thicker multiplication region also exhibits reduced breakdown field strength and achieves a given breakdown probability at a lower overbias ratio than thinner multiplication regions. This reduction in electric field may be exploited to suppress field-activated contributions to dark current, and reduce the instances of false positives. In addition to increased breakdown probability and reduced leakage current, thicker active regions also lead to higher SPDE by virtue of their greater quantum efficiency.

Photon timing applications, on the other hand, are known to benefit from thinner multiplication regions. Our simulations demonstrate that the rate of growth for Geiger mode photocurrent (after a brief initial "avalanche initiation" phase), is a decreasing function of multiplication region thickness, as shown in Figure 6.9. This phenomenon can be explained qualitatively within the framework of the first two moments of the Boltzmann transport equation, which admits approximate analytic solutions of the form $I(t)e^{(\alpha+\beta)\nu t}$ in the limit of spatially invariant avalanche coefficients. Here, ν is the geometric mean of the

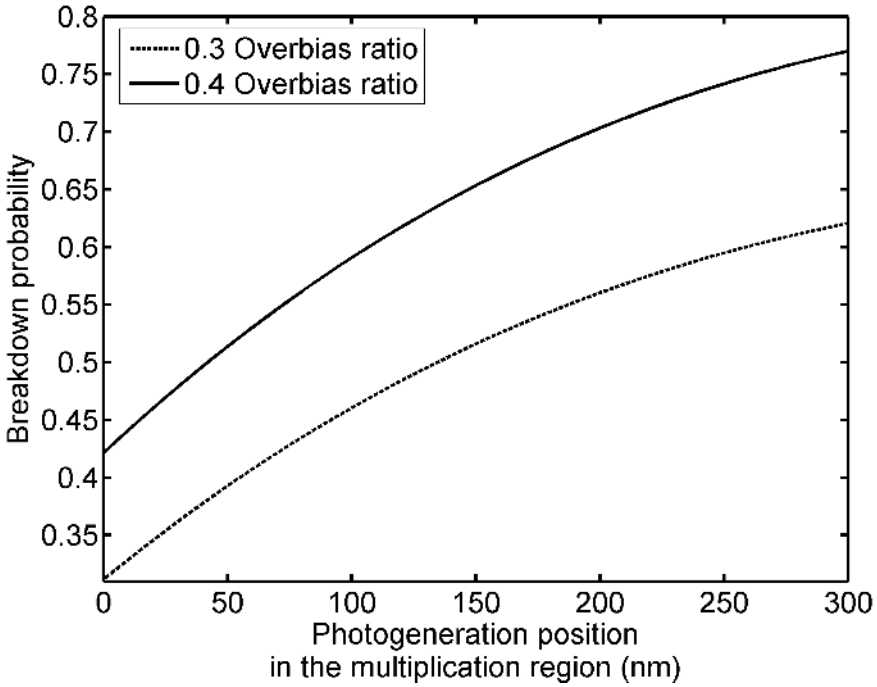

Figure 6.7: Probability of triggering breakdown is a function of photogeneration position, and is highest for holes injected from the *n*-side depletion region boundary.

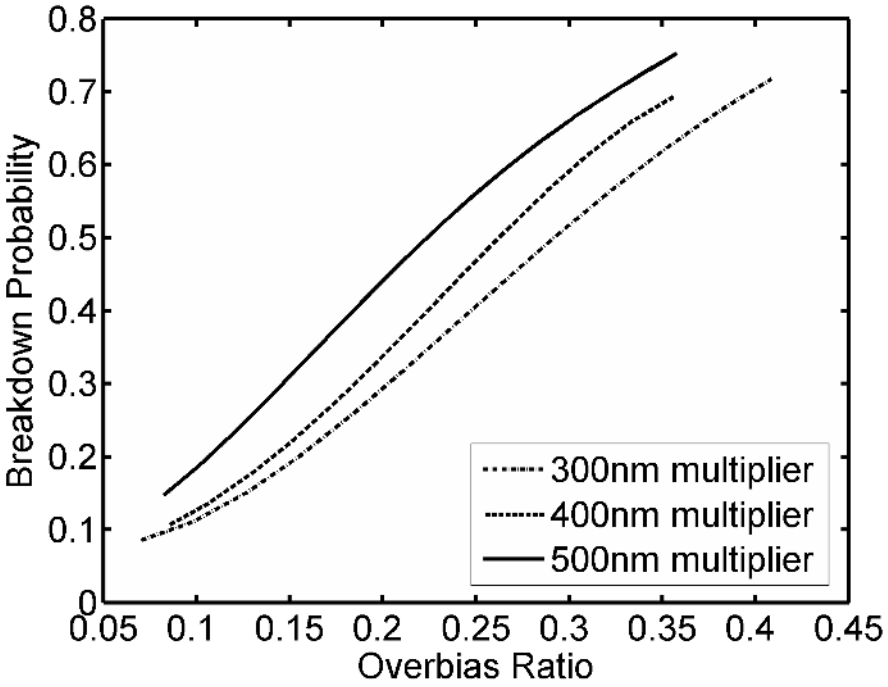

Figure 6.8: For a given overbias ratio, thicker multiplication regions offer greater breakdown triggering probability.

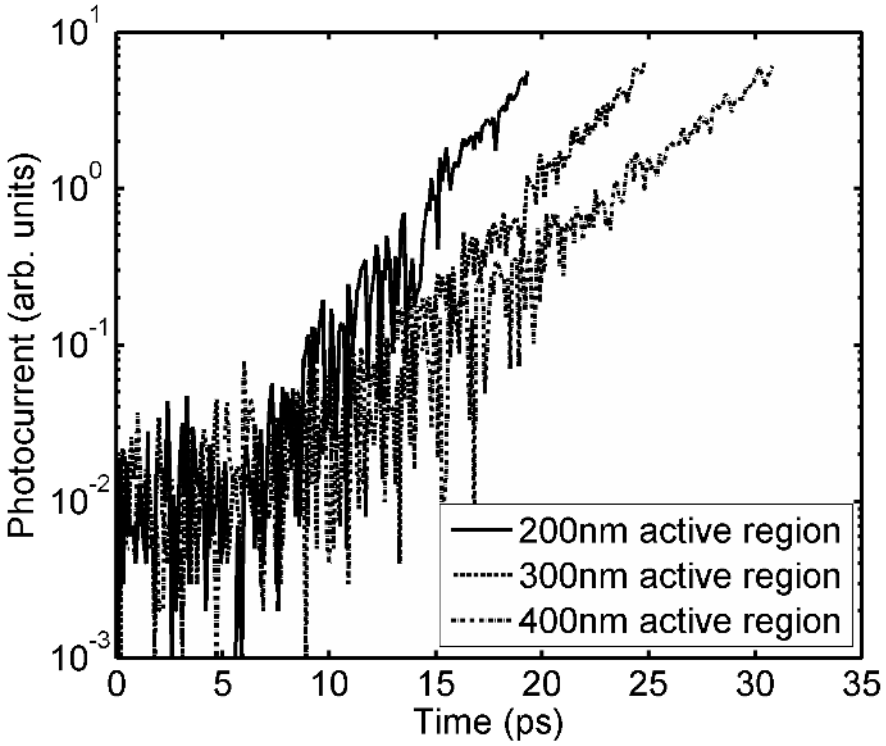

Figure 6.9: Geiger mode photocurrent grows fastest for a given overbias ratio in the limit of thin active regions.

electron and hole saturated drift velocities, and so are the field-dependent electron and hole ionization coefficients, respectively. Although saturated carrier velocities remain approximately constant at high fields, ionization coefficients exhibit exponential dependence on field strength. It is inferred from Figure 6.8 that the ionization coefficients as well as average field strength in the active region are necessarily larger for devices with thinner active regions than for those with thicker active regions. This observation links the trend depicted in Figure 6.9 with the approximate characteristic time constant $[(\alpha + \beta)v]^{-1}$.

CHAPTER VII

STUDY AND DESIGN OF HETEROJUNCTION AVALANCHE PHOTODIODES

The single photon detection efficiency (SPDE) of homojunction APDs presented in the previous chapter is limited by several factors such as photon absorption profile, dark current, and field profile. This chapter explores heterojunction APDs and provides valuable insight into their operation gained from Monte Carlo simulation. Based on these results, a new device structure for improved SPDE is proposed and demonstrated.

7.1 Heterojunction APDs

As demonstrated in the previous chapter breakdown probability is a strong function of multiplication region thickness and improving the breakdown probability requires the use of thicker multiplication region, which also increases the dark current. Also, in the case of homojunction APDs, a significant fraction of the incident photons are absorbed throughout the high-field multiplication region, resulting in a large excess noise factor due to the strong position dependence of gain and breakdown probability. To improve the noise factor and quantum efficiency, a separate absorption and multiplication APD (SAM-APD) structure was developed. The SAM-APD uses a AlGaN/GaN heterojunction with a narrow bandgap absorber and a wide bandgap multiplier. This structure, schematically shown in Figure 7.1, has three main advantages:

1. Dark current: Due to the wider bandgap of the multiplication region, the dark current is significantly reduced, enabling the use of thicker multiplication regions required for better performance.

2. Excess noise: The wider bandgap of the multiplication region reduces photon absorption in the multiplication region, improving the excess noise factor.

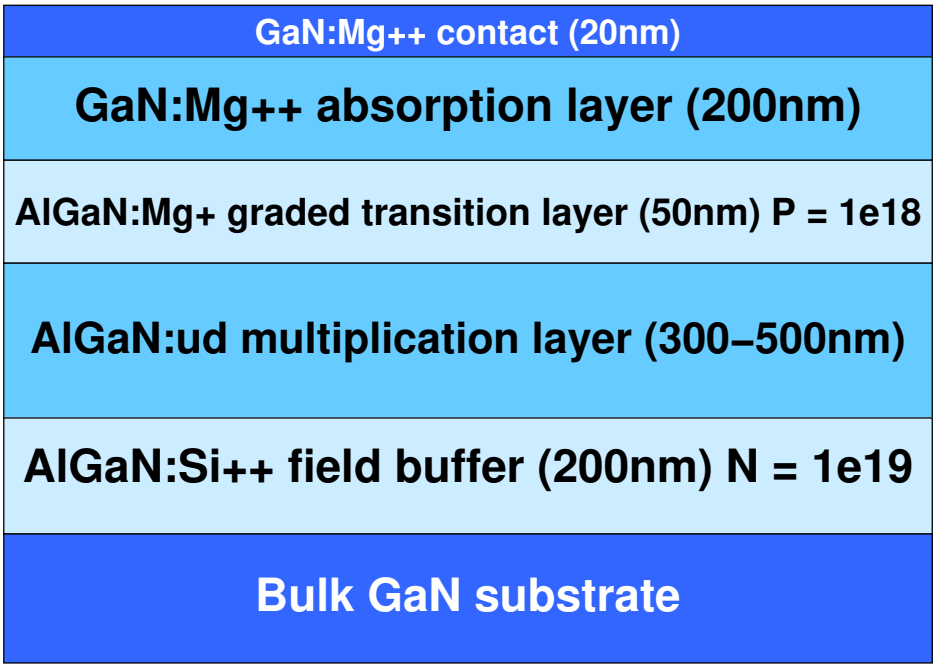

Figure 7.1: Schematic structure of the heterojunction APD device.

3. Polarization charges: The presence of strong piezo-electric and spontaneous polarization charges at the heterojunction interface enables favorable field profile with a low field in the absorption region, and a high-field in the multiplication region. The low field in the narrow bandgap absorption region reduces the dark current, as dark current increases with increasing field strength. Secondly, the polarization charge enables high field strength in the multiplication without fully depleting the absorption region. This allows the use of a thicker, lightly-doped absorber, improving the quantum efficiency and reducing the dark current due to the lighter doping.

An heterojunction APD with an n-type AlGaN multiplier and a p-type GaN absorber was studied. The device structure consists of a 200nm Si-doped n+ $Al_{0.1}Ga_{0.9}N$ field buffer layer grown on top of a GaN substrate followed by an 300-500nm unintentionally doped $Al_{0.1}Ga_{0.9}N$. A graded transition layer, a 200nm Mg+ doped p-type GaN absorption layer, and 20nm highly p-doped cap layer grown on top complete the device. With the objective of maximizing breakdown probability, electron-hole pairs were generated at uniformly

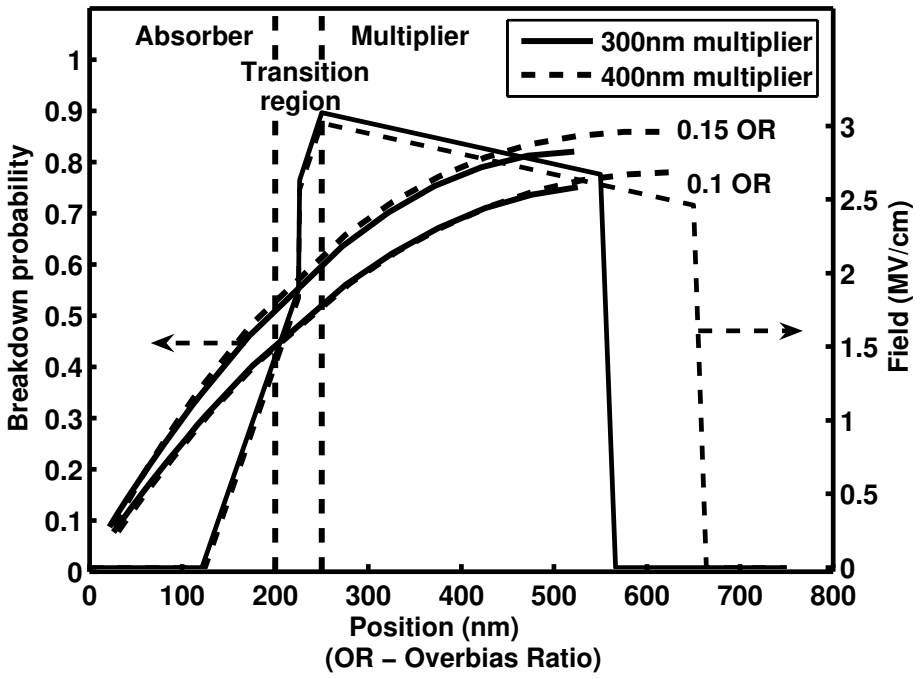

Figure 7.2: Photogeneration position dependent breakdown probability and field profile.

spaced positions along the device and the breakdown probability was calculated by averaging over 5000 trials at each position. The minority carriers generated in the undepleted portion of the device were allowed to diffuse and would contribute to gain upon reaching the depletion region boundaries. Figure 7.2 shows a plot of the breakdown probability as a function of the photogeneration position along the device for 300nm and 400nm multiplication region thicknesses and overbias ratios of 0.1 and 0.15. Due to the dominance of hole-initiated impact ionization, the observed breakdown probability is higher for carriers generated close to the n-side depletion region boundary, and for the same overbias ratio the thicker multiplication region clearly provides higher breakdown probability. Figure 7.2 also shows that for the same overbias ratio, the average field strength in the longer multiplier is also lower, resulting in lower field induced dark current component.

A plot of the SPDE of this structure as a function of overbias ratio for different multiplication and absorption region thicknesses, as shown in Figure 7.3, clearly demonstrates that a thin absorber combined with thicker multipliers yields the most efficient device. A thin absorber device biased at high overbias ratios runs the risk of completely depleting the

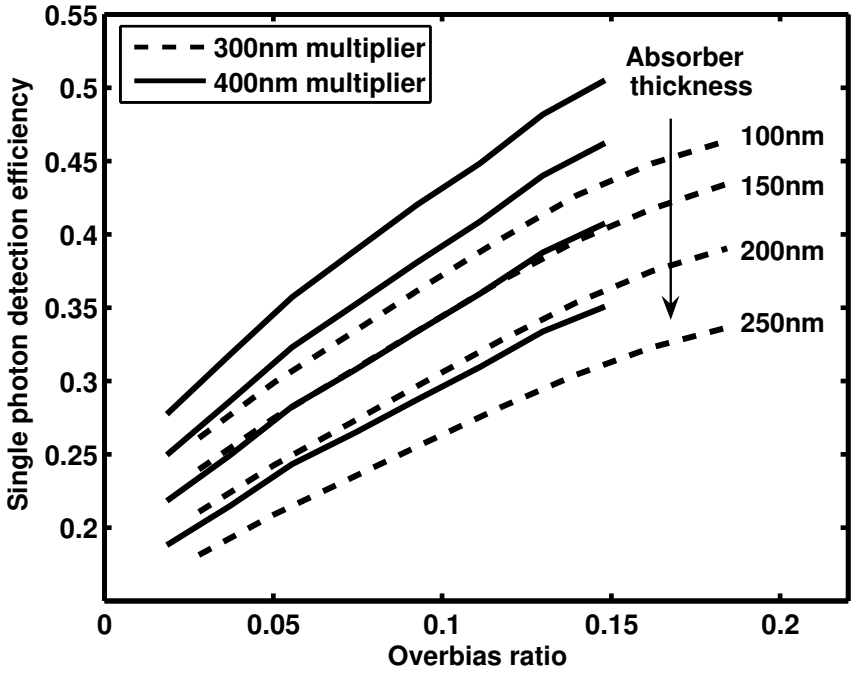

Figure 7.3: Single photon detection efficiency of AlGaN/GaN heterojunction APD structure.

absorption region, resulting in electron injection directly from the contacts. To maximize SPDE, the device requires a higher doping in the graded transition region and a higher mole fraction of the AlGaN multiplier, both of which would reduce the penetration of the depletion region into the absorber, enabling thin-absorber devices to safely operate at higher overbias ratios.

7.2 Design optimization of heterojunction APDs

The calculated breakdown probability of the heterojunction APD at a given overbias ratio is already higher than that of the homojunction APD. However, the overall SPDE, which accounts for the optical absorption profile, is still less than 50% (Figure 7.3). Investigating the lower than desirable efficiency reveals that the absorption region captures only 30% of the photons due to the slightly weaker optical absorption (18000/cm) and injects electrons into the multiplication region from the p-side depletion region boundary. Furthermore, a study of the breakdown probability due to pure electron injection into the multiplication region, plotted in Figure 7.4, indicates that a sizable fraction of the injected electrons

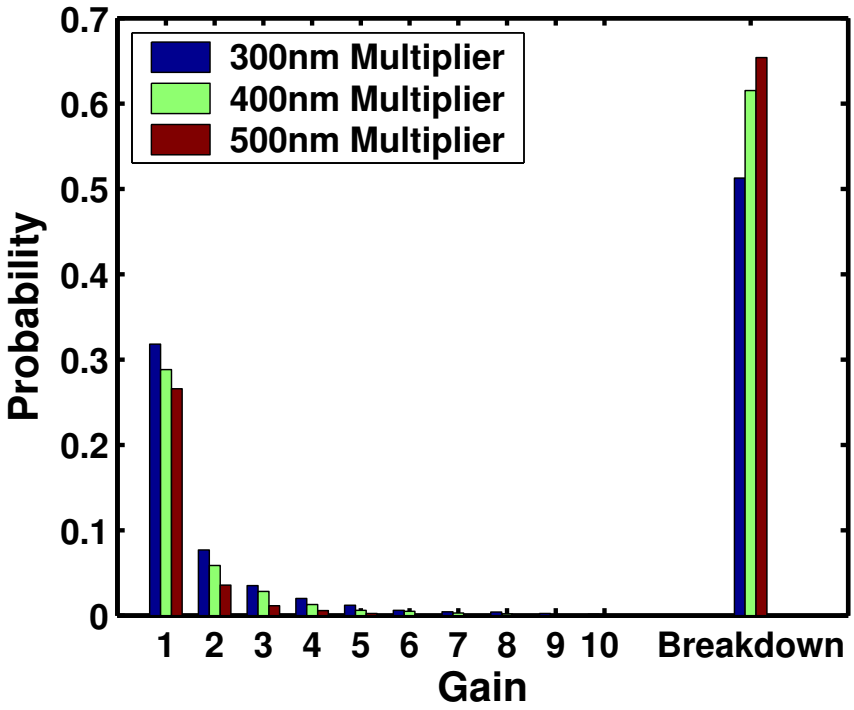

Figure 7.4: Breakdown probability statistics for an overbias ratio of 0.3.

traverses the multiplier without initiating a single impact ionization event. Both of these deficiencies can be improved by placing the absorption region below the multiplication region. The heterojunction APD was redesigned by moving the n-type GaN absorption region below the multiplication region as schematically represented in Figure 7.5. Buffer regions and graded transition regions were added to tune the field profile. Figure 7.6 shows the field profile of a device with a 500nm multiplication region biased at an overbias ratio of 0.5. The use of an heterojunction provides polarization charges that enhance the field transitions at the edges of the multiplication region. This allows the top cap layer and the quasi-neutral layer to be very thin, thereby reducing absorption in the quasi-neutral material for top-illuminated designs to a far greater extent than would be possible with a GaN homojunction APD. The enhanced field transition also enables a low average field strength in the unintentionally doped absorber, which limits the potential dropped across this region and keeps the breakdown voltage under control. The absorption region is lightly doped (unintentionally) to reduce carrier recombination and dark current. The absorption region is also considerably thicker (500-1000nm) to improve the optical quantum

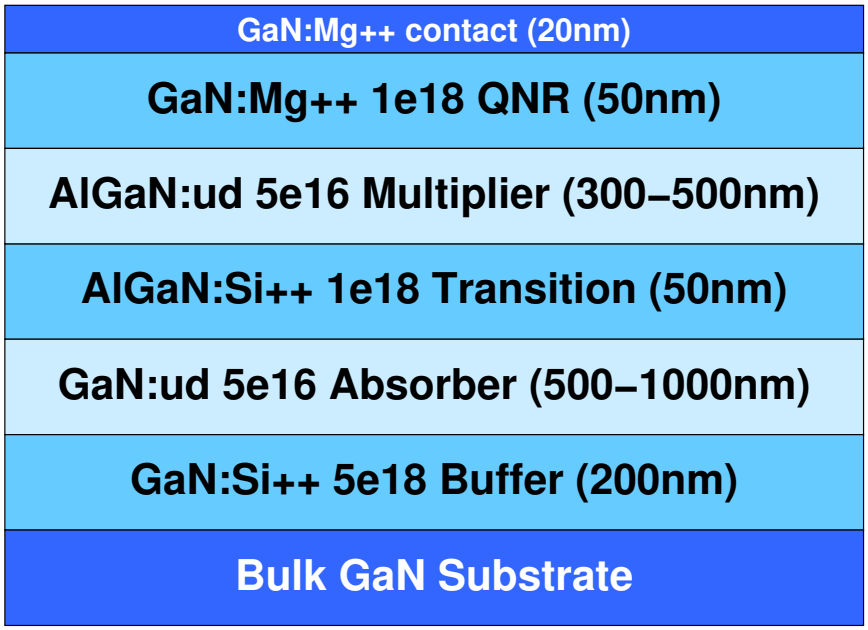

Figure 7.5: Redesigned heterojunction APD structure.

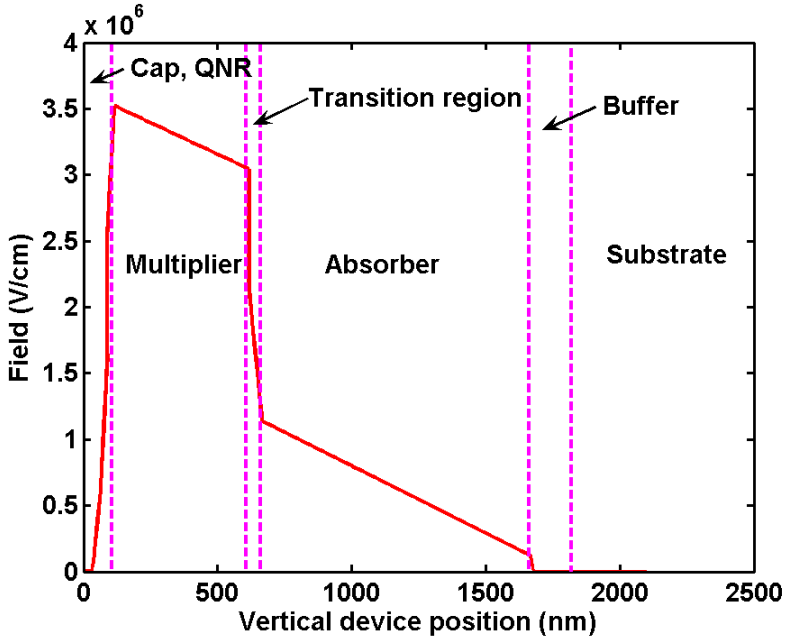

Figure 7.6: Field profile in the redesigned heterojunction APD.

efficiency and a higher SPDE is achieved by injecting the dominant holes from the n-side multiplication region, where breakdown probability is highest. Furthermore, the use of a wide-gap multiplication region reduces optical absorption within the multiplier itself, resulting in greater absorption in the low-field GaN region below, while improving the excess noise factor.

Figure 7.7 shows the breakdown probability in the new structure as function of photo-generation position for 300nm and 400nm multiplier devices, both operating at an overbias ratio of 0.3. The optical absorption profile for both the device geometries is overlaid on the plot showing reduced absorption in the wider band gap multiplier, where the optical absorption coefficient, α_{AlGaN}, is 15,300/cm compared to 18,000/cm for α_{GaN}. For a 400nm multiplier device operating at an overbias ratio of 0.3, the overall SPDE is calculated to be 64.7%. A similar GaN homojunction APD with comparable breakdown probabilities and field profile in the multiplication region requires a 200nm quasi-neutral region doped p-type to $1 \times 10^{18}/\mathrm{cm}^3$ at the top. The overall SPDE of the homojunction device operating at an overbias ratio of 0.3 is calculated to be 54%.

Figure 7.8 shows the SPDE as a function of overbias ratio for three different multiplier thicknesses. The improvements in both optical quantum efficiency and breakdown probability yield an SPDE of 73% for the 500nm multiplier device operating at an overbias ratio of 0.58. This SPDE is the highest achieved so far and is significantly higher than that of the heterojunction SAM-APD and the homojunction APD designs described earlier.

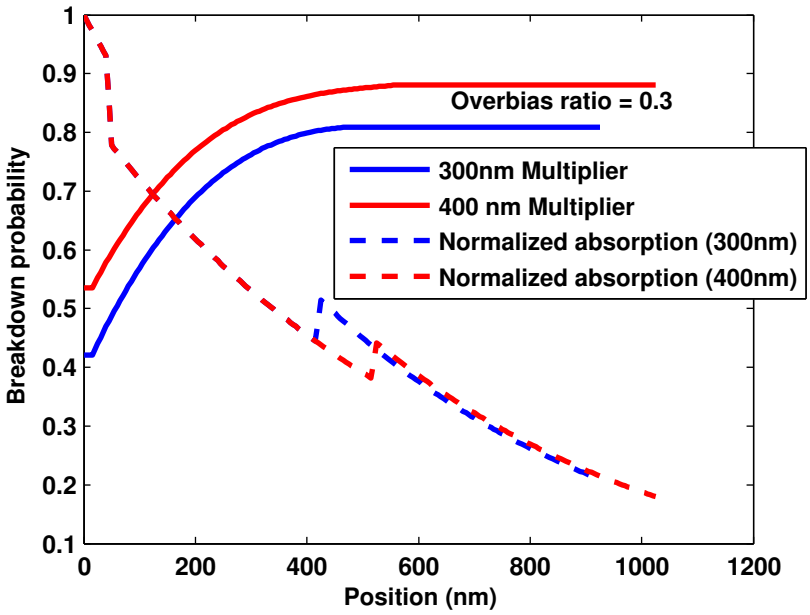

Figure 7.7: Optical absorption profile and position dependent breakdown probability of the redesigned heterojunction APD structure.

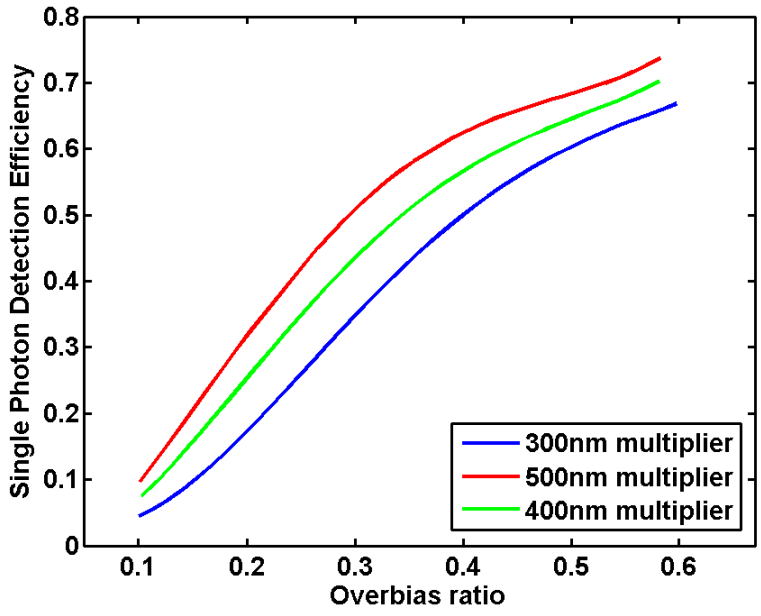

Figure 7.8: Single photon detection efficiency vs. overbias ratio for the redesigned heterojunction APD structure.

CHAPTER VIII

STUDY OF TRAVELING DIPOLE DOMAINS IN ALGAN/GAN HETEROSTRUCTURES

8.1 Introduction

This chapter introduces the Gunn effect and highlights the favorable properties of wurtzite III-nitride in the production of Gunn diodes followed by a discussion of the challenges associated with the bulk Gunn effect in GaN. A new approach for the direct generation of self-sustaining millimeter-wave oscillations in this material system is presented. Lastly, sustained millimeter-wave oscillations in an AlGaN/GaN triode structure is demonstrated by means of full-band ensemble Monte Carlo simulation.

8.2 Gunn effect and the transferred-electron device

The transferred-electron device (TED) is an important microwave device that has been extensively used as primary devices for oscillators and power amplifiers in micro- and millimeter-wave applications operating at frequencies ranging from a few GHz to hundreds of GHz [145–148]. TEDs are widely used in micro- and millimeter-wave applications such as oscillators in radio communications [149], military and commercial radars [150], modulation of semiconductor lasers [151], motion detectors, and sensors for detecting velocity, direction, proximity [150, 152].

Oscillations in TEDs are produced by negative differential resistance (NDR) exhibited, for example, by III-V semiconductors [153]. In general, NDR is caused by microscopic bulk semiconductor properties such as field enhanced trapping [154], impact ionization of shallow impurity levels in compensated semiconductors [155], but the primary NDR in TEDs is due to the field-induced transfer of conduction band electrons from a low-energy high-mobility valley to a high-energy low-mobility satellite valley, known as the transferred-electron effect. The oscillations due to NDR were first observed by Gunn and

was later confirmed to be specifically due to the transferred-electron effect. Hence, the transferred-electron effect is also known as the Gunn effect. The effect is also referred to as the Ridley-Watkins-Hilsum effect who independently proposed the theory of oscillations due to negative differential resistance [153, 156].

A semiconductor exhibiting NDR is inherently unstable when biased above the threshold electric field strength necessary for NDR. A perturbation in the electric field profile at any point in the material, either spatially or temporally, produces a charge imbalance that grows over time. The charge imbalance grows and propagates in two different modes, namely accumulation-layer mode and dipole-layer mode. Consider the accumulation-layer mode of operation: in a voltage-controlled NDR device biased to the NDR regime, a small local spike in the electric field strength due to a dopant fluctuation, for instance, leads to a local increase in the resistivity due to NDR. This implies that the number of carriers flowing into this region is greater than the number of carriers flowing out of this region, resulting in a local accumulation of carriers inside the region. The accumulation region splits the electric field profile into a low-field region and a high-field region consistent with the Poisson equation. With a constant applied bias, the accumulation region grows while moving towards the anode contact, which collects the accumulated carriers and the accumulation region disappears. The initial local field spike grows again and the entire process repeats, leading to sustained oscillations.

When a device has both positive and negative charges separated by a small distance due to a static perturbation in the electric field profile such as under the gate electrode, a dipole domain is formed. The electric field inside the dipole domain is greater than the electric field on either side of the domain. The dipole domain reaches an equilibrium configuration such that the currents in the high-field region inside the domain and the low-field regions outside the domain are the same due to NDR. This domain moves through the device, disappears at the anode, and a new domain forms at cathode end of the device, resulting in the dipole-layer mode of oscillations. Further description and analysis of TEDs can be found in [157].

8.3 Gunn instability in GaN

Relative to GaAs and InP, materials which have been used extensively in the production of Gunn diodes, the wurtzite III-nitride material system offers many superior electrical and thermal properties. The significantly greater field strengths required for both dielectric breakdown and the onset of negative differential drift velocity point towards the opportunity for higher output power, while the larger peak and saturated drift velocities offer the promise of higher operating frequency [158, 159]. Negative differential drift velocity in n-type wurtzite GaN was first predicted by Littlejohn *et al.* [160] and has been verified experimentally [161], yet in spite of the wealth of documented theoretical investigations of GaN-based Gunn diodes [159, 162–166], not a single such device has yet been demonstrated experimentally. In the following sections, the challenges associated with a bulk Gunn effect in GaN is discussed, and an orthogonal approach to the direct generation of millimeter-wave oscillations in this material system is presented. Further, sustained millimeter-wave oscillation is demonstrated by means of full-band ensemble Monte Carlo simulation.

8.3.1 Bulk GaN material

The detail study of charge transport in bulk Wurtzite GaN was presented in Chapter 3. At 300K, a peak electron drift velocity of approximately 3×10^7 cm/s in undoped wurtzite GaN occurs at an electric field strength of around 150 kV/cm as shown in Figure 3.3. Above this threshold, drift velocity is a monotonically decreasing function of field strength, falling only to approximately 2×10^7 cm/s at 500 kV/cm, representing a span of 350 kV/cm. Only a few kV/cm, however, separate the field strengths at which peak and saturated electron drift velocity occur in GaAs. Due to this gradual drop in drift velocity as a function of field strength, Alekseev and Pavlidis [159] have estimated the intrinsic negative differential resistance of wurtzite GaN to be 50 times weaker than that of zincblende GaAs [159]. As a direct consequence, the electric field strength which must be maintained within a viable traveling dipole domain is necessarily far higher in GaN than in GaAs, and this field must be supported primarily within the leading, depleted portion of the dipole domain. Various authors have noted [159, 164, 166] that this in turn imposes a

significantly higher minimum value on the product of doping density and active layer thickness, nL_{th}, required for Gunn oscillation. In particular, Barry, Sokolov, Kim and Trew estimate that the active layer doping must reach $10^{18}/\text{cm}^3$ for high-speed devices of reasonable thickness [166]. A subtle phenomenon associated with heavy doping, often neglected in theoretical analysis, is the degradation of not just Ohmic drift mobility, but peak electron velocity as well. Figure 3.9 depicts the doping dependence of the stationary velocity-field relationship for electrons in bulk wurtzite GaN, as calculated in Chapter 3 using the full-band ensemble Monte Carlo charge transport model. From these calculations, it is clear that the high doping levels required to sustain traveling dipole domains in bulk GaN significantly compromise the intrinsic negative differential resistance upon which Gunn instabilities are based. Furthermore, because the electric field strength at which peak stationary drift velocity occurs is a monotonically increasing function of doping density, actual requirements for the minimum nL_{th} product are even more restrictive than the estimates provided by Barry et al. These considerations may likely preclude the formation of self-sustaining Gunn domains in bulk GaN at room temperature.

8.3.2 Polar heterojunctions

Polar heterojunctions of wurtzite III-nitride material enable the realization of exceedingly high electron densities in the presence of fixed interfacial charge of equal magnitude but opposite sign [167]. In contrast to the ionized impurity scattering introduced by the random spatial distribution of bulk dopant atoms, the high correlation in the positions of the interfacial lattice sites at which polarization charge is located ensures conservation of the in-plane component of crystal momentum in electrostatic interactions with mobile electrons. For this reason, the effect of even large polarization charge on the in-plane transport properties of electrons is relatively small. To realize dipole instabilities within the two-dimensional electron gas (2DEG) formed at a polar heterojunction, a simple triode structure such as the one used for AlGaN/GaN-based high electron mobility transistors, is proposed Figure 8.1. At sufficient gate and drain bias with respect to the source electrode, field crowding underneath the drain edge of the gate electrode will generate a longitudinal

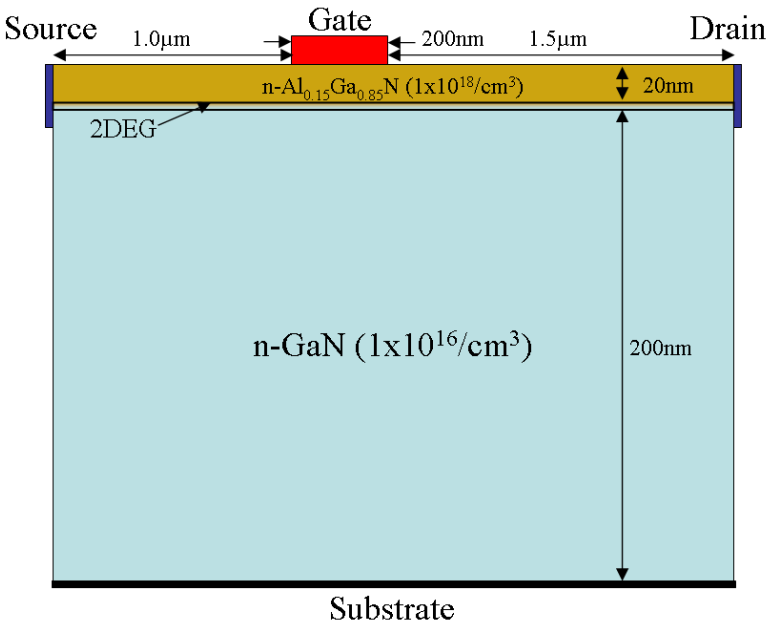

Figure 8.1: In this prototypical oscillator structure, field crowding at the the gate electrode may be exploited to nucleate traveling dipole domains.

component of the electric field within the channel in excess of the threshold for negative differential drift velocity. It is precisely the location of this spike in longitudinal electric field which serves as the nucleation site for dipole instabilities.

8.4 Theoretical model

The full-band ensemble Monte Carlo method [42] is used to model electron transport throughout the two-dimensional device domain of Figure 8.1, with bulk electronic dispersion calculated for wurtzite III-nitride material according to the method of non-local empirical pseudopotentials described in Chapter 2. Electron scattering mechanisms considered include the Fröhlich interaction, deformation potential scattering, ionized impurity scattering, piezoelectric scattering, and impact ionization. Detailed description of these mechanisms and the theoretical model are presented in Chapter 2. A non-equilibrium or "hot" LO phonon distribution is accounted for throughout the device by means of a set of rate equations for occupation number which are enforced at each grid node, and solved self-consistently with the Monte Carlo simulation. Electrostatic self-consistency is achieved through synchronous solution of the 2D Poisson equation at sub-femtosecond time steps.

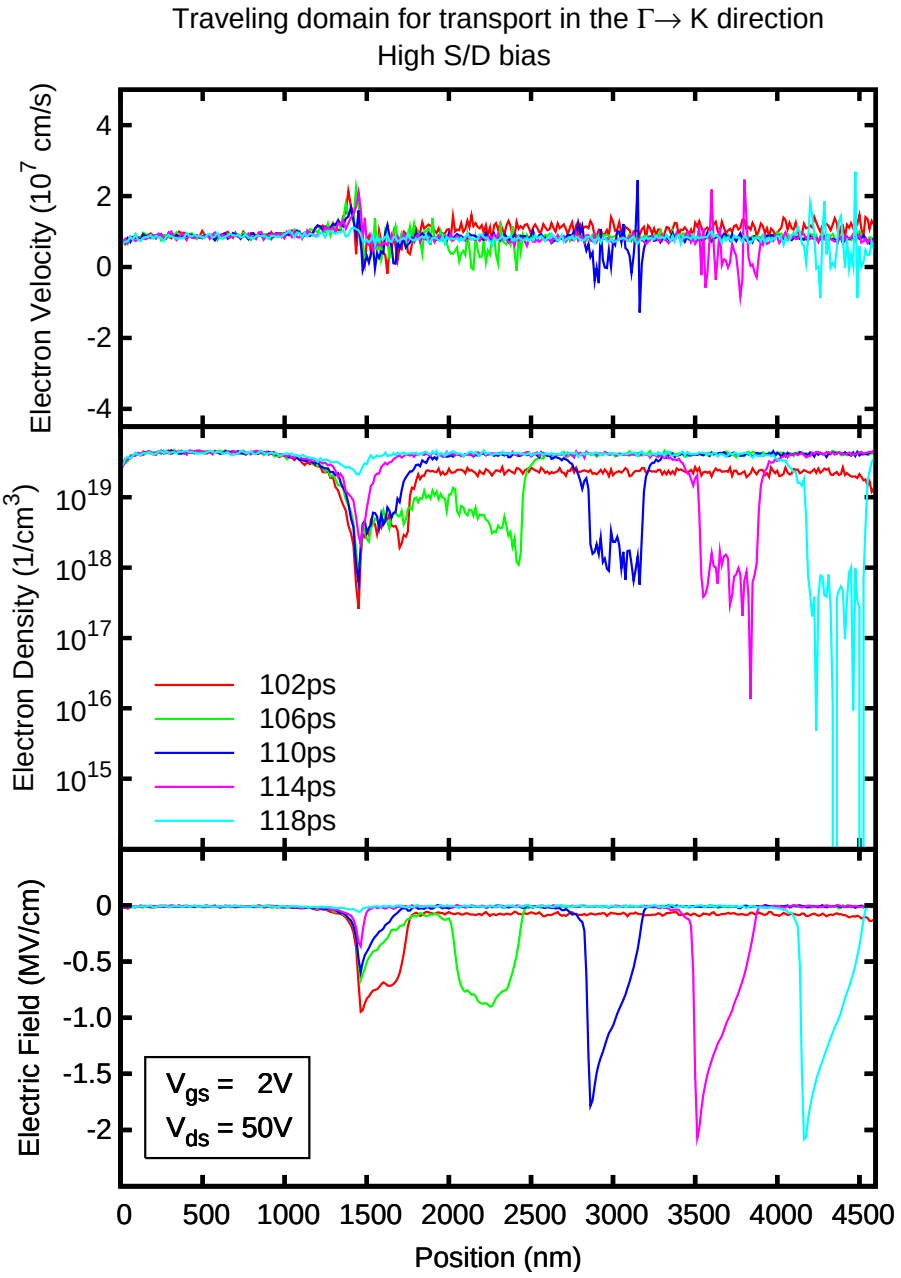

Figure 8.2: Nucleation of the dipole instability occurs at approximately 1300nm, followed by growth, forward propagation, and ultimate collection at the drain electrode.

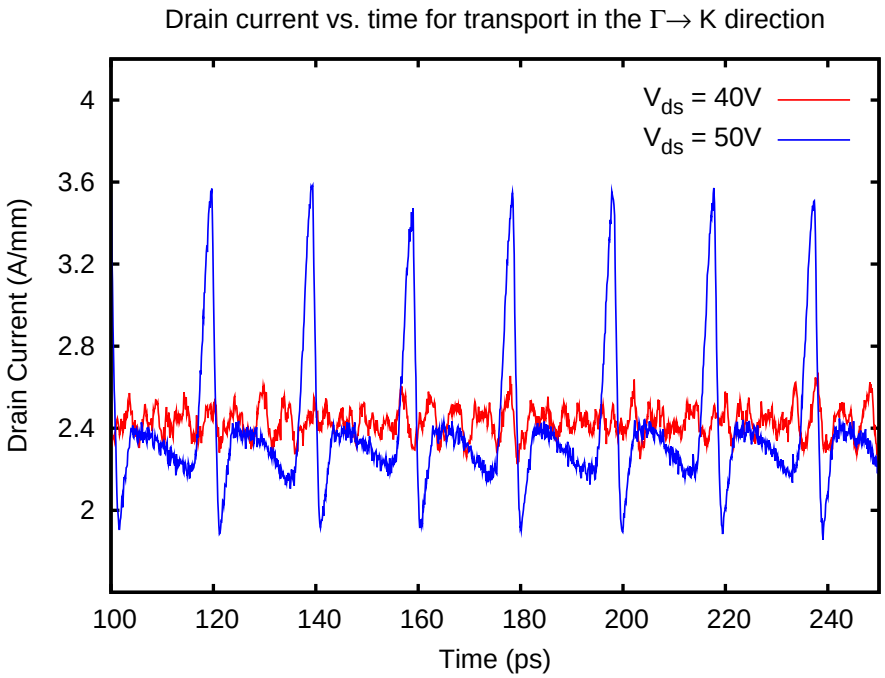

Figure 8.3: Load current oscillation at 51 GHz is observed for Vgs=2V and Vds≈50V.

8.5 Results and discussion

The aforementioned theoretical model has been applied to study the 2D device structure illustrated in Figure 8.1, under the assumption of a 50 Ohm series load resistance. In the third spatial dimension, device width has been scaled to 1mm for convenience. Numerical simulation reveals two distinct modes of self-sustaining millimeter-wave oscillation. The first mode is characterized by the nucleation of a dipole domain underneath the drain edge of the gate electrode, and its growth and propagation towards the drain electrode, the point of its ultimate collection. Figure 8.2 illustrates the spatial profiles of electron density and electric field strength at five representative instants of time during one cycle of operation for the case of a 2V gate-source bias and an average drain-source bias of approximately 50V. Strong oscillations at a rate of approximately 51 GHz are reflected in the load current waveform (see Figure 8.3), corresponding to a transit time of 19ps and an average dipole domain propagation speed of 1.75×10^7cm/s. At their peak, lateral electric fields within the 2D traveling domains exceed 1 MV/cm – over an order of magnitude larger

than the peak fields associated with bulk-like Gunn domains observed in conventional zincblende materials. As a consequence, charge transport within these traveling domains is fundamentally quasi-ballistic, and not directly related to the familiar stationary velocity-field profile of electrons in bulk material. Instead, the dipole domains observed in our simulations share many features in common with previously predicted instabilities induced by Bragg scattering [168], and are largely unrelated to the Gunn instabilities observed in traditional zincblende materials based on the mechanism of k-space transfer [153, 156].

A second mode of oscillation is observed at slightly lower average drain-source bias, in which the traveling dipole domains prematurely self-quench after traversing only a fraction of the channel length between gate and drain electrodes. The lower electric field strength in the domain indicates that this mode is similar to the bulk-like Gunn domains. However, the mismatch in the drift velocity between the wave-front and the trailing edge of the wave causes the domain to shrink until it completely disappears before reaching the drain electrode, as shown in Figure 8.4. As a consequence, the reduced transit distance enables faster oscillation, however, the premature quenching places limitations on the magnitude of oscillation. The corresponding load current waveform, depicted in Figure 8.5, exhibits sustained periodic oscillation at 154 GHz.

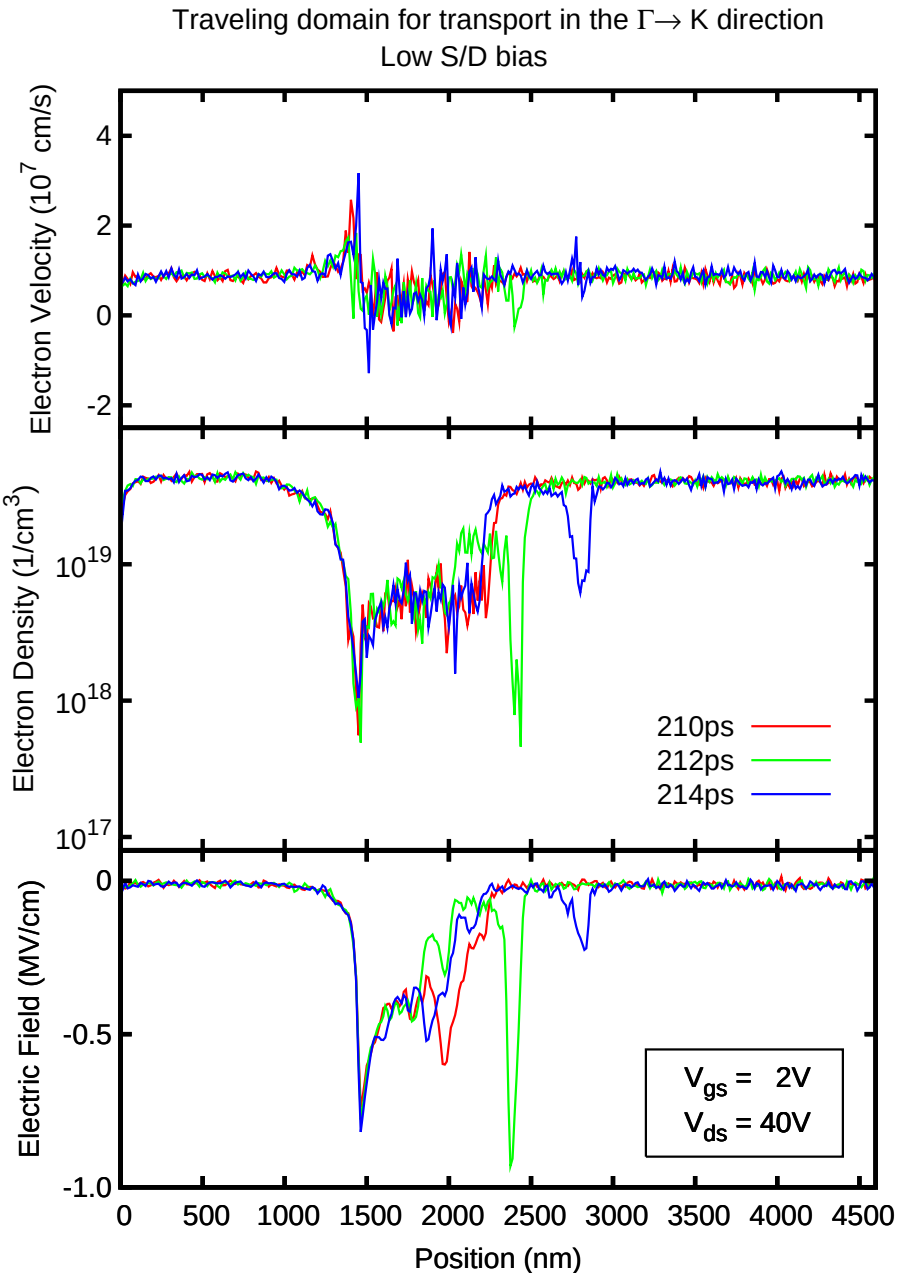

Figure 8.4: At low drain-source bias the dipole domain self-quenches prematurely.

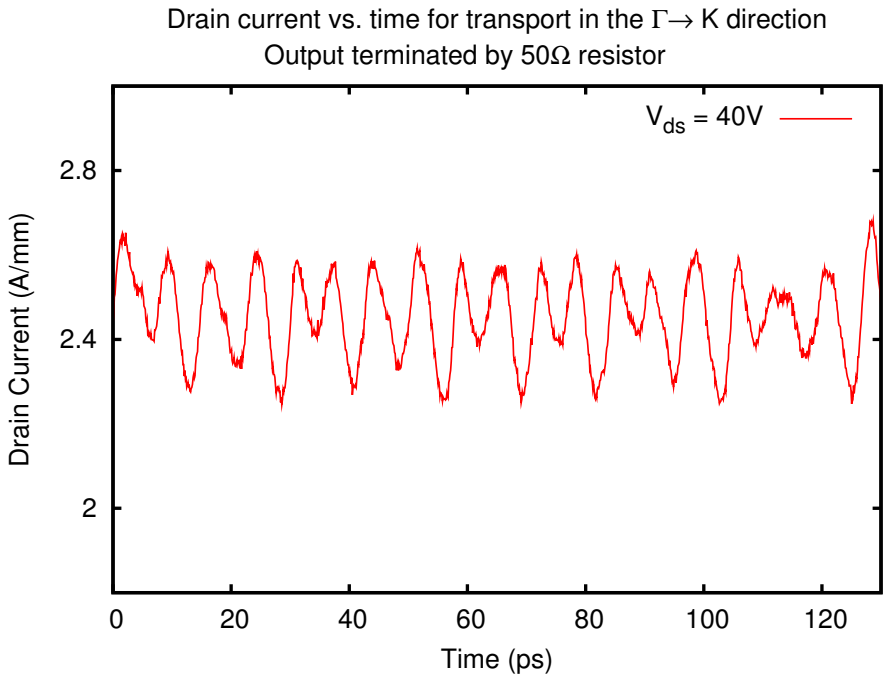

Figure 8.5: Low power load current oscillation at much higher frequency (154GHz) is observed at lower drain-source bias.

CHAPTER IX

CONCLUSION AND FUTURE RESEARCH DIRECTIONS

9.1 Conclusion

9.1.1 Simulation and calibration of transport in bulk GaN

The study of charge transport in bulk GaN using Monte Carlo simulation was presented in chapter 3. It was shown that both peak electron velocity and saturated electron velocity are higher for transport in the basal plane than along the *c*-axis, contrary to previously reported results [92]. Study of the transient electron velocity also showed a clear transit-time advantage for electron devices exploiting charge transport perpendicular to the *c*-axis. Chapter 3 also presented the temperature and doping dependence of electron mobility in GaN with transport parameters calibrated to experimental measurements. The Monte Carlo simulator enabled studies of transport under the influence of high free carrier densities but with low doping density, which is the mode of transport in AlGaN/GaN HEMTs. Theoretical studies of mobility under these conditions have not been previously reported in literature. These results provide valuable insight into transport phenomena to enable, for instance, the evaluation of mobility tradeoff between the free carrier density and the lattice temperature in the channel.

9.1.2 Isothermal study of charge transport in AlGaN/GaN HEMTs

The study of isothermal charge transport in AlGaN/GaN HEMTs using full-band ensemble Monte Carlo simulation was presented in chapter 4. Under high gate bias, simulations showed a droop in the drain current with increasing drain-source bias. Drain current droop in pulsed I-V measurements of AlGaN/GaN HEMTs has been previously reported [117]. The cause of the current droop in the absence of self-heating was investigated and was attributed to the presence of a lateral electric field spike in the channel at the drain edge of the gate. The field spike causes intervalley transfer of electrons to higher-energy valleys where group velocity is lower, leading to a drop in the drain current. Several

ways to minimize or eliminate the droop were considered. The use of a source- or gate-connected field plate was found to be effective in suppressing the magnitude of the field spike and designs with both types field plate were shown to eliminate the drain current droop. For X-band applications, gate capacitance becomes a primary concern and hence the source-connected field plate is preferred for maximum power-added efficiency.

9.1.3 Electrothermal study of charge transport in AlGaN/GaN HEMTs

High-power steady-state operation of GaN-based HEMTs is severely limited by self-heating effects [28, 29]. The influence of non-equilibrium acoustic and optical phonons on charge transport in AlGaN/GaN HEMTs was studied in chapter 5 using full-band ensemble Monte Carlo simulation. The direct emission of longitudinal optical (LO) phonons by hot electrons, their decay into acoustic phonons, and the subsequent transport of thermal energy away from the active region of the device by acoustic mode phonons were modeled by a system of rate equations and a two-dimensional lattice heat equation. It was found that, contrary to previous suggestions [28], the elevated acoustic mode temperature, rather than the direct influence of non-equilibrium LO phonon population, exerts the greater influence on the degradation of channel electron mobility over a broad range of applied bias.

9.1.4 Study of Geiger Mode Homojunction Avalanche Photodiodes

The Geiger mode operation of wurtzite GaN-based homojunction avalanche photodiodes (APDs) was investigated via full-band ensemble Monte Carlo charge transport simulation in chapter 6. The influence of dopant profile, active region thickness, and optical absorption profile on single photon detection efficiency (SPDE) were quantified. Simulations of linear mode gain as a function of multiplication region thickness and doping profile reveal that weakly n-type active regions may be exploited to achieve higher avalanche gain, without penalty to either applied bias or active region thickness. The study further demonstrated that the use of thicker multiplication regions leads to three distinct advantages for photon counting operations: 1) enhanced probability for photogenerated electron-hole pairs to trigger breakdown, 2) enhanced quantum efficiency due to the larger volume of depleted absorbing material, and 3) reduction of field-activated contributions to leakage current - all

without penalty to overbias ratio. Finally, it was shown through simulation that the growth rate of an avalanche pulse is a decreasing function of active region thickness, and derived an approximate analytic expression for the characteristic time constant, $[(\alpha + \beta)v]^{-1}$.

9.1.5 Study and Design of Heterojunction Avalanche Photodiodes

Chapter 7 explored the heterojunction APDs and provided valuable insight into their operation gained from full-band ensemble Monte Carlo simulation. A separate absorption and multiplication APD (SAM-APD) utilizing a AlGaN/GaN heterojunction was investigated. The presence of strong piezo-electric and spontaneous polarization charges at the heterojunction enabled favorable electric field profile in the device to reduce dark current, improve excess noise factor, improve quantum efficiency, and improve breakdown probability. With new insight into the different factors influencing APD performance, a new device structure with a buried absorber for maximizing SPDE was proposed. For the same overbias ratio, the SPDE of the new structure was calculated to be 64.7% compared to 54% for the homojunction APD. However, the new structure allows the device to be operated at much higher overbias ratios without depleting the absorber. A SPDE of 73% was demonstrated for a 500nm multiplier device operating at an overbias ratio of 0.58.

9.1.6 Study of Traveling Dipole Domains in AlGaN/GaN Heterostructures

A new approach for the direct generation of self-sustaining millimeter-wave oscillations was presented in chapter 8. In contrast to Gunn diodes, which exploit a bulk-like active region, periodic oscillation is achieved in the proposed structures through the creation, propagation and collection of traveling dipole domains supported by fixed polarization charge and the associated two-dimensional electron gas along the plane of a polar heterojunction. Full-band ensemble Monte Carlo simulations reveal two distinct modes of self-sustaining millimeter-wave oscillation, both nucleating underneath the drain edge of the gate electrode. The first mode is characterized by traveling dipole domains with fundamentally quasi-ballistic charge transport sharing many features in common with previously predicted instabilities induced by Bragg scattering [168], and largely unrelated to the Gunn instabilities observed in traditional zincblende materials. These domains grow

as they propagate towards the drain electrode, where they are collected.

The second mode of oscillation, observed at slightly lower drain-source bias, involves traveling dipole domains that prematurely self-quenches after traversing only a fraction of the channel length. Although the reduced transit time leads to faster oscillation, premature quenching limits the magnitude of oscillation.

9.2 Future research directions

9.2.1 Self-consistent electrothermal analysis of HEMTs

HEMTs used in continuous wave RF applications operate under large duty-cycles, where Joule heating plays a significant role, and severely degrades mobility, resulting in a significant drop in the drain current when compared to low duty-cycle, narrow pulse width mode of operation. Accurate modeling of the electrothermal transport under these conditions is essential for predicting device performance. In its present state, the full-band ensemble Monte Carlo simulator solves the two-dimensional lattice heat equation to calculate the acoustic mode temperature on an extended device grid. However, the computed lattice temperature is not readily usable to synchronously update the non-equilibrium phonon populations. Enhancing the lattice heat equation solver to allow synchronous update of the non-equilibrium phonon population at suitable time steps would enable self-consistent solution to the electrothermal model.

To maximize the power-added efficiency of these devices, the synchronous electrothermal model in conjunction with the full-band ensemble Monte Carlo simulator can be used to explore key design aspects that influence the performance of AlGaN/GaN HEMTs. These design considerations include gate-drain spacing, gate length, barrier thickness, aluminum mole fraction in the barrier, placement of electrical and thermal contacts, and other design features such as the addition of source or gate connected field plates.

Similar design considerations can be used to optimize dipole domains in triode structures to simultaneously achieve high-power and high-frequency millimeter-wave oscillations.

9.2.2 Design optimization of SAM-APDs

The buried absorber heterojunction SAM-APD structure proposed in this thesis demonstrated improvements in both optical quantum efficiency and breakdown probability yielding a SPDE of 73% for a 500nm multiplier device operating at an overbias ratio of 0.58. Using coupled electrothermal full-band ensemble Monte Carlo simulations, the design space of SAM-APD can be explored to further enhance the SPDE.

REFERENCES

[1] J. W. Johnson, E. L. Piner, A. Vescan, R. Therrien, P. Rajagopal, J. C. Roberts, J. D. Brown, S. Singhal, and K. J. Linthicum, "12 W/mm AlGaN-GaN HFETs on silicon substrates," *IEEE Electron Device Letters*, vol. 25, no. 7, pp. 459–61, 2004.

[2] T. Li, D. J. H. Lambert, A. L. Beck, C. J. Collins, B. Yang, M. M. Wong, U. Chowdhury, R. D. Dupuis, and J. C. Campbell, "Low-noise solar-blind AlxGa1-xN-based metal-semiconductor-metal ultraviolet photodetectors," *Journal of Electronic Materials*, vol. 30, no. 7, pp. 872–7, 2001.

[3] J. B. Limb, D. Yoo, J. H. Ryou, W. Lee, S. C. Shen, R. D. Dupuis, M. L. Reed, C. J. Collins, M. Wraback, D. Hanser, E. Preble, N. M. Williams, and K. Evans, "GaN ultraviolet avalanche photodiodes with optical gain greater than 1000 grown on GaN substrates by metal-organic chemical vapor deposition," *Applied Physics Letters*, vol. 89, no. 1, pp. 11 112–1, 2006.

[4] S. Verghese, K. A. McIntosh, R. J. Molnar, L. J. Mahoney, R. L. Aggarwal, M. W. Geis, K. M. Molvar, E. K. Duerr, and I. Melngailis, "GaN avalanche photodiodes operating in linear-gain mode and Geiger mode," *IEEE Transactions on Electron Devices*, vol. 48, no. 3, pp. 502–11, 2001.

[5] R. D. Dupuis, R. Jae-Hyun, S. Shyh-Chiang, P. D. Yoder, Z. Yun, K. Hee Jin, C. Suk, and Z. Lochner, "Growth and fabrication of high-performance GaN-based ultraviolet avalanche photodiodes," *Journal of Crystal Growth*, vol. 310, no. 23, pp. 5217–22, 2008.

[6] S. Nakamura and G. Farol, *The Blue Laser Diode*. Springer-Verlag, 1998.

[7] I. Akasaki and H. Amano, "Breakthroughs in improving crystal quality of GaN and invention of the p-n junction blue-light-emitting diode," *Japanese Journal of Applied Physics, Part 1 (Regular Papers, Short Notes & Review Papers)*, vol. 45, no. 12, pp. 9001–10, 2006.

[8] V. D. Jovanovic, Z. Ikonic, D. Indjin, P. Harrison, and R. A. Soref, "Designs for $\lambda = 1.55\mu$m GaN-based intersubband laser active region," *Japanese Journal of Applied Physics*, vol. 43, no. 11A, pp. 7444–7, 2004.

[9] S. Strite and H. Morkoc, "GaN, AlN, and InN: a review," *Journal of Vacuum Science & Technology B (Microelectronics Processing and Phenomena)*, vol. 10, no. Copyright 1992, IEE, pp. 1237–66, 1992.

[10] Q. Weida, M. Skowronski, and G. S. Rohrer, "Structural defects and their relationship to nucleation of GaN thin films," in *III-Nitride, SoC and Diamond Materials for Electronic Devices. Symposium, 8-12 April 1996*, ser. III-Nitride, SiC and Diamond Materials for Electronic Devices. Symposium. Mater. Res. Soc, 1996, pp. 475–86.

[11] S. N. Mohammed and H. Morkoc, "Progress and prospects of group-III nitride semiconductors," *Progress in Quantum Electronics*, vol. 20, no. 5-6, pp. 361–525, 1996.

[12] J. Burk, A. A., M. J. O'Loughlin, R. R. Siergiej, A. K. Agarwal, S. Sriram, R. C. Clarke, M. F. MacMillan, V. Balakrishna, and C. D. Brandt, "SiC and GaN wide bandgap semiconductor materials and devices," in *Topical Workshop on Heterostructure Microelectronics, 30 Aug.-2 Sept. 1998*, ser. Solid-State Electron. (UK), vol. 43. Elsevier, 1999, pp. 1459–64.

[13] M. Wraback, H. Shen, J. C. Carrano, C. J. Collins, J. C. Campbell, R. D. Dupuis, M. J. Schurman, and I. T. Ferguson, "Time-resolved electroabsorption measurement of the transient electron velocity overshoot in GaN," *Applied Physics Letters*, vol. 79, no. 9, pp. 1303–5, 2001.

[14] M. Wraback, H. Shen, J. C. Carrano, T. Li, and J. C. Campbell, "Measurement of transit time and carrier velocity under high electric field in III-nitride p-i-n diodes," in *Materials Research Society Symposium*, ser. Wide-Bandgap Electronic Devices. Symposium (Materials Research Society Symposium Proceedings Vol.622). Mater. Res. Soc, 2001, pp. 5–1.

[15] V. A. Dmitriev, K. G. Irvine, J. Carter, C. H., N. I. Kuznetsov, and E. V. Kalinina, "Electric breakdown in GaN p-n junctions," *Applied Physics Letters*, vol. 68, no. 2, pp. 229–31, 1996.

[16] N. Dyakonova, A. Dickens, M. S. Shur, and R. Gaska, "Impact ionisation in AlGaN-GaN heterostructure field effect transistors on sapphire substrates," *Electronics Letters*, vol. 34, no. 17, pp. 1699–700, 1998.

[17] X. A. Cao, M. Larsen, H. Lu, and S. D. Arthur, "Structural properties and electrical characteristics of homoepitaxial GaN PiN diodes," *Materials Science Forum*, vol. 527-529, pp. 1541–4, 2006.

[18] V. M. Asnin, F. H. Pollak, J. Ramer, M. Schurman, and I. Ferguson, "High spatial resolution thermal conductivity of lateral epitaxial overgrown GaN/sapphire (0001) using a scanning thermal microscope," *Applied Physics Letters*, vol. 75, no. 9, pp. 1240–2, 1999.

[19] D. Kotchetkov, J. Zou, and A. A. Balandin, "Theoretical investigation of thermal conductivity in wurtzite GaN," in *Materials Research Society Symposium*, ser. Modeling and Numerical Simulation of Materials Behavior and Evolution. Symposium (Materials Research Society Proceedings Vol.731). Mater. Res. Soc, 2002, pp. 135–40.

[20] F. Bernardini, V. Fiorentini, and D. Vanderbilt, "Spontaneous polarization and piezoelectric constants of III-V nitrides," *Physical Review B (Condensed Matter)*, vol. 56, no. 16, pp. 10 024–7, 1997.

[21] O. Ambacher, J. Smart, J. R. Shealy, N. G. Weimann, K. Chu, M. Murphy, W. J. Schaff, L. F. Eastman, R. Dimitrov, L. Wittmer, M. Stutzmann, W. Rieger, and J. Hilsenbeck, "Two-dimensional electron gases induced by spontaneous and piezoelectric polarization charges in N- and Ga-face AlGaN/GaN heterostructures," *Journal of Applied Physics*, vol. 85, no. 6, pp. 3222–33, 1999.

[22] K. Oe and Y. Imamura, "Two-dimensional electron gas at n-AlGaAs/GaAs interface grown by molecular-beam epitaxy using direct-radiation substrate heating," *Japanese*

Journal of Applied Physics, Part 1 (Regular Papers & Short Notes), vol. 24, no. 6, pp. 779–80, 1985.

[23] U. K. Mishra, P. Parikh, and W. Yi-Feng, "AlGaN/GaN HEMTs-an overview of device operation and applications," *Proceedings of the IEEE*, vol. 90, no. 6, pp. 1022–31, 2002.

[24] G. A. Slack, "Nonmetallic crystals with high thermal conductivity," *Journal of the Physics and Chemistry of Solids*, vol. 34, no. 2, pp. 321–35, 1973.

[25] Y. F. Wu, A. Saxler, M. Moore, R. P. Smith, S. Sheppard, P. M. Chavarkar, T. Wisleder, U. K. Mishra, and P. Parikh, "30-W/mm GaN HEMTs by field plate optimization," *IEEE Electron Device Letters*, vol. 25, no. 3, pp. 117–19, 2004.

[26] T. Palacios, A. Chakraborty, S. Rajan, C. Poblenz, S. Keller, S. P. DenBaars, J. S. Speck, and U. K. Mishra, "High-power AlGaN/GaN HEMTs for Ka-band applications," *IEEE Electron Device Letters*, vol. 26, no. 11, pp. 781–3, 2005.

[27] S. Shyh-Chiang, Z. Yun, Y. Dongwon, L. Jae-Boum, R. Jae-Hyun, P. D. Yoder, and R. D. Dupuis, "Performance of deep ultraviolet GaN avalanche photodiodes grown by MOCVD," *IEEE Photonics Technology Letters*, vol. 19, no. 21, pp. 1744–6, 2007.

[28] A. Matulionis, "Comparative analysis of hot-phonon effects in nitride and arsenide channels for HEMTs," in *Device Research Conference*, ser. Device Research Conference - Conference Digest, DRC. Institute of Electrical and Electronics Engineers Inc., 2004, pp. 145–146.

[29] ——, "Hot phonons in GaN channels for HEMTs," *Physica Status Solidi A*, vol. 203, no. 10, pp. 2313–25, 2006.

[30] B. Gelmont, K. Kim, and M. Shur, "Monte Carlo simulation of electron transport in gallium nitride," *Journal of Applied Physics*, vol. 74, no. 3, pp. 1818–21, 1993.

[31] J. Kolnik, I. H. Oguzman, K. F. Brennan, W. Rongping, P. P. Ruden, and W. Yang, "Electronic transport studies of bulk zincblende and wurtzite phases of GaN based

on an ensemble Monte Carlo calculation including a full zone band structure," *Journal of Applied Physics*, vol. 78, no. 2, pp. 1033–8, 1995.

[32] N. S. Mansour, K. W. Kim, and M. A. Littlejohn, "Theoretical study of electron transport in gallium nitride," *Journal of Applied Physics*, vol. 77, no. 6, pp. 2834–6, 1995.

[33] J. D. Albrecht, R. P. Wang, P. P. Ruden, M. Farahmand, and K. F. Brennan, "Electron transport characteristics of GaN for high temperature device modeling," *Journal of Applied Physics*, vol. 83, no. 9, pp. 4777–81, 1998.

[34] M. Saraniti and S. M. Goodnick, "A full-band cellular automaton for charge transport simulation in semiconductors," in *Sixth International Workshop on Computational Electronics*, ser. 1998 Sixth International Workshop on Computational Electronics. Extended Abstracts (Cat. No.98EX116). IEEE, 1998, pp. 88–91.

[35] ——, "Hybrid fullband cellular automaton/Monte Carlo approach for fast simulation of charge transport in semiconductors," *IEEE Transactions on Electron Devices*, vol. 47, no. 10, pp. 1909–16, 2000.

[36] J. Y. Tang and K. Hess, "Investigation of transient electronic transport in GaAs following high energy injection," *IEEE Transactions on Electron Devices*, vol. ED-29, no. 12, pp. 1906–11, 1982.

[37] C. Jacoboni and L. Reggiani, "The Monte Carlo method for the solution of charge transport in semiconductors with applications to covalent materials," *Reviews of Modern Physics*, vol. 55, no. 3, pp. 645–705, 1983.

[38] K. Brennan and K. Hess, "High field transport in GaAs, InP and InAs," *Solid-State Electronics*, vol. 27, no. 4, pp. 347–57, 1984.

[39] T. Wang and K. Hess, "Calculation of the electron velocity distribution in high electron mobility transistors using an ensemble Monte Carlo method," *Journal of Applied Physics*, vol. 57, no. 12, pp. 5336–9, 1985.

[40] C. Moglestue, "A self-consistent Monte Carlo particle model to analyse semiconductor microcomponents of any geometry," *IEEE Transactions on Computer-Aided Design of Integrated Circuits and Systems*, vol. CAD-5, no. 2, pp. 326–45, 1986.

[41] U. Ravaioli and D. K. Ferry, "MODFET ensemble Monte Carlo model including the quasi-two-dimensional electron gas," *IEEE Transactions on Electron Devices*, vol. ED-33, no. 5, pp. 677–81, 1986.

[42] M. V. Fischetti and S. E. Laux, "Monte Carlo analysis of electron transport in small semiconductor devices including band-structure and space-charge effects," *Physical Review B (Condensed Matter)*, vol. 38, no. 14, pp. 9721–45, 1988.

[43] S. E. Laux, M. V. Fischetti, and D. J. Frank, "Monte Carlo analysis of semiconductor devices. The DAMOCLES program," *IBM Journal of Research and Development*, vol. 34, no. 4, pp. 466–494, 1990.

[44] T. Kurosawa, "Monte carlo calculation of hot electron problems," in *International Conference on the Physics of Semiconductors*, vol. 21, 1966, pp. 424–426.

[45] A. D. Boardman, W. Fawcett, and H. D. Rees, "Monte Carlo calculation of the velocity-field relationship for gallium arsenide," *Solid State Communications*, vol. 6, no. 5, pp. 305–307, 1968.

[46] W. Fawcett, C. Hilsum, and H. D. Rees, "Effects of non-parabolicity on non-ohmic transport in InAs," *Solid State Communications*, vol. 7, no. 17, pp. 1257–9, 1969.

[47] H. D. Rees, "The numerical analysis of semiclassical transport problems," *Journal of Physics C (Solid State Physics)*, vol. 3, no. 5, pp. 965–74, 1970.

[48] P. A. Lebwohl and P. J. Price, "Direct microscopic simulation of Gunn-domain phenomena," *Applied Physics Letters*, vol. 19, no. 12, pp. 530–2, 1971.

[49] N. W. Ashcroft and N. D. Mermin, *Solid State Physics*. Brooks/Cole, 1976.

[50] K. Hess, *Advanced Theory of Semiconductor Devices*. IEEE Press, 2000, ch. 7, pp. 94–96.

[51] A. de Mari, "An accurate numerical one-dimensional solution of the p-n junction under arbitrary transient conditions," *Solid-State Electronics*, vol. 11, no. 11, pp. 1021–53, 1968.

[52] ——, "An accurate numerical steady-state one-dimensional solution of the p-n junction," *Solid-State Electronics*, vol. 11, no. 1, pp. 33–58, 1968.

[53] E. M. Buturla and P. E. Cottrell, "Simulation of semiconductor transport using coupled and decoupled solution techniques," *Solid-State Electronics*, vol. 23, no. 4, pp. 331–4, 1980.

[54] H. D. Rees, "Calculation of steady state distribution functions by exploiting stability," *Physics Letters*, vol. 26A, no. 9, pp. 416–417, 1968.

[55] H. Shichijo and K. Hess, "Band-structure-dependent transport and impact ionization in GaAs," *Physical Review B (Condensed Matter)*, vol. 23, no. 8, pp. 4197–207, 1981.

[56] J. Y. Tang and K. Hess, "Impact ionization of electrons in silicon (steady state)," *Journal of Applied Physics*, vol. 54, no. 9, pp. 5139–44, 1983.

[57] J. M. Ziman, *Electrons and Phonons*. Oxford University Press, 1974.

[58] L. V. Keldysh, "Theory of impact ionization in semiconductors," *Zhurnal Eksperimental'noi i Teoreticheskoi Fiziki*, vol. 48, no. 6, pp. 1692–1707, 1965.

[59] E. O. Kane, "Electron scattering by pair production in silicon," *Physical Review*, vol. 159, no. 3, pp. 624–631, 1967.

[60] P. Conti, N. Hitschfeld, and W. Fichtner, "-an octree-based mixed element grid allocator for the simulation of complex 3-D device structures," *IEEE Transactions on Computer-Aided Design of Integrated Circuits and Systems*, vol. 10, no. 10, pp. 1231–41, 1991.

[61] N. Hitschfeld, P. Conti, and W. Fichtner, "Mixed element trees: a generalization

of modified octrees for the generation of meshes for the simulation of complex 3-D semiconductor device structures," *IEEE Transactions on Computer-Aided Design of Integrated Circuits and Systems*, vol. 12, no. 11, pp. 1714–25, 1993.

[62] T. Chen, D. W. Yergeau, and R. W. Dutton, "Efficient 3D mesh adaptation in diffusion simulation," in *Proceedings of International Conference on Simulation of Semiconductor Processes and Devices, 2-4 Sept. 1996*, ser. 1996 International Conference on Simulation of Semiconductor Processes and Devices. SISPAD '96 (IEEE Cat. No.96TH8095). Japan Soc. Appl. Phys, 1996, pp. 171–2.

[63] G. Garreton, L. Villablanca, N. Strecker, and W. Fichtner, "A new approach for 2-D mesh generation for complex device structures," in *Proceedings of International Workshop on Numerical Modeling of processes and Devices for Integrated Circuits: NUPAD V, 5-6 June 1994*, ser. International Workshop on Numerical Modeling of Processes and Devices for Integrated Circuits. NUPAD V (Cat. No.94TH0640-3). IEEE, 1994, pp. 159–62.

[64] J. Krause, N. Strecker, and W. Fichtner, "Boundary-sensitive mesh generation using an offsetting technique [and semiconductor device/process simulation application]," *International Journal for Numerical Methods in Engineering*, vol. 49, no. 1-2, pp. 51–9, 2000.

[65] R. Klima, "Three-Dimensional Device Simulation with Minimos-NT," PhD Thesis, Vienna University of Technology, 2002.

[66] S. Hang. (2005) A Quality Tetrahedral Mesh Generator and a 3D Delaunay Triangulator. [Online]. Available: http://www.tetgen.org

[67] S. Bloom, G. Harbeke, E. Meier, and I. B. Ortenburger, "Band structure and reflectivity of GaN," *Physica Status Solidi B*, vol. 66, no. 1, pp. 161–8, 1974.

[68] A. Rubio, J. L. Corkill, M. L. Cohen, E. L. Shirley, and S. G. Louie, "Quasiparticle bond structure of AlN and GaN," *Physical Review B (Condensed Matter)*, vol. 48, no. 16, pp. 11 810–16, 1993.

[69] M. Suzuki, T. Uenoyama, and A. Yanase, "First-principles calculations of effective-mass parameters of AlN and GaN," *Physical Review B (Condensed Matter)*, vol. 52, no. 11, pp. 8132–9, 1995.

[70] Y. C. Yeo, T. C. Chong, and M. F. Li, "Electronic band structures and effective-mass parameters of wurtzite GaN and InN," *Journal of Applied Physics*, vol. 83, no. 3, pp. 1429–36, 1998.

[71] E. Bellotti, B. K. Doshi, K. F. Brennan, J. D. Albrecht, and P. P. Ruden, "Ensemble Monte Carlo study of electron transport in wurtzite InN," *Journal of Applied Physics*, vol. 85, no. 2, pp. 916–23, 1999.

[72] B. K. Ridley, *Quantum Processes in Semiconductors*, 4th ed. Oxford University Press, 1999, ch. 4, pp. 138–183.

[73] D. K. Cheng, *Field and Wave Electromagnetics*. Pearson Education, 1989.

[74] J. M. Wagner and F. Bechstedt, "Phonon deformation potentials of α-GaN and -AlN: An ab initio calculation," *Applied Physics Letters*, vol. 77, no. 3, pp. 346–8, 2000.

[75] K. F. Brennan, E. Bellotti, M. Farahmand, H. E. Nilsson, P. P. Ruden, and Y. Zhang, "Monte Carlo modeling of wurtzite and 4H phase semiconducting materials," in *Seventh International Workshop on Computational Electronics (IWCE-7), 22-25 May 2000*, ser. VLSI Des. (Netherlands), vol. 13. Gordon & Breach, 2001, pp. 117–24.

[76] K. F. Brennan, *The Physics of Semiconductors: with applications to optoelectronic devices*. Cambridge University Press, 1999.

[77] B. C. Lee, K. W. Kim, M. Dutta, and M. A. Stroscio, "Electron-optical-phonon scattering in wurtzite crystals," *Physical Review B (Condensed Matter)*, vol. 56, no. 3, pp. 997–1000, 1997.

[78] C. Bulutay, B. K. Ridley, and N. A. Zakhleniuk, "Full-band polar optical phonon scattering analysis and negative differential conductivity in wurtzite GaN," *Physical Review B (Condensed Matter)*, vol. 62, no. 23, pp. 15 754–63, 2000.

[79] R. Loudon, "The Raman effect in crystals," *Advances in Physics*, vol. 13, pp. 423–482, 1964.

[80] K. W. Kim and M. A. Stroscio, "Electron-optical-phonon interaction in binary/ternary heterostructures," *Journal of Applied Physics*, vol. 68, no. 12, pp. 6289–92, 1990.

[81] T. Azuhata, T. Sota, K. Suzuki, and S. Nakamura, "Polarized Raman spectra in GaN," *Journal of Physics: Condensed Matter*, vol. 7, no. 10, pp. 129–33, 1995.

[82] P. W. Rambo and J. Denavit, "Time stability of Monte Carlo device simulation," *IEEE Transactions on Computer-Aided Design of Integrated Circuits and Systems*, vol. 12, no. 11, pp. 1734–41, 1993.

[83] E. Cuthill and J. McKee, "Reducing the bandwidth of sparse symmetric matrices," in *Proceedings of the 1969 24th national conference*. 805928: ACM, 1969, pp. 157–172.

[84] A. George, "Computer Implementation of the Finite Element Method," PhD Thesis, Stanford University, 1971.

[85] S. E. Laux, "On particle-mesh coupling in Monte Carlo semiconductor device simulation," *IEEE Transactions on Computer-Aided Design of Integrated Circuits and Systems*, vol. 15, no. 10, pp. 1266–77, 1996.

[86] P. D. Yoder, K. Gartner, and W. Fichtner, "A generalized Ramo-Shockley theorem for classical to quantum transport at arbitrary frequencies," *Journal of Applied Physics*, vol. 79, no. 4, pp. 1951–4, 1996.

[87] V. W. L. Chin, T. L. Tansley, and T. Osotchan, "Electron mobilities in gallium, indium, and aluminum nitrides," *Journal of Applied Physics*, vol. 75, no. 11, pp. 7365–72, 1994.

[88] W. Gotz, N. M. Johnson, C. Chen, H. Liu, C. Kuo, and W. Imler, "Activation energies of Si donors in GaN," *Applied Physics Letters*, vol. 68, no. 22, pp. 3144–6, 1996.

[89] I. H. Oguzman, J. Kolnik, K. F. Brennan, W. Rongping, F. Tzu-Ning, and P. P. Ruden, "Hole transport properties of bulk zinc-blende and wurtzite phases of GaN based on

an ensemble Monte Carlo calculation including a full zone band structure," *Journal of Applied Physics*, vol. 80, no. 8, pp. 4429–36, 1996.

[90] B. E. Foutz, S. K. O'Leary, M. S. Shur, and L. F. Eastman, "Transient electron transport in wurtzite GaN, InN, and AlN," *Journal of Applied Physics*, vol. 85, no. 11, pp. 7727–34, 1999.

[91] M. Wraback, H. Shen, S. Rudin, and E. Bellotti, "Experimental and theoretical studies of transient electron velocity overshoot in GaN," *Physica Status Solidi B*, vol. 234, no. 3, pp. 810–16, 2002.

[92] M. Wraback, H. Shen, S. Rudin, E. Bellotti, M. Goano, J. C. Carrano, C. J. Collins, J. C. Campbell, and R. D. Dupuis, "Direction-dependent band nonparabolicity effects on high-field transient electron transport in GaN," *Applied Physics Letters*, vol. 82, no. 21, pp. 3674–6, 2003.

[93] S. K. O'Leary, B. E. Foutz, M. S. Shur, and L. F. Eastman, "Steady-state and transient electron transport within the III-V nitride semiconductors, GaN, AlN, and InN: a review," *Journal of Materials Science: Materials in Electronics*, vol. 17, no. 2, pp. 87–126, 2006.

[94] J. M. Barker, R. Akis, D. K. Ferry, S. M. Goodnick, T. J. Thornton, D. D. Koleske, A. E. Wickenden, and R. L. Henry, "High-field transport studies of GaN," in *Twelfth International Conference on Nonequilibriaum Carrier Dynamics in Semiconductors.*, ser. Physica B (Netherlands), vol. 314. Elsevier, 2001, pp. 39–41.

[95] M. Goano, E. Bellotti, E. Ghillino, G. Ghione, and K. F. Brennan, "Band structure nonlocal pseudopotential calculation of the III-nitride wurtzite phase materials system. Part I. Binary compounds GaN, AlN, and InN," *Journal of Applied Physics*, vol. 88, no. 11, pp. 6467–75, 2000.

[96] S. Sridharan, A. Venkatachalam, and P. D. Yoder, "Electrothermal analysis of AlGaN/GaN high electron mobility transistors," *Journal of Computational Electronics*, vol. 7, no. 3, pp. 236–239, 2008.

[97] Y. Oshima, T. Yoshida, T. Eri, M. Shibata, and T. Mishima, "Thermal and electrical properties of high-quality freestanding GaN wafers with high carrier concentration," *Japanese Journal of Applied Physics, Part 1 (Regular Papers, Short Notes & Review Papers)*, vol. 45, no. 10A, pp. 7685–7, 2006.

[98] H. Witte, A. Krtschil, E. Schrenk, K. Fluegge, A. Dadgar, and A. Krost, "Correlation between macroscopic transport parameters and microscopic electrical properties in GaN," *Journal of Applied Physics*, vol. 97, no. 4, pp. 43 710–14, 2005.

[99] Y. Fu, M. Willander, Z. F. Li, and W. Lu, "Electron mobilities, Hall factors, and scattering processes of n-type GaN epilayers studied by infrared reflection and Hall measurements," *Physical Review B (Condensed Matter and Materials Physics)*, vol. 67, no. 11, pp. 113 313–1, 2003.

[100] S. Sridharan and P. D. Yoder, "Anisotropic transient and stationary electron velocity in bulk wurtzite GaN," *IEEE Electron Device Letters*, vol. 29, no. 11, pp. 1190–2, 2008.

[101] A. Dyson and B. K. Ridley, "Phonon-plasmon coupled-mode lifetime in semiconductors," *Journal of Applied Physics*, vol. 103, no. 11, pp. 114 507–1, 2008.

[102] T. Beechem and S. Graham, "Temperature and doping dependence of phonon lifetimes and decay pathways in GaN," *Journal of Applied Physics*, vol. 103, no. 9, pp. 093 507–1, 2008.

[103] T. Palacios, L. Shen, S. Keller, A. Chakraborty, S. Heikman, S. P. DenBaars, U. K. Mishra, J. Liberis, O. Kiprijanovic, and A. Matulionis, "Nitride-based high electron mobility transistors with a GaN spacer," *Applied Physics Letters*, vol. 89, no. 7, pp. 73 508–1, 2006.

[104] D. Huang, F. Yun, M. A. Reshchikov, D. Wang, H. Morkoc, D. L. Rode, L. A. Farina, C. Kurdak, K. T. Tsen, S. S. Park, and K. Y. Lee, "Hall mobility and carrier concentration in free-standing high quality GaN templates grown by hydride vapor phase epitaxy," *Solid-State Electronics*, vol. 45, no. 5, pp. 711–15, 2001.

[105] T. D. Moustakas, E. Iliopoulos, A. V. Sampath, H. M. Ng, D. Doppalapudi, M. Misra, D. Korakakis, and R. Singh, "Growth and device applications of III-nitrides by MBE," ser. J. Cryst. Growth (Netherlands), vol. 227-228. Elsevier, 2001, pp. 13–20.

[106] F. Bertazzi, M. Moresco, and E. Bellotti, "Theory of high field carrier transport and impact ionization in wurtzite GaN. Part I: a full band Monte Carlo model," *Journal of Applied Physics*, vol. 106, no. Copyright 2009, The Institution of Engineering and Technology, p. 063718 (12 pp.), 2009.

[107] A. Conway, J. Li, and P. Asbeck, "Effects of gate recess depth on pulsed I-V characteristics of AlGaN/GaN HFETs," ser. 2003 International Semiconductor Device Research Symposium (IEEE Cat. No.03EX741). IEEE, 2003, pp. 439–40.

[108] S. Yamakawa, M. Saraniti, and S. M. Goodnick, "High field transport in GaN and AlGaN/GaN heterojunctions," in *Proc. SPIE - Int. Soc. Opt. Eng. (USA)*, ser. Proc. SPIE - Int. Soc. Opt. Eng. (USA), vol. 6471. SPIE - The International Society for Optical Engineering, 2007, pp. 64 710–1.

[109] R. Gaska, A. Osinsky, J. W. Yang, and M. S. Shur, "Self-heating in high-power AlGaN-GaN HFET's," *IEEE Electron Device Letters*, vol. 19, no. 3, pp. 89–91, 1998.

[110] T. Sadi, R. W. Kelsall, and N. J. Pilgrim, "Investigation of self-heating effects in submicrometer GaN/AlGaN HEMTs using an electrothermal Monte Carlo method," *IEEE Transactions on Electron Devices*, vol. 53, no. 12, p. 9 pp., 2006.

[111] Y. Tomita, H. Ikegami, and H. I. Fujishiro, "Monte Carlo study of high-field electron transport characteristics in AlGaN/GaN heterostructure considering dislocation scattering," in *Physica Status Solidi (C) Current Topics in Solid State Physics*, ser. Physica Status Solidi (C) Current Topics in Solid State Physics, vol. 4. Wiley-VCH Verlag, Weinheim, D-69451, Germany, 2007, pp. 2695–2699.

[112] T. Sadi, R. W. Kelsall, and N. J. Pilgrim, "Electrothermal Monte Carlo simulation of submicron wurtzite GaN/AlGaN HEMTs," *Journal of Computational Electronics*, vol. 6, no. 1, pp. 35–39, 2007.

[113] F. van Raay, R. Quay, R. Kiefer, F. Benkhelifa, B. Raynor, W. Pletschen, M. Kuri, H. Massler, S. Muller, M. Dammann, M. Mikulla, M. Schlechtweg, and G. Weimann, "A coplanar X-band AlGaN/GaN power amplifier MMIC on s.i. SiC substrate," *IEEE Microwave and Wireless Components Letters*, vol. 15, no. 7, pp. 460–2, 2005.

[114] D. S. A. Sahinkaya, A. S. Turk, B. Sen, and S. A. Bechteler, "An innovative GPR system design: Detection of cylindrical dielectric objects," in *Proceedings of the Tenth International Conference Ground Penetrating Radar*, ser. Proceedings of the Tenth International Conference Ground Penetrating Radar, GPR 2004, vol. 1. Institute of Electrical and Electronics Engineers Inc., 2004, pp. 191–194.

[115] Y. Kawano, Y. Nakasha, K. Yokoo, S. Masuda, T. Takahashi, T. Hirose, Y. Oishi, and K. Hamaguchi, "RF chipset for impulse UWB Radar using 0.13-μm InP-HEMT technology," *IEEE Transactions on Microwave Theory and Techniques*, vol. 54, no. 12, pp. 4489–97, 2006.

[116] N. Deparis, C. Loyez, N. Rolland, and P. A. Rolland, "UWB in millimeter wave band with pulsed ILO," *IEEE Transactions on Circuits and Systems-II: Analog and Digital Signal Processing*, vol. 55, no. 4, pp. 339–43, 2008.

[117] W. Nagy, J. Brown, R. Borges, and S. Singhal, "Linearity characteristics of microwave-power GaN HEMTs," *IEEE Transactions on Microwave Theory and Techniques*, vol. 51, no. 2, pp. 660–4, 2003.

[118] W. Saito, Y. Takada, M. Kuraguchi, K. Tsuda, I. Omura, T. Ogura, and H. Ohashi, "High breakdown voltage AlGaN-GaN power-HEMT design and high current density switching behavior," *IEEE Transactions on Electron Devices*, vol. 50, no. 12, pp. 2528–31, 2003.

[119] E. Pop, R. Dutton, and K. Goodson, "Detailed heat generation simulations via the Monte Carlo method," ser. 2003 IEEE International Conference on Simulation of Semiconductor Processes and Devices (Cat. No.03TH8679). IEEE, 2003, pp. 121–4.

[120] W. Batty, C. E. Christoffersen, A. J. Panks, S. David, C. M. Snowden, and M. B. Steer, "Electrothermal CAD of power devices and circuits with fully physical time-dependent compact thermal modeling of complex nonlinear 3-D systems," *IEEE Transactions on Components and Packaging Technologies*, vol. 24, no. 4, pp. 566–590, 2001.

[121] T. Sadi and R. W. Kelsall, "Hot-phonon effect on the electrothermal behavior of submicrometer III-V HEMTs," *IEEE Electron Device Letters*, vol. 28, no. 9, pp. 787–9, 2007.

[122] ——, "Theoretical study of electron confinement in submicrometer GaN HFETs using a thermally self-consistent Monte Carlo method," *IEEE Transactions on Electron Devices*, vol. 55, no. 4, pp. 945–953, 2008.

[123] J. C. Campbell, S. Demiguel, M. Feng, A. Beck, G. Xiangyi, W. Shuling, Z. Xiaoguang, L. Xiaowei, J. D. Beck, M. A. Kinch, A. Huntington, L. A. Coldren, J. Decobert, and N. Tscherptner, "Recent advances in avalanche photodiodes," *IEEE Journal of Selected Topics in Quantum Electronics*, vol. 10, no. 4, pp. 777–87, 2004.

[124] M. A. Albota, B. F. Aull, D. G. Fouche, R. M. Heinrichs, D. G. Kocher, R. M. Marino, J. G. Mooney, N. R. Newbury, M. E. O'Brien, B. E. Player, B. C. Willard, and J. J. Zayhowski, "Three-dimensional imaging laser radars with Geiger-mode avalanche photodiode arrays," *Lincoln Laboratory Journal*, vol. 13, no. 2, pp. 351–70, 2002.

[125] P. Clowes, S. McCallum, and A. Welch, "Development of a Monte Carlo simulation for APD-based PET detectors using a continuous scintillating crystal," *IEEE Transactions on Nuclear Science*, vol. 53, no. 5, pp. 2563–9, 2006.

[126] J. Cabalo, M. DeLucia, A. Goad, J. Lacis, F. Narayanan, and D. Sickenberger, "Overview of the TAC-BIO detector," ser. Proc. SPIE - Int. Soc. Opt. Eng. (USA), vol. 7116. SPIE - The International Society for Optical Engineering, 2008, p. 71160D (11 pp.).

[127] G. Xiangyi, L. B. Rowland, G. T. Dunne, J. A. Fronheiser, P. M. Sandvik, A. L. Beck, and J. C. Campbell, "Demonstration of ultraviolet separate absorption and multiplication 4H-SiC avalanche photodiodes," *IEEE Photonics Technology Letters*, vol. 18, no. 1, pp. 136–8, 2006.

[128] R. J. McIntyre, "Multiplication noise in uniform avalanche diodes," *IEEE Transactions on Electron Devices*, vol. ED-13, no. 1, pp. 164–168, 1966.

[129] R. McIntyre, "The Distribution of Gains in Uniformly Multiplying Avalanche Photodiodes: Theory," *IEEE Transactions on Electron Devices*, vol. ED-19, no. 6, pp. 703–713, 1972.

[130] R. J. McIntyre, "A new look at impact ionization-Part I: A theory of gain, noise, breakdown probability, and frequency response," *IEEE Transactions on Electron Devices*, vol. 46, no. 8, pp. 1623–31, 1999.

[131] W. G. Oldham, R. R. Samuelson, and P. Antognetti, "Triggering phenomena in avalanche diodes," *IEEE Transactions on Electron Devices*, vol. ED-19, no. 9, pp. 1056–1060, 1972.

[132] R. J. McIntyre, "On the avalanche initiation probability of avalanche diodes above the breakdown voltage," *IEEE Transactions on Electron Devices*, vol. ED20, no. 7, pp. 637–41, 1973.

[133] V. Chandramouli, C. M. Maziar, and J. C. Campbell, "Monte Carlo simulation of the effect of multiplication layer thickness in wide-bandwidth avalanche photodiodes," ser. IEEE Trans. Electron Devices (USA), vol. 40, 1993, p. 2137.

[134] ——, "Design considerations for high performance avalanche photodiode multiplication layers," *IEEE Transactions on Electron Devices*, vol. 41, no. 5, pp. 648–54, 1994.

[135] W. Yu-Jen and N. Goldsman, "Deterministic modeling of impact ionization with a random-k approximation and the multiband Boltzmann equation," *Journal of Applied Physics*, vol. 78, no. 8, pp. 5174–6, 1995.

[136] A. Spinelli and A. L. Lacaita, "Physics and numerical simulation of single photon avalanche diodes," *IEEE Transactions on Electron Devices*, vol. 44, no. 11, pp. 1931–43, 1997.

[137] C. H. Tan, J. P. R. David, J. Clark, G. J. Rees, S. A. Plimmer, D. J. Robbins, D. C. Herbert, R. T. Carline, and W. Y. Leong, "Avalanche multiplication and noise in submicron Si p-i-n diodes," ser. Proc. SPIE - Int. Soc. Opt. Eng. (USA), vol. 3953. SPIE-Int. Soc. Opt. Eng, 2000, pp. 95–102.

[138] B. K. Ng, J. P. R. David, C. H. Tan, S. A. Plimmer, G. J. Rees, R. C. Tozer, and M. Hopkinson, "Avalanche multiplication noise in bulk and thin AlGaAs (x=0-0.8) PIN and NIP diodes," ser. Proc. SPIE - Int. Soc. Opt. Eng. (USA), vol. 4288. SPIE-Int. Soc. Opt. Eng, 2001, pp. 39–46.

[139] B. K. Ng, J. S. Ng, P. J. Hambleton, J. P. R. David, D. S. Ong, G. J. Rees, and R. C. Tozer, "Design considerations for high-speed low-noise avalanche photodiodes," ser. Proc. SPIE - Int. Soc. Opt. Eng. (USA), vol. 4594. SPIE-Int. Soc. Opt. Eng, 2001, pp. 1–9.

[140] J. P. R. David, C. H. Tan, S. A. Plimmer, G. J. Rees, R. C. Tozer, and P. N. Robson, "Design of low-noise avalanche photodiodes," ser. Proc. SPIE - Int. Soc. Opt. Eng. (USA), vol. 3950. SPIE-Int. Soc. Opt. Eng, 2000, pp. 30–8.

[141] J. S. Ng, C. H. Tan, B. K. Ng, P. J. Hambleton, J. P. R. David, G. J. Rees, A. H. You, and D. S. Ong, "Effect of dead space on avalanche speed [APDs]," *IEEE Transactions on Electron Devices*, vol. 49, no. 4, pp. 544–9, 2002.

[142] J. S. Ng, C. H. Tan, G. J. Rees, and J. P. R. David, "Effects of dead space on breakdown probability in Geiger mode avalanche photodiode," *Journal of Modern Optics*, vol. 54, no. 2-3, pp. 353–60, 2007.

[143] D. S. Ong, K. F. Li, G. J. Rees, G. M. Dunn, J. P. R. David, and P. N. Robson, "A Monte Carlo investigation of multiplication noise in thin p+-i-n+ GaAs avalanche photodiodes," *IEEE Transactions on Electron Devices*, vol. 45, no. 8, pp. 1804–10, 1998.

[144] C. H. Tan, J. S. Ng, G. J. Rees, and J. P. R. David, "Statistics of avalanche current buildup time in single-photon avalanche diodes," *IEEE Journal on Selected Topics in Quantum Electronics*, vol. 13, no. 4, pp. 906–910, 2007.

[145] J. Carroll, *Hot electron microwave generators*. Edward Arnold, 1970.

[146] P. Bulman, G. Hobson, and B. Taylor, *Transferred electron devices*. Academic Press, 1972.

[147] G. Hobson, *The Gunn effect*. Clarendon Press, 1974.

[148] B. Bosch and R. Engelmann, *Gunn-effect electronics*. Wiley, 1975.

[149] H. Thim, *Microwave sources*. North-Holland, 1981, pp. 425–79.

[150] P. H. Siegel, "Terahertz technology," *IEEE Transactions on Microwave Theory and Techniques*, vol. 50, no. 3, pp. 910–28, 2002.

[151] S. I. Domrachev, S. A. Alaverdjan, and V. N. Skorokhodov, "Application of a Gunn-diode current-pulse generator for modulation of semiconductor lasers," *Technical Physics*, vol. 44, no. 5, pp. 544–7, 1999.

[152] N. Kukutsu and Y. Kado, "Overview of Millimeter and Terahertz Wave Application Research," *NTT Technical Review*, vol. 7, no. 3, p. 6 pp., 2009.

[153] C. Hilsum, "Transferred electron amplifiers and oscillators," *Proceedings of the Institute of Radio Engineers*, vol. 50, no. 2, pp. 185–189, 1962.

[154] B. K. Ridley and R. G. Pratt, "A bulk differential negative resistance due to electron tunnelling through an impurity potential barrier," *Physics Letters*, vol. 4, no. 5, pp. 300–302, 1963.

[155] R. H. Rediker and A. L. McWhorter, "Compound cryosars for low-temperature computer memories," *Solid-State Electronics*, vol. 2, no. 2-3, pp. 100–105, 1961.

[156] B. K. Ridley and T. B. Watkins, "The possibility of negative resistance effects in semiconductors," *Proceedings of the Physical Society*, vol. 78, pp. 293–304, 1961.

[157] S. Sze and K. Ng, *Physics of semiconductor devices*. Wiley-Interscience, 2007.

[158] S. Adachi, *Physical Properties of III-V Seminconductor Compounds*. New York: John Wiley and Sons, 1992.

[159] E. Alekseev and D. Pavlidis, "Large-signal microwave performance of GaN-based NDR diode oscillators," *Solid-State Electronics*, vol. 44, no. 6, pp. 941–7, 2000.

[160] M. A. Littlejohn, J. R. Hauser, and T. H. Glisson, "Monte Carlo calculation of the velocity-field relationship for gallium nitride," *Applied Physics Letters*, vol. 26, no. 11, pp. 625–7, 1975.

[161] Z. C. Huang, R. Goldberg, J. C. Chen, Z. Youdou, D. B. Mott, and P. Shu, "Direct observation of transferred-electron effect in GaN," *Applied Physics Letters*, vol. 67, no. 19, pp. 2825–6, 1995.

[162] R. F. Macpherson, G. M. Dunn, and N. J. Pilgrim, "Simulation of gallium nitride Gunn diodes at various doping levels and temperatures for frequencies up to 300 GHz by Monte Carlo simulation, and incorporating the effects of thermal heating," *Semiconductor Science and Technology*, vol. 23, no. 5, p. 055005 (7 pp.), 2008.

[163] R. P. Joshi, S. Viswanadha, P. Shah, and R. D. del Rosario, "Monte Carlo analysis of GaN-based Gunn oscillators for microwave power generation," *Journal of Applied Physics*, vol. 93, no. 8, pp. 4836–42, 2003.

[164] V. Gruzinskis, J. H. Zhao, P. Shiktorov, and E. Starikov, "Gunn effect and THz frequency power generation in n+-n-n+ GaN structures," in *Proceedings of the 10th International Symposium on Ultrafast Phenomena in Semiconductors (10-UFPS), 31 Aug.-2 Sept. 1998*, ser. Mater. Sci. Forum (Switzerland), vol. 297-298. Trans Tech Publications, 1999, pp. 341–4.

[165] V. N. Sokolov, K. W. Kim, V. A. Kochelap, and D. L. Woolard, "Terahertz generation in submicron GaN diodes within the limited space-charge accumulation regime," *Journal of Applied Physics*, vol. 98, no. 6, pp. 64 507–1, 2005.

[166] E. A. Barry, V. N. Sokolov, K. W. Kim, and R. J. Trew, "Large-signal analysis of terahertz generation in submicrometer GaN diodes," *IEEE Sensors Journal*, vol. 10, no. 3, pp. 765–71, 2010.

[167] F. Bernardini and V. Fiorentini, "Macroscopic polarization and band offsets at nitride heterojunctions," *Physical Review B (Condensed Matter)*, vol. 57, no. 16, pp. 9427–30, 1998.

[168] M. Buttiker and H. Thomas, "Current instability and domain propagation due to Bragg scattering," *Physical Review Letters*, vol. 38, no. 2, pp. 78–80, 1977.

VITA

Sriraaman Sridharan received the Bachelor of Engineering (B.E.) degree in Electrical and Electronics Engineering from Crescent Engineering College at University of Madras, Chennai, India in 1997 and the Master of Science (M.S.) degree in Electrical Engineering from The Ohio State University, Columbus, OH in 2001. He is currently working towards a Ph.D. in Electrical Engineering at the Georgia Institute of Technology, Atlanta, GA under the guidance of Dr. Douglas Yoder.

Previously, he was Member of Technical Staff (MTS) at Sun Microsystems Inc., Sunnyvale, CA, where he worked on top-level integration of the UltraSPARC V microprocessor.

He is also currently employed as Member of Technical Staff at GLOBALFOUNDRIES Inc., Sunnyvale, CA, where he is working on parasitic RC extraction, transistor performance benchmarking, and inductor design and modeling.